

MOLECULARLY IMPRINTED POLYMERS FOR CHEMICAL DETECTION ON A PAPER
SUBSTRATE

A Dissertation

by

TING-YEN CHI

Submitted to the Graduate and Professional School of
Texas A&M University
in partial fulfillment of the requirements for the degree of

DOCTOR OF PHILOSOPHY

Chair of Committee,	Jun Kameoka
Committee Members,	Terry S. Creasy
	Kamran Entesari
	Hong Liang
	Pao-Tai Lin
Head of Department,	Ibrahim Karaman

August 2021

Major Subject: Materials Science and Engineering

Copyright 2021 Ting-Yen Chi

ABSTRACT

Molecularly imprinted polymers (MIPs) have become one of the most promising materials for achieving superior performance in detecting numerous biological molecules, chemical compounds, and water pollutants. Integrated with a paper substrate, MIPs can be fabricated into a paper-based sensor that is low-cost, flexible, and easy to be processed and modified. In this study, we have demonstrated the detection of two typical perfluorinated compounds (PFCs), perfluorooctanoic acid (PFOA) and perfluorooctanesulfonic acid (PFOS), with the molecularly imprinted polyaniline (MIP-PANI) paper sensor platform. The detection limits of PFOA (20.55 ppt) and PFOS (7.12 ppt) with linear ranges of 1–200 ppt have been estimated. In addition, the surface of the MIP structure upon exposure to PFCs was characterized to propose the detection mechanism and visualize the molecular imprinting process.

We also demonstrated the integration of MIP-PANI with ultra-high frequency (UHF) wireless communication function for detecting multiple volatile organic compounds such as ammonia and ethanol. Wireless responses of the reduced reflection coefficient as a function of frequency are summarized, and the potential characteristic peaks and regions with trends in gas concentrations were identified. The calibration curves using a linear regression model were calculated to estimate the limit of detection of ammonia gas, which is 122 ppb.

To further expand the applications of the MIP-PANI platform, lentiviruses were imprinted in the polymer electrode. The calibration curve showed a considerably better signal response upon exposure to virus samples compared with the non-molecularly imprinted control, suggesting its potential in biomedical sensing.

This paper-based sensor incorporated with molecularly imprinted polymer electrodes adapts to various chemical as well as biological compounds with excellent sensitivity and selectivity at a low-cost compared with conventional assays, providing the potential in environmental monitoring and biomedical applications.

DEDICATION

This dissertation is dedicated to my beloved ones for actively encouraging and supporting me all the time.

ACKNOWLEDGEMENTS

First, I would like to appreciate my committee chair, Dr. Kameoka, for leading me to the fantastic world of sensing technology with steady patience, guidance, advise, and supports throughout my entire PhD career. His boundless enthusiasm for academic research inspires me to keep pursuing state-of-the-art studies. Also, I would like to thank my committee members, Dr. Creasy, Dr. Entesari, Dr. Liang, and Dr. Lin, for their providing invaluable comments and suggestions to my research work and this dissertation.

Meanwhile, I would like to thank my colleagues in Bio- and Soft MEMS Laboratory, Dimo, Zach, Chris, Sina, Jaskirat, and Sravani, for assisting my experiments and giving me suggestions and ideas, and staffs in Materials Characterization Facility as well as Microscopy Imaging Center for providing instrumental training and technical supports, and my friends and the departmental faculties and staffs for bringing me such a wonderful journey in Texas A&M University.

Finally, my greatest appreciation goes to my grandparents, parents, and family for their continuous supports and blessings and my dearest girlfriend for her endless encouragement and love. This dissertation could never be completed without them.

CONTRIBUTORS AND FUNDING SOURCES

Contributors

This work was supervised by the dissertation committee consisting of Professor Jun Kameoka [advisor] of the Department of Electrical and Computer Engineering and affiliated with the Department of Materials Science and Engineering, Professor Terry Creasy of the Department of Materials Science and Engineering, Professor Kamran Entesari and Professor Pao-Tai Lin of the Department of Electrical and Computer Engineering, and Professor Hong Liang of the Department of Mechanical Engineering.

Part of the X-ray photoelectron spectroscopy and scanning electron microscopy data in Chapter II was conducted by Mr. Zheyuan Chen of the Department of Electrical and Computer Engineering. The antenna design and printing in Chapter III were provided by Mr. Onder Dincel of the Department of Electrical and Computer Engineering. The lentivirus samples used in Chapter IV were synthesized and provided by Ms. Mo-Fan Huang and Dr. Dung-Fang Lee of the Department of Integrative Biology and Pharmacology in the University of Texas Health Science Center at Houston.

All other work for this dissertation was executed by the student independently.

Funding Sources

The graduate study was supported by MSEN Fellowship and Graduate Research Assistantship of the Department of Materials Science and Engineering and Graduate Research Assistantship of the project of Precise Advanced Technologies and Health Systems for Underserved Populations (PATHS-UP) under the National Science Foundation Engineering Research Center.

This work was also supported by the Bill and Melinda Gates Foundation under Grant Number OPP 1199456 and the National Science Foundation under Grant Number NSF 1648451. Its contents exclusively correspond with the author and do not contain any certain official perspectives of the Bill and Melinda Gates Foundation and the National Science Foundation.

NOMENCLATURE

MIP	Molecularly Imprinted Polymer
PANI	Polyaniline
MIP-PANI	Molecularly Imprinted Polyaniline
PFC	Perfluorinated Compound
PFOA	Perfluorooctanoic Acid
PFOS	Perfluorooctanesulfonic Acid
USEPA	United State Environmental Protection Agency
ppt	Part per Trillion
ppb	Part per Billion
ppm	Part per Million
PFOA-MIP-PANI	PFOA Molecularly Imprinted Polyaniline
PFOS-MIP-PANI	PFOS Molecularly Imprinted Polyaniline
DC	Direct Current
LoD	Limit of Detection
R ²	Coefficient of Determination
ATR-FTIR	Attenuated Total Reflection Fourier-transform Infrared Spectroscopy
XPS	X-ray Photoelectron Spectroscopy
SEM	Scanning Electron Microscopy
NIP-PANI	Non-molecularly Imprinted Polyaniline
VOC	Volatile Organic Compound
RFID	Radio-frequency Identification

UHF	Ultra-high Frequency
MHz	Mega (10^6) Hertz
VNA	Vector Network Analyzer
S_{11}	Reduced Reflection Coefficient
NH_3	Ammonia
EtOH	Ethanol
NH_3 -MIP-PANI	Ammonia Molecularly Imprinted Polyaniline
EtOH-MIP-PANI	Ethanol Molecularly Imprinted Polyaniline
Virus-MIP-PANI	Lentivirus Molecularly Imprinted Polyaniline

TABLE OF CONTENTS

	Page
ABSTRACT.....	ii
DEDICATION.....	iv
ACKNOWLEDGEMENTS.....	v
CONTRIBUTORS AND FUNDING SOURCES.....	vi
NOMENCLATURE.....	viii
TABLE OF CONTENTS.....	x
LIST OF FIGURES.....	xii
LIST OF TABLES.....	xvii
CHAPTER I INTRODUCTION.....	1
CHAPTER II PERFLUORINATED COMPOUND DETECTION USING A MOLECULARLY IMPRINTED POLYANILINE PAPER SENSOR.....	9
Introduction.....	9
Perfluorinated Compound Sensing.....	9
Paper-based Sensors.....	10
Materials and Methods.....	11
Materials.....	11
Synthesis of Molecularly Imprinted Polyaniline on Paper.....	12
Long-term Stability Test.....	14
Fabrication of Molecularly Imprinted Polymer Paper Sensor.....	14
PFOA/PFOS Exposure, Resistance Measurement, and Selectivity Experiment.....	15
PFOA/PFOS Detection in Mixed Solutions by PFOA/PFOS Hybrid Imprinted Polyaniline.....	17
Fourier-transform Infrared Spectroscopy.....	19
X-ray Photoelectron Spectroscopy.....	19
Scanning Electron Microscopy.....	20
Results.....	20
Long-term Stability Test.....	20
Fabrication of Molecularly Imprinted Polymer Paper Sensor.....	21
PFOA/PFOS Detection in Single Solutions.....	22
PFOA/PFOS Detection in Mixed Solutions and by Hybrid Imprinted Polyaniline.....	27

Attenuated Total Reflection Fourier-transform Infrared Spectroscopy Spectra	29
X-ray Photoelectron Spectroscopy Spectra	31
Surface Morphology of MIP Electrodes by Scanning Electron Microscopy.....	34
Selectivity among Relevant Perfluorinated Compounds	37
Discussion.....	39
CHAPTER III WIRELESS GAS DETECTION BASED ON MOLECULARLY IMPRINTED POLYANILINE.....	54
Introduction.....	54
Molecular Imprinting in Gas Sensing	54
Wireless Radio-frequency Identification Sensors.....	55
Materials and Methods.....	59
Materials	59
Synthesis of Ammonia and Ethanol Imprinted PANI.....	60
Gas Detection by Resistance Measurement	60
Fabrication of Antenna and Deposition of MIP-PANI.....	62
Gas Detection by Wireless Method	63
Results.....	66
Gas Sensing by DC Resistance Measurement	66
Wireless Gas Sensing.....	70
Discussion.....	75
CHAPTER IV FURTHER APPLICATIONS OF MOLECULARLY IMPRINTED POLYANILINE.....	80
Introduction.....	80
Virus Detection and Molecular Imprinting.....	80
Materials and Methods.....	82
Materials	82
Synthesis of Lentivirus-Imprinted PANI	83
Lentivirus Detection and Resistance Measurement	83
Results.....	84
Lentivirus Detection.....	84
Discussion.....	85
CHAPTER V CONCLUSIONS	88
REFERENCES	92
APPENDIX A THE OPERATING PROCEDURE OF SDR-KITS DG8SAQ VECTOR NETWORK ANALYZER (VNWA 3).....	108
APPENDIX B THE FULL-SPECTRUM DATA OF WIRELESS SENSING	112

LIST OF FIGURES

	Page
Figure 1 The schematic diagram of the fabrication and the operating principle of MIP sensors. . .	2
Figure 2 The schematic overview of the sample intermolecular interactions in MIPs: (a) reversible covalent recognition (b) non-covalent recognition activated by cleaved covalently imprinted functional templates (c) electrostatic attraction (d) Van der Waals force or hydrophobic interaction (d) metallic ligation or coordination. Reprinted from [4].	4
Figure 3 Applicable receptors and biomarkers for being imprinted in a polymer matrix and the size-dependent distribution of different types of imprinted polymers. Reprinted from [29].	7
Figure 4 The schematic diagram of the synthesis of PFOA-MIP-PANI and PFOS-MIP-PANI and the molecular imprinting process. (a) PFOA or PFOS, as the template, was first mixed with aniline monomers in HCl aqueous solution, followed by immersing paper strips for the thorough absorption of the monomers on the surface. The polymerization was initiated by adding the oxidant, and the PFC-imprinted PANI was synthesized. (b) The PFOA or PFOS templates were removed by sonication for 4 h in a mixed solution of methanol and acetic acid at a v/v ratio of 6:1, leaving cavities of specific recognition sites. (c) PFC samples were then dispensed to the surface of the integrated paper sensor, and the PFOA-MIP-PANI or PFOS-MIP-PANI was then able to detect the target PFCs by the molecularly imprinted structures. The targets and the host of MIP-PANI performed an equilibrium system of association and dissociation. (d) The photographic images of the integrated sensor with a flexible paper/plastic substrate. Scale bar denotes 1 cm in length.	13
Figure 5 The experimental setup for measuring the resistance of the MIP-PANI electrodes. The scale bar denotes the length of 1 cm, which also corresponds to the dimension of the grids on the cutting mat. The probes are connected to the multimeter with a portion of the wires not shown in this picture.	17
Figure 6 Long-term stability of PANI on paper (n=4). The <i>x</i> axis represents the time from the fabrication of PANI on paper strips.	21
Figure 7 The resistivity ratios of the NIP-PANI and MIP-PANI sensors exposed to PFOA or PFOS. NIP-PANI: non-molecularly imprinted PANI; PFOA-MIP-PFOA: PFOA-imprinted PANI; PFOS-MIP-PANI: PFOS-imprinted PANI. The two types of MIP-PANI exposed to its designated analytes are denoted as PFOA detection and PFOS detection.	23
Figure 8 The resistivity ratios of NIP-PANI and PFOA-MIP-PANI paper sensors after dispensing PFOA aqueous samples on the sensors with different concentrations.	

Each point denotes the average value measured from three devices, and the error bars represent the standard deviations. The red line is the calibration curve with the coefficient of determination (R^2) estimated by using a linear regression model. 25

Figure 9 The calibration curve of NIP-PANI and PFOS-MIP-PANI exposed to various concentrations of PFOS aqueous solutions. The resistivity ratios were normalized to the resistivity ratio of DI water. The data points denote the averages of repeating measurements of DC resistance of at least three devices, from which the standard deviations are also calculated and marked as error bars. The red line is the calibration curve with the coefficient of determination (R^2) estimated by using a linear regression model. 26

Figure 10 The 3D diagram of resistivity ratios of NIP-PANI, PFOA-MIP-PANI, PFOS-MIP-PANI, and the hybrid imprinted PANI (PFOA/PFOS-MIP-PANI) exposed to PFOA/PFOS mixed solutions at the combined concentration of 70 ppt. (a) The 3D figure is a perspective view plotted by Origin software, showing the error bars calculated from at least three devices. The dots represent the mean averages that came from at least three devices as well. (b, c) The complementary 3D figures plotted by SigmaPlot, which demonstrate two different viewing angles to reveal the concealed bars from the one side of view. All three figures are plotted based on the same set of data. 28

Figure 11 The ATR-FTIR spectra of the surface of PFOA-MIP-PANI and NIP-PANI. NIP-PANI denotes the polyaniline synthesized in the absence of PFOA templates while the template removal process including sonication was still performed. The y axis based on the transmission mode has been adjusted in order to compare the wavelengths of the characteristic peaks. The arrows point out the characteristic peaks with their corresponding wavenumbers. The blue dotted lines are provided for comparing the potential redshifts. 30

Figure 12 The ATR-FTIR spectra of the surface of PFOS-MIP-PANI and NIP-PANI. NIP-PANI denotes the polyaniline synthesized in the absence of PFOS templates while the template removal process including sonication was still performed. The y axis based on the transmission mode has been adjusted in order to compare the wavelengths of the characteristic peaks. The arrows point out the characteristic peaks with their corresponding wavenumbers. The blue dotted line is designated for comparing the potential redshift. 31

Figure 13 XPS spectra of the surface of MIP-PANI electrodes in each processing step of molecular imprinting and PFOA/PFOS exposure. Non-molecularly imprinted PANI (NIP-PANI) served as control. (a, b) F1s spectra (c, d) N1s spectra. The arrows represent the direction of redshift in binding energy. The y axis based on counts per second has been adjusted to the arbitrary unit in order to compare the binding energies of different samples. 33

Figure 14 SEM images of the surface morphology of (a) NIP-PANI before sonication; (b) NIP-PANI after sonication and before the exposure to PFOA; (c) NIP-PANI after the exposure to PFOA; (d) PFOA-MIP-PANI before sonication; (e) PFOA-MIP-PANI after sonication and before the exposure to PFOS; (f) PFOA-MIP-PANI after the exposure to PFOS. The scale bar denotes 1 μm in length.....	35
Figure 15 SEM images of the surface morphology of (a) NIP-PANI before sonication; (b) NIP-PANI after sonication and before the exposure to PFOS; (c) NIP-PANI after the exposure to PFOS; (d) PFOS-MIP-PANI before sonication; (e) PFOS-MIP-PANI after sonication and before the exposure to PFOS; (f) PFOS-MIP-PANI after the exposure to PFOS. The scale bar denotes 1 μm in length.....	36
Figure 16 The selectivity of PFOA-MIP-PANI to PFOA, PFBA, PFHxA, and PFOS. The concentration of each PFC in the aqueous sample was 70 ppt. The bars denote the average values of DC resistivity ratios normalized to which of water. The standard deviations as error bars were calculated from three devices. The asterisks represent the statistical significance ($p < 0.05$) compared with the ratio of PFOA.....	38
Figure 17 The selectivity of PFOS-MIP-PANI to PFOS, PFBA, PFHxA, and PFOA. The concentration for each chemical in the aqueous samples was 70 ppt. The data were normalized to water resistivity. Each bar denotes the average of DC resistivity ratios measured from three devices, and the standard deviations are also marked as the error bars. The asterisks represent significance ($p < 0.05$) lower than the response of PFOS.	39
Figure 18 The transformation between the forms of polyaniline emeraldine salt and emeraldine base. The symbol of A- denotes the counter ion of the positively charged electron-hole.....	51
Figure 19 The scheme of the concept of wireless chemical sensors (WCS). Reprinted from [102].	56
Figure 20 The schematic illustration of the definition of the S-parameter.	59
Figure 21 (a) The photographic image of the experimental setting of DC resistance measurement for gas sensing. The pop-out figure presents the sensor integrated with two electric wires for connecting the probes with the sensor in the sealed test chamber. (b) The scheme of the gas test chamber with its dimensional information for calculating the total volume.....	62
Figure 22 The instrumental setup of the wireless sensing experiment. The inserted picture displays the inkjet-printed antenna on a flexible substrate of a polyester film. Note that the excess wires connecting the reader and the vector network analyzer (VNA) were hindered in this figure.....	63

Figure 23 The screenshot of the VNA software including the frequency range and the y axis of the S_{11} parameter with the unit of decibels.	65
Figure 24 The real-time DC resistances of (a) NIP-PANI and NH_3 -MIP-PANI electrodes after exposure to 100 ppm NH_3 gas (b) NIP-PANI and EtOH-MIP-PANI electrodes after exposure to saturated ethanol vapor (concentration $\sim 58,684$ ppm).	67
Figure 25 The real-time resistance responses and the corresponding linear regression curves as a function of VOC gas concentration. (a, c) NH_3 detection using the NH_3 -MIP-PANI electrode. After exposure to NH_3 gas for 35 min, the test chamber was opened for 25 min for recovery, followed by injecting the higher concentration of NH_3 . (b, d) Ethanol detection by using the EtOH-MIP-PANI electrode. The exposure and recovery time was 10 min. The data points in the calibration curves were obtained from the peak values in the real-time responses.....	69
Figure 26 (a) The wireless response of ΔS_{11} of the printed antenna with NH_3 -MIP-PANI upon exposure to NH_3 gas. The red arrow points out the peak at 982 MHz (b) The calibration curve calculated from the ΔS_{11} values at 982 MHz by using a linear regression model.	70
Figure 27 (a) The ΔS_{11} -frequency data of ethanol gas detection. The red arrow indicates the peak being analyzed by linear regression. (b) The calibration curve of ΔS_{11} as a function of ethanol concentration at 949 MHz.....	71
Figure 28 The ΔS_{11} -frequency data of NH_3 gas detection at the range of (a) 890 to 920 MHz (b) 970 to 990 MHz. The two figures share the same figure caption as shown in part (a). Arrows indicate the region and peak of interest with a correlation of ΔS_{11} with the concentration of NH_3 gas.	72
Figure 29 The calibration curves at 974 MHz calculated from the wireless data as shown in Figure 28b. (a) The full set of the data points from 0 to 100 ppm of NH_3 gas. (b) the calibration curve plotted by the partial wireless data from 0 to 10 ppm (10,000 ppb) as the blue shade in part a. The red line denotes the linear regression line from 0 to 2.5 ppm.....	73
Figure 30 The ΔS_{11} -frequency diagrams of NH_3 gas detection. (a) The diagram from 870 to 1,000 MHz with a red arrow suggesting the characteristic peak being analyzed. (b, c) The enlarged figures of different magnification from part a. The peak locates at around 882.7 MHz. All the figures use the same notation of NH_3 concentrations with different colors of the profiles.....	74
Figure 31 (a) The calibration curve calculated from Figure 30c. (b) The calibration curve plotted by selecting the partial data from 0 to 10 ppm. (c) The partial calibration curve selected by the range of 0 to 1,000 ppb (1 ppm). The standard errors were collected from at least three repeating sweeps provided by the VNA.	75

Figure 32 The schematic example of virus-imprinted polymers. As the typical molecular imprinting process, the virus was co-polymerized and removed from the matrix, leaving cavities for recognizing the H5N1 virus as shown in the scheme. The probe mentioned here in this study was to inhibit the binding with the MIP matrix. Reprinted from [26]..... 80

Figure 33 (a) The resistivity ratios and the calibration curves of NIP-PANI and Virus-MIP-PANI electrodes after different time of drying. The red line is the linear regression line calculated from the data between 1.1×10^5 to 2.2×10^5 TU/ml. (b) The enlarged figure focusing on the control groups of NIP-PANI in part a. 85

Figure 34 The S_{11} -frequency diagram of signals from four different experimental setups for quality control of the instrumental calibration as well as the signal sources. 111

Figure 35 The full-spectrum ΔS_{11} -frequency diagram associated with Figure 26..... 112

Figure 36 The full-spectrum ΔS_{11} -frequency diagram associated with Figure 27..... 113

Figure 37 The full-spectrum ΔS_{11} -frequency diagram associated with Figure 28..... 114

Figure 38 The full-spectrum ΔS_{11} -frequency diagram associated with Figure 30..... 115

LIST OF TABLES

	Page
Table 1 The denotation of the mixture of PFOA and PFOS sample solutions.	18
Table 2 The summary of the linear regression ranges, regression equations, coefficients of determination (R^2), and limits of determination (LoD) of each sensing element.	24
Table 3 The reference of the characteristic peaks in the FTIR spectra of PANI, PFOA, and PFOS. Adapted from [56-62].	42
Table 4 The binding energies of the 1s orbital of fluorine (F) in the FTIR spectra of various chemicals. Adapted from [66-76].	45
Table 5 The binding energies of the 1s orbital of organic nitrogen (N) in the FTIR spectra of various chemicals. Adapted from [66, 67, 69, 80-86].	47
Table 6 The features of common wireless communication protocols for chemical sensing. Adapted from [102-112]. LF: low frequency; HF: high frequency; UHF: ultra-high frequency	57
Table 7 The summary of parameters for evaluating the response of the molecularly imprinted gas sensors for NH_3 and ethanol detection. n/a: data not available.	68

CHAPTER I

INTRODUCTION

Intermolecular interactions such as ionic bonding, hydrogen bonding, van der Waals forces, and hydrophobic effects dominate the natural molecular recognition. For receptors to identify their corresponding targets, a complementary structure must be generated by applicable intermolecular forces or stereochemical affinity between the target and host matrix. Enzymes are typical examples having extraordinarily sophisticated structures based on chemical ligands and stereo compatibility to their target proteins. Although natural receptors and antibodies are entitled to precisely recognize corresponding antigens, they are vulnerable to critical chemical or physical environments. Therefore, synthetic antibodies have been of interest in sensing applications. Synthetic polymers become the strong candidate for making artificial receptors because of their low-cost, durability, and processibility of various structures. To reproduce the receptor-like structures of natural antibodies and their capability of recognizing specific analytes on synthetic polymers, molecular imprinting has been one of the most inspiring approaches for developing state-of-the-art chemical or biosensors.

The concept of molecular imprinting as a promising approach to fabricate synthetic antibodies was firstly introduced by Linus Pauling in 1940 [1]. In the general principle of molecular imprinting, monomers are polymerized in the presence of target analytes to fabricate artificial antibodies. The target analytes acting as templates interact with monomers by certain intermolecular interactions and create an intermediate complex, followed by being polymerized into a template-embedded polymer matrix. The templates are then either chemically or physically removed from the polymer matrix by an appropriate approach, leaving cavities with

structures complementary to the templates. In other words, the polymer matrix is imprinted by the templates in the polymerization step, and the resulted polymer is called a molecularly imprinted polymer (MIP) carrying numerous binding cavities that are counterparts specific to the templates. MIPs are hence capable of recognizing their designated target molecules, and such the procedure is analogous to how natural enzymatic receptors work. The schematic diagram of MIPs is shown in Figure 1 illustrating the co-polymerization of monomers and templates in the reaction batch and the recognition of the analytes in the sensing stage. The recognition and desorption of analytes in MIPs react as equilibrium, resulting in a signal variation that can be analyzed to signal outputs such as colorimetric changes and calibration curves of analyte concentrations. Moreover, the association and dissociation of templates on the matrix are usually reversible and equilibrium, making the removal of templates from MIPs be the most critical step among molecular imprinting processes. Characterization of the residual templates can be performed to justify the effectiveness of template removal.

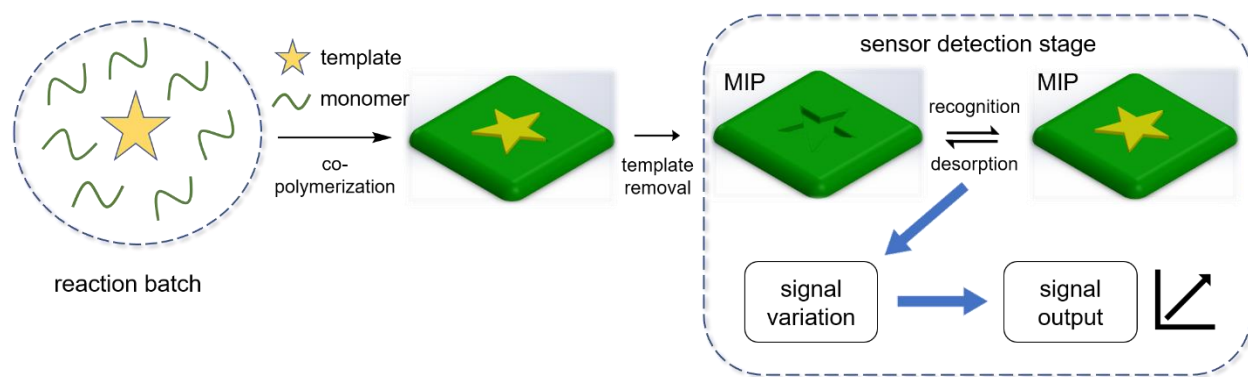


Figure 1 The schematic diagram of the fabrication and the operating principle of MIP sensors.

Several reviews have comprehensively discussed MIPs including principles as well as applications [2, 3]. The types of interactions between templates and monomers can be covalent bonding, non-covalent bonding, metallic ligands, Van der Waals force, electrostatic attraction, or any hybrids of them, depending on the acting functional groups on templates as well as monomers [4]. The schematic diagram of these sample intermolecular interactions between the template and matrix in MIPs is shown in Figure 2. Because of the excellent bonding strength of covalent bonds, the bonding efficiency and homogeneity in the imprinting step should be better than those with non-covalent binding [5]. However, cleaving agents are needed for removing covalently imprinted templates from the matrix [6]. On the contrary, non-covalent imprinting provides a more flexible way of selecting templates as well as the polymer matrix depending on the reactivity and processibility. Templates with non-covalent bindings to a polymer matrix can be removed by physical methods like sonication and centrifugation. In fact, most of the intermolecular interactions of biomolecules in nature rely on non-covalent bindings. Besides, hybrid systems that incorporate covalent and non-covalent bindings have been reported [7]. For instance, a peptide consisting of three amino acids (Lys-Trp-Asp) is firstly imprinted via covalent bonds to the polymer matrix, followed by hydrolysis to cleave covalent bonding and to remove the peptide templates. The tripeptide recombined the polymer matrix by hydrogen bonding, which is non-covalent.

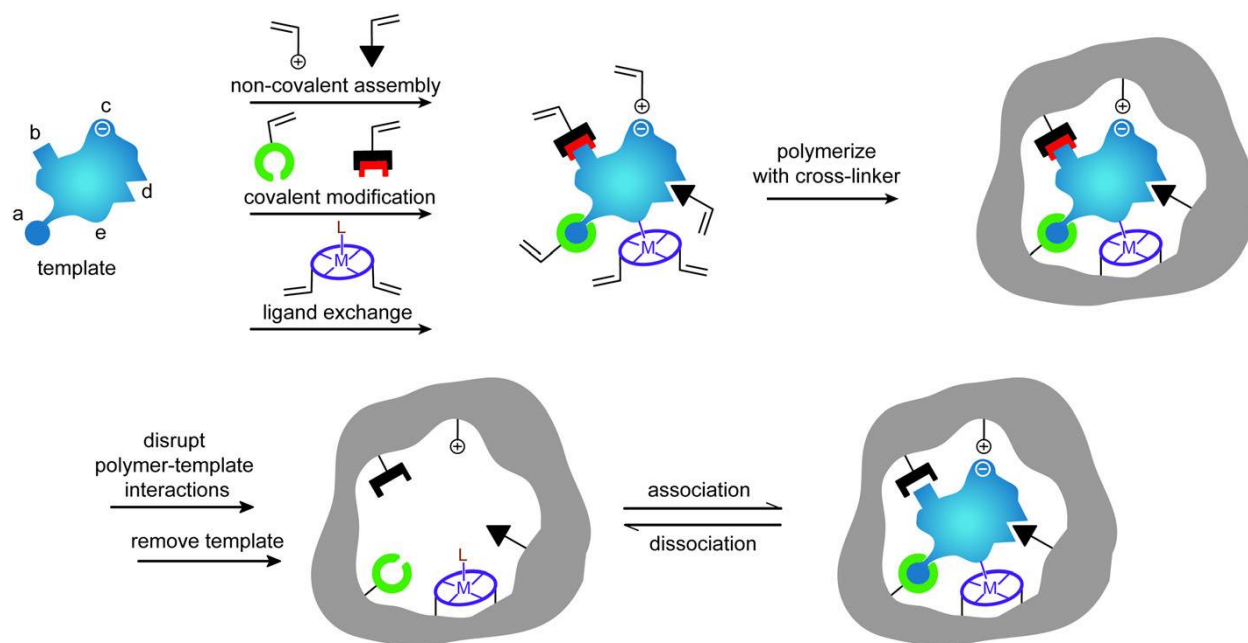


Figure 2 The schematic overview of the sample intermolecular interactions in MIPs: (a) reversible covalent recognition (b) non-covalent recognition activated by cleaved covalently imprinted functional templates (c) electrostatic attraction (d) Van der Waals force or hydrophobic interaction (e) metallic ligation or coordination. Reprinted from [4].

MIPs have been the favorable candidate for fabricating electrochemical sensors, of which conductive polymers are desired because the charge carriers conducting through the bonding sites and matrix lead the signal variation upon the recognition of target molecules. Polymers such as polyethylene or polypropylene are naturally insulated and not suitable for fabricating MIP electrodes, in which the electrical signal transduction is prohibited. As a result, many electrochemical sensors have applied molecularly imprinted conductive polymers as their sensing elements to improve the detecting effectiveness. To fabricate the electrodes, MIPs are generally integrated with various substrates such as gold electrodes [8], glassy carbon electrodes [9], nanoparticles [10, 11], and paper [12-14]. Several methods for preparing MIP electrodes include drop-casting of polymer solution on substrates, bulk polymerization in the presence of

templates and substrates, mixing conductive dopants like graphene or carbon nanotubes into MIPs on a supporter such as plastic beads, and electrochemical polymerization on the working electrode. Particularly, electrochemical polymerization enables the thickness and uniformity of MIP films on electrodes to be handily controllable using cyclic voltammetry in a bulk solution of monomers and template analytes.

Conductive polymers integrated by molecular imprinting deliver a novel type of electrode for electrochemical sensors with high sensitivity and selectivity to chemical and biological compounds. Polyaniline (PANI), one of the typical conductive polymers, gives a promising potential of being introduced by a molecular imprinting process because of economic and simple synthesis/doping procedures. Also, the excellent environmental durability and capability of operating in an aqueous phase make PANI one of the best candidates of molecularly imprinted conductive polymers [15]. Abundant research of molecularly imprinted PANI (MIP-PANI) sensors has been reported. For example, Luo et al. deposited MIP-PANI on a gold electrode to detect ovalbumin, a major egg allergen. This MIP-PANI sensor, using the peak current in cyclic voltammetry as the responsive signal, recognized ovalbumin much better than non-molecularly imprinted PANI did [16]. In addition, PANI imprinted by paracetamol, usually known as Panadol for pain relief, had dramatically improved the detection performance from the responses of peak current in cyclic voltammetry. Interestingly, the aniline monomers were synthesized on a polymeric micelle of poly(2-acrylamido-2-methyl-1-propane sulfonic acid-*co*-styrene) acting as a nanoreactor [11]. Moreover, for recognizing one of the most famous explosives, 2,4,6-trinitrobenzene (TNT), PANI modified with graphene was imprinted by picric acid, of which the chemical structure is nearly identical to TNT. MIP-PANI showed a significant difference in differential pulse voltammograms compared with control. [17]. Apart from PANI, other

conductive polymers such as polypyrrole [18, 19], polythiophene [20], and poly(3,4-ethylene dioxythiophene (PEDOT) [21] are reported for serving as the matrix materials for molecular imprinting electrodes.

Since the molecular imprinting process is considered one of the biomimetic systems that simulate the protein-receptor function in biomolecules, biomolecule-imprinted polymers become the state-of-art sensing materials for biomedical detection and diagnostic of precursors of diseases. As discussed above, the stability and accessibility of synthetic polymers make them suitable for serving as artificial proteins or antibodies with a superior lifetime. Various biomolecular templates such as polypeptides [22], proteins [23], or even bacteria [24] or viruses [25-28] are being imprinted in polymers via different types of functional groups in recent research. Based on the size dependence, among typical MIPs we have discussed, those with larger templates like microorganisms and cells can be further categorized by virus-imprinted polymers (VIPs) and cell-imprinted polymers (CIPs) as shown in Figure 3 [29].

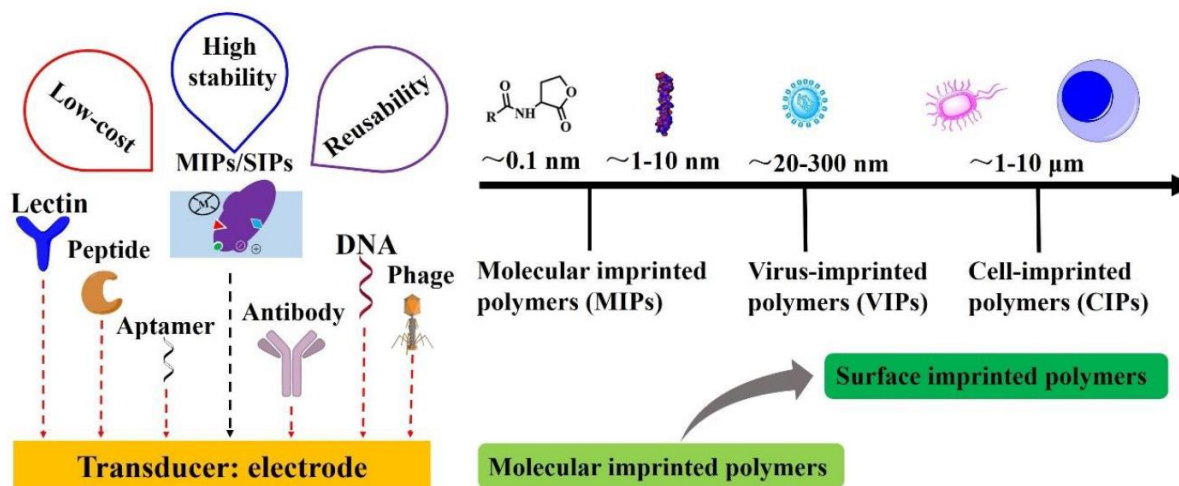


Figure 3 Applicable receptors and biomarkers for being imprinted in a polymer matrix and the size-dependent distribution of different types of imprinted polymers. Reprinted from [29].

Unlike small compounds with low molecular weights, proteins are much larger in both geometric and molecular weight points of view, causing many challenges in molecular imprinting. First, a highly crosslinked polymer matrix can obstruct the dispersion of templates as well as the removal, making the imprinted cavities inhomogeneous in the matrix. Secondly, because proteins are sensitive to multiple physical and chemical conditions that change the morphology and structures, the conformation memorized in the imprinted cavities may be different from those that should have been specifically recognized. Also, multiple complex binding sites on a protein may cause partial and non-specific binding to the polymer matrix. In other words, the specific rebinding is not efficient anymore. Additionally, proteins themselves have large sizes, and the diffusion in the polymer matrix is therefore restricted. As the disadvantage of a dense matrix, protein templates are not only difficult to spread out the entire matrix, but also hard to be removed and to create cavities for recognition. Such a problem may

be solved by nanoscale and surface imprinting, of which only the surface templates are imprinted and then removed. Moreover, proteins are vulnerable to many organic solvents in which MIPs are often synthesized. Water-based synthesis is desired which limits the selection of monomers. Hydrogen bonding interaction between proteins and polymer matrix is severely interfered with by aqueous solutions as well [30]. Despite the challenges above, the number of protein-imprinted polymer systems is still increasing. Polyaniline, as discussed above, has been served as the model polymer matrix for proteins such as ovalbumin [16] and horseradish peroxidase [31]. For more complicated cases, viral [25, 32, 33] and bacterial [24, 34] sensing based on MIPs is also feasible.

In summary, molecular imprinting technology provides a promising method to fabricate synthetic antibodies that mimic natural receptors with the capability of recognizing the specific target molecule. Such the feature make MIPs have the attractive potential in sensing application. Advantages of MIPs include: (1) excellent detection efficacy benefited from the complementarity and specificity of the polymer matrix and targets. (2) simple fabrication processes and the flexibility of being applied to various types of analytes and polymers (3) better stability compared with enzymatic assays which are sensitive and vulnerable to environments (4) the low-cost and potential in high throughput production of sensing elements. In this dissertation, a low-cost, accurate, and sensitive sensor platform based on MIPs were developed. Different types of analytes such as perfluorinated compounds, gases, and viruses of sensing approaches like resistometric and wireless sensing were also investigated.

CHAPTER II

PERFLUORINATED COMPOUND DETECTION USING A MOLECULARLY IMPRINTED POLYANILINE PAPER SENSOR*

Introduction

Perfluorinated Compound Sensing

Perfluorinated compounds (PFCs) are a series of aliphatic chemicals that all or part of the hydrogen atoms on the alkyl groups are substituted by fluorine atoms. PFCs have been used in industries for manufacturing water and oil foiling products, fire-retardant materials, and packaging since the 1950s [35, 36]. After decades of utilization, PFCs are found to be persistent and cumulative in environments due to the extremely strong and stable carbon-fluorine bonding. For example, the reported average concentration of perfluorooctanoic acid (PFOA) and perfluorooctanesulfonic acid (PFOS) in the basin of the Tsurumi River, Japan, was 15.9 ng/L and 179.9 ng/L, respectively [37]. As a result, PFCs are responsible for the toxicity to metabolism [38], reproduction [39], and liver function [40]. Governmental regulations for maximum tolerance of PFCs are therefore being conducted and updated. The United States Environmental Protection Agency (USEPA) released the advisory maximum concentration of 70 ng/L (70 part-per-trillion, 70 ppt) for a combination of PFOA and PFOS in drinking water [41]. In addition, according to the guidance broadcasted by Interstate Technology and Regulatory Council,

* Part of the data reported in this chapter is reprinted with permission from “Perfluorooctanesulfonic Acid Detection Using Molecularly Imprinted Polyaniline on a Paper Substrate” by Ting-Yen Chi, Zheyuan Chen, and Jun Kameoka, 2020, *Sensors*, 20, 7301, Copyright 2020 by MDPI.

approximately six million people in the United States are consuming drinking water in which the combined concentration of PFOA and PFOS exceeds the health advisory of 70 ppt from USEPA [42]. Therefore, for the severe public health issues in the world, the detection of PFCs in water is of interest as well as importance.

Currently, the detection of PFCs mostly relies on high-performance liquid chromatography/mass spectroscopy (HPLC/MS) and gas chromatography/mass spectroscopy (GC/MS) which are extremely expensive and time-consuming. As a result, developing a low-cost assay with the capability of detecting the notorious chemicals with a concentration near the official suggestion or the regulation is highly demanded. Recently, several sensors have been developed for detecting PFCs. For example, as reported by Chen et al., PFOS can be detected by utilizing fluoro-photometry on red-emission carbon dots with a linear range from 100 $\mu\text{g/L}$ to 6 mg/L [43]. Another method based on a complex of blue-fluorescent carbon dots and berberine chloride hydrate for the detection of PFOS is reported with the linear region from 110 $\mu\text{g/L}$ to 25 mg/L [44]. A smartphone app-based sensor is also developed using colorimetric analysis to an active agent of methylene blue. The detection range is claimed in the 10 to 1000 ppb [45]. Consequently, an accurate, reliable, and fast assay for detecting PFCs is still in thriving development.

Paper-based Sensors

Paper substrates possess numerous advantages among other conventional substrates like metal electrodes. Paper is flexible, portable, extremely cheap, lightweight, biodegradable, and easy to be processed [46]. To be specific, the low-cost and ease of availability enable paper-based sensors to compete with conventional detecting methods that are expensive and with high-

threshold. For example, a single test of HPLC/MS assay could cost more than hundreds of dollars; however, paper-based electronics could cost less than ten dollars per device. Especially, for those developed countries and areas, the demand for a simple and sensitive device at an affordable price is of interest. Moreover, paper-based devices can be easily fabricated by printing or casting conductive materials on paper fibers. Conductive inks and printers are commercially available for printing electrodes with a variety of shapes as needed, offering engineers exceptional flexibility in designing paper-based electrodes; in the meantime, the conductivity will be unsacrificed.

Jointly with these advantages, various paper-based sensors are reported to evaluate the potential for replacing conventional substrates such as printed circuit boards or glass slides. For instance, paper can serve as the substrate for electrochemical sensors integrated with microfluidic channels and sensing elements (the working electrode) in a multi-layer configuration [47-49]. Furthermore, the multi-layers can be folded together to inspire an “origami”, which means paper folding in Japanese, microfluidic design attributed to the flexibility of paper [46, 50-52]. Other applications include energy storage [53] and supercapacitors [54].

Materials and Methods

Materials

Aniline, ammonium persulfate (APS), PFOA, PFOS, perfluorobutanoic acid (PFBA), and perfluorohexanoic acid (PFHxA) were purchased from Sigma-Aldrich (St. Louis, MO, USA). Hydrochloric acid (HCl, 36–38%) and acetic acid were purchased from Macron (Center Valley, PA, USA). Methanol was obtained from VWR Chemicals (Radnor, PA, USA). Paper made of

polyester fibers was obtained from Xerox (Cat# 3R12493, Norwalk, CT, USA). The filter paper of Whatman 1 was purchased from VWR Chemicals (Radnor, PA, USA). Silver conductive ink was purchased from Creative Materials (Cat# 125-15, Ayer, MA, USA).

Synthesis of Molecularly Imprinted Polyaniline on Paper

PFOA or PFOS was used as the template for the molecular imprinting process on the PANI to synthesize PFOA molecularly imprinted PANI (PFOA-MIP-PANI) and PFOS molecularly imprinted PANI (PFOS-MIP-PANI). The monomer solution was prepared by mixing 0.2 g of aniline and 1 ml of 100 ppm PFOA or PFOS aqueous solution in 1 M HCl with a concluding volume of 5 ml. Paper strips with the dimensions of 1 cm × 0.5 cm were immersed in the monomer solution and soaked for 5 min to be saturated with the solution. The polyester paper we used can absorb the most PANI on its surface during polymerization, giving the best conductivity compared with other filter papers such as the Whatman series. Afterward, the oxidant solution prepared by mixing 409 mg of APS in 5 ml of 1 M HCl was added drop-by-drop into the monomer solution under vigorous stirring to initiate the polymerization of PANI on paper substrates. The HCl was to act as the dopant enriching the conductivity of the PANI and to sustain the pH (pH = 0) in the reaction. The concentration of PFOA or PFOS templates in the reaction solution was 10 ppm. After 10 min of polymerization, the paper strips were removed and flushed with deionized water (DI water) multiple times until the eluent was clear and no excess PANI as dark-colored particles were found in the solution.

To remove the template from the PANI matrix, the paper strips were immersed in a mixture of methanol and acetic acid at a ratio of 6:1 (v/v), followed by sonication for 4 h. The solution was refreshed every hour to ensure the effectiveness of template extraction. The

resulting strips were removed and rinsed with DI water until the pH reached 7, and then air-dried at 25°C for at least 12 h before fabrication. Non-molecularly imprinted PANI (NIP-PANI), serving as the control, was synthesized by following the same protocol given formerly without the addition of PFOA or PFOS in the monomer solution. The schematic diagram of the synthesis of PFOA-MIP-PANI and PFOS-MIP-PANI and the principle of molecular imprinting technology is shown in Figure 4.

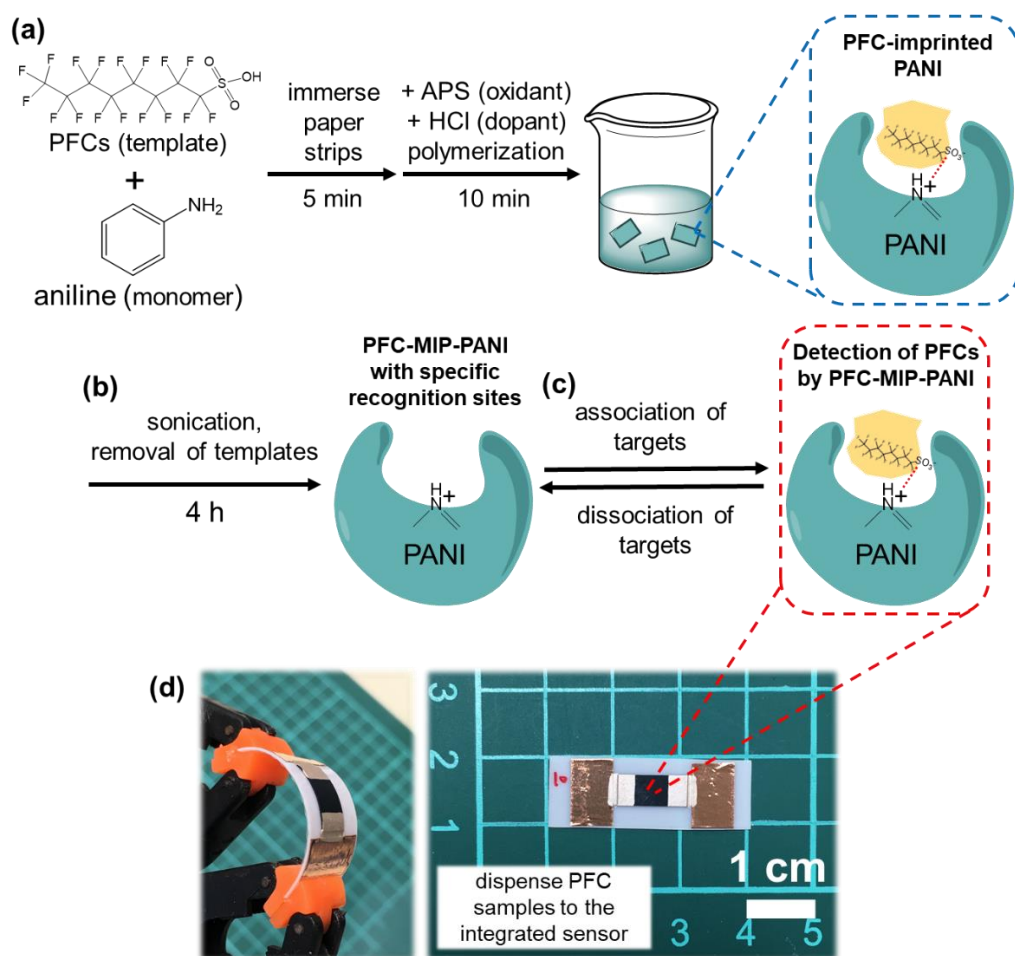


Figure 4 The schematic diagram of the synthesis of PFOA-MIP-PANI and PFOS-MIP-PANI and the molecular imprinting process. (a) PFOA or PFOS, as the template, was first

mixed with aniline monomers in HCl aqueous solution, followed by immersing paper strips for the thorough absorption of the monomers on the surface. The polymerization was initiated by adding the oxidant, and the PFC-imprinted PANI was synthesized. (b) The PFOA or PFOS templates were removed by sonication for 4 h in a mixed solution of methanol and acetic acid at a v/v ratio of 6:1, leaving cavities of specific recognition sites. (c) PFC samples were then dispensed to the surface of the integrated paper sensor, and the PFOA-MIP-PANI or PFOS-MIP-PANI was then able to detect the target PFCs by the molecularly imprinted structures. The targets and the host of MIP-PANI performed an equilibrium system of association and dissociation. (d) The photographic images of the integrated sensor with a flexible paper/plastic substrate. Scale bar denotes 1 cm in length.

Long-term Stability Test

To determine the model substrate for PANI to be deposited on, two types of commercially available paper, polyester paper from Xerox and Whatman 40, were selected for the long-term stability test. Paper was cut into strips (1 cm × 1 cm) and deposited with PANI on the surface. The resistivity of each strip in the air at 25°C was measured by a multimeter (8846A, Fluke) once a week.

Fabrication of Molecularly Imprinted Polymer Paper Sensor

For fabricating the device, an MIP-PANI pad was first attached to a piece of the plastic stencil (Cat# 381384, Show-offs Company, USA) with the dimensions of 1 cm × 3 cm using double-sided tape. Two pieces of copper tape (1 cm × 1/4 in), as the connecting electrodes, were then attached on both sides of the MIP-PANI pad, leaving a 1 mm gap between the MIP-PANI pad and each copper electrode. The gaps were filled with silver ink to build the conjunction between the MIP-PANI pad and the connecting electrodes. The silver ink was then air-dried at 25°C for at least 12 h, and the assembled device was ready to detect PFOA and PFOS. The photographic image of the integrated sensor is presented in Figure 4.

PFOA/PFOS Exposure, Resistance Measurement, and Selectivity Experiment

PFC solutions with multiple concentrations from 0 to 100 ppt were prepared to cover the maximum tolerance of 70 ppt from the USEPA's guideline. For the exposure step, a 30 μL aliquot of PFOA or PFOS was dispensed on the center of the PANI pad and reacted for 30 min, and then air-dried at 25°C. The reaction time of 30 min after dispensing PFC samples was used to ensure that the detection achieved an equilibrium. The change in resistance between the two electrodes after exposure to PFOS was measured by the direct current (DC) resistance mode of a multimeter (8846A, Fluke, Everett, WA, USA). The experimental setup is illustrated in Figure 5. Resistance (R) can be converted to resistivity (ρ) by using the following equation,

$$\rho = \frac{RA}{L}$$

Equation 1

where L is the length and A is the cross-sectional area of the PANI paper electrode. Since the dimension of paper electrodes remains the same for all specimens, the measured resistance is proportional to the resistivity of the PANI paper electrodes. All the responses were normalized based on the DI water (0 ppt) by using the following equation, where ρ_{before} and ρ_{after} are the resistivity of the PANI paper electrodes before and after the exposure, respectively:

$$\text{Normalized ratio} = \frac{\text{ratio}_{\text{sample}}}{\text{ratio}_{\text{water}}} = \frac{(\rho_{\text{after, sample}})/(\rho_{\text{before, sample}})}{(\rho_{\text{after, water}})/(\rho_{\text{before, water}})}$$

Equation 2

The statistical analysis and the calibration curves were generated by using the default linear regression model in SigmaPlot. The statistical significance between experimental groups

was defined as p (p -value) < 0.05 and determined by a Student's t -test performed by SigmaPlot.

The typical equation to calculate the limit of detection (LoD) is [55]:

$$\text{LoD} = \frac{3\sigma}{m}$$

Equation 3

where m and σ are the slope and the standard deviation of blank samples from the calibration curve, respectively. By plugging in these values, the limit of detection of PFOA or PFOS for the PFOA-MIP-PANI and PFOS-MIP-PANI paper sensors can be estimated.

Relevant PFCs of PFBA, PFHxA were used for the selectivity experiment of which the concentration for comparison was set to be 70 ppt corresponding to the maximum tolerance advised by USEPA. The experimental procedures followed the same protocol for measuring the resistivity of MIP-PANI electrodes as previously mentioned.

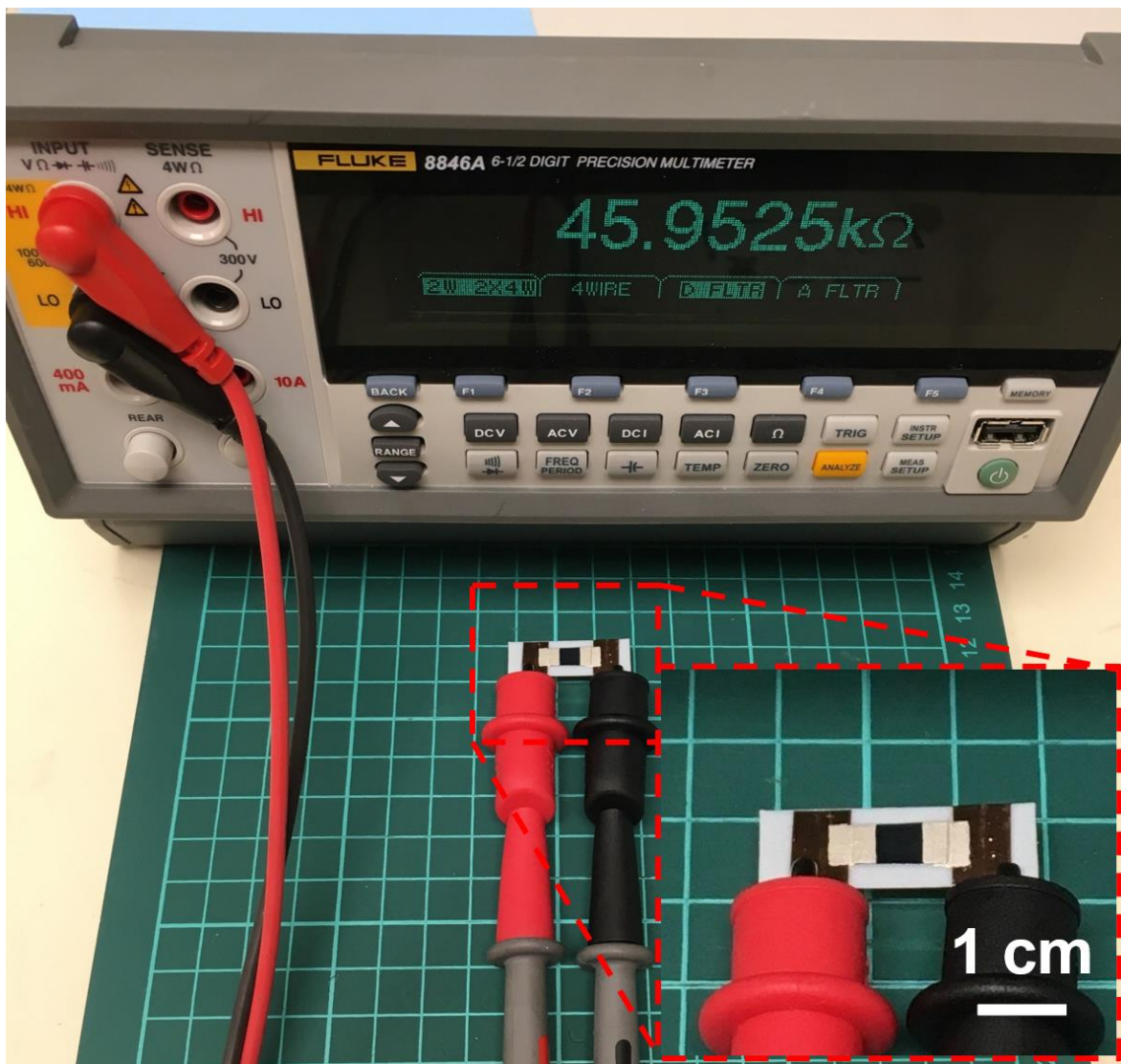


Figure 5 The experimental setup for measuring the resistance of the MIP-PANI electrodes. The scale bar denotes the length of 1 cm, which also corresponds to the dimension of the grids on the cutting mat. The probes are connected to the multimeter with a portion of the wires not shown in this picture.

PFOA/PFOS Detection in Mixed Solutions by PFOA/PFOS Hybrid Imprinted Polyaniline

To synthesize the MIP-PANI with the hybrid templates of PFOA as well as PFOS (PFOA/PFOS-MIP-PANI), the 1 ml of template solution in the synthesis of MIP-PANI was

replaced by two equal amounts of 500 μ l of 100 ppm PFOA and PFOS, followed by the same protocols as mentioned above. NIP-PANI, PFOA-MIP-PANI, PFOS-MIP-PANI, and PFOA/PFOS-MIP-PANI as four different sensing elements were used to fabricate the paper sensors. Mixture samples of PFOA and PFOS were prepared by mixing PFOA and PFOS in aqueous solutions at the combined concentration of 70 ppt. The sample set is listed in Table 1. Because there are three variables of resistivity ratios, PFOA/PFOS concentrations in the sample solutions, and the types of MIP-PANI, a 3D diagram is required to visualize and compare the trends among these parameters. Origin and SigmaPlot were used to plot the 3D diagrams with two different styles emphasizing the standard errors and mean averages, respectively.

Table 1 The denotation of the mixture of PFOA and PFOS sample solutions.

Mixture Denotation		
PFOA:PFOS	PFOA Concentration (ppt)	PFOS Concentration (ppt)
70:0	70	0
60:10	60	10
50:20	50	20
40:30	40	30
30:40	30	40
20:50	20	50
10:60	10	60
0:70	0	70

Fourier-transform Infrared Spectroscopy

The surface of the PFOA-MIP-PANI and PFOS-MIP-PANI sensing element was characterized by an attenuated total reflectance module of an FTIR spectrometer (ATR-FTIR, Nicolet 380, Thermo Scientific, Waltham, MA, USA) to evaluate the potential binding sites for PFOA and PFOS on PFOA-MIP-PANI and PFOS-MIP-PANI. The sensing area on the PANI pad was dispensed by 30 μl of 150 ppt PFOA or PFOS aqueous solution for 30 min and air-dried at 25°C for at least 12 h, followed by an additional vacuum drying process for 2 days and being kept in a silica gel-contained desiccator to ensure the complete removal of moisture in the specimens. The FTIR spectra were based on 64 scans and were collected at 25°C with wavenumbers from 500 cm^{-1} to 4000 cm^{-1} and at a resolution of 2 cm^{-1} .

X-ray Photoelectron Spectroscopy

To evaluate the effectiveness of removing PFC templates from the PANI matrix, the XPS spectra of the surface of PFOA-MIP-PANI and PFOS-MIP-PANI at different fabrication steps (before sonication, after sonication, and after sample dispensing) in the molecular imprinting process were obtained by an XPS instrument (Scienta Omicron, Denver, CO, USA) equipped with Mg/Al X-ray source (DAR 400, Scienta Omicron, Denver, CO, USA). Before XPS measurement, the specimens from the three steps were vacuum dried for at least 4 days to remove any trace level moisture in the specimens. The binding energies of interest in the XPS spectra come from 1s orbitals of fluorine (F1s) and nitrogen atoms (N1s) which were selected in the corresponding modes in the control panel of the XPS system.

Scanning Electron Microscopy

After the exposure to 150 ppt PFOA or PFOS for 30 min, the PFOA-MIP-PANI and PFOS-MIP-PANI strips were air-dried at 25°C for 12 h, followed by further drying under vacuum for additional 4 days. The specimens were then stored in a desiccator with silica gels to keep from environmental humidity. For sample preparation, the specimens were cut into small pieces with a dimension of about 0.5 cm × 0.5 cm and mounted on aluminum stubs using carbon conductive tapes, followed by being pre-treated with Pt/Pd sputtering for improving the conductivity. The surface morphology of PFOA-MIP-PANI and PFOS-MIP-PANI were analyzed by a field-emission scanning electron microscope (LYRA3, TESCAN, Czech Republic) operated at the voltage of 10 kV.

Results

Long-term Stability Test

The resistivity changes of PANI on Xerox polyester paper and Whatman 40 filter paper among a 14-week experimental period from synthesis are shown in Figure 6. For Xerox paper, on the one hand, the resistivity of PANI expressed no significant increase within 11 weeks. On the other hand, the resistivity of PANI on Whatman 40 increased gradually after synthesis. The resistivity of the PANI on the polyester paper substrate in the air was stable, suggesting the remarkable stability of the proposed molecularly imprinted paper sensor.

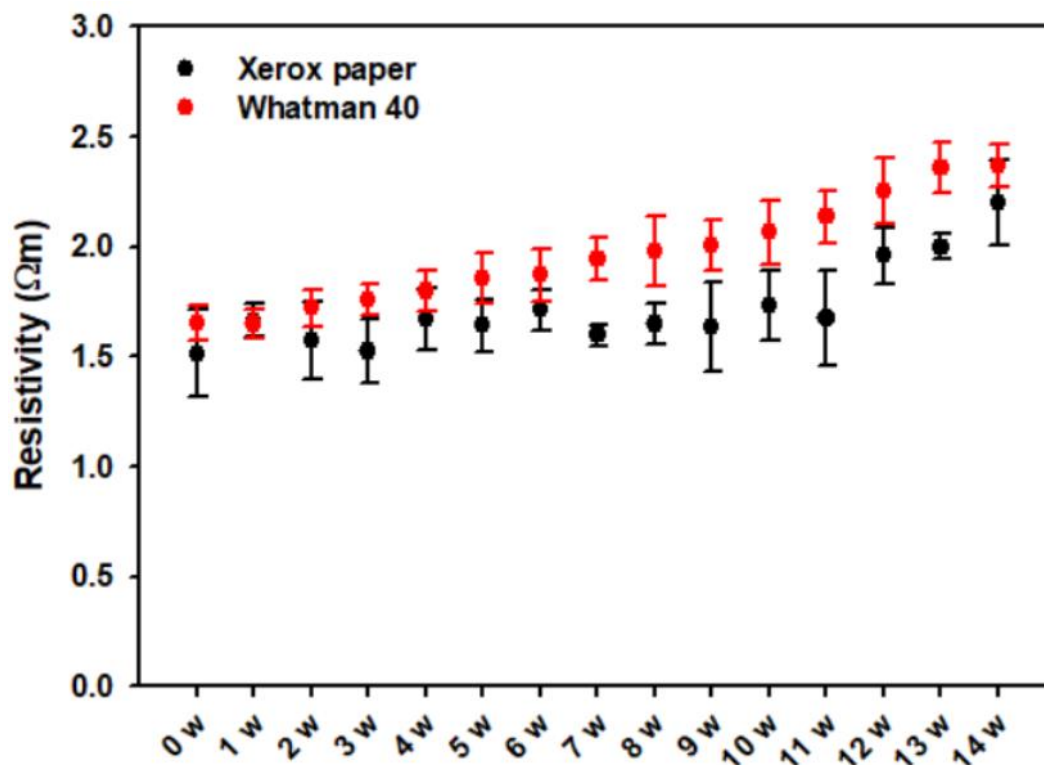


Figure 6 Long-term stability of PANI on paper (n=4). The x axis represents the time from the fabrication of PANI on paper strips.

Fabrication of Molecularly Imprinted Polymer Paper Sensor

To incorporate as much PFOS as possible in molecular imprinting to generate more recognition sites in the PANI matrix, the concentration of PFOS in the template solution was adjusted to 100 ppm, which is close to the solubility of PFOS in water (~550 ppm). In general, concentrations of templates would be larger than concentrations of samples to ensure binding effectiveness. As the photographic images of the integrated paper sensor shown in Figure 4d. PFC-MIP-PANI was evenly deposited on the paper strips. The substrates of paper and stencil are flexible, and the bending motion did not damage the electronic connection of the silver pastes as shown in Figure 4d. In addition, using paper and conductive polymers as the substrate and the

electrodes can achieve high-throughput fabrication and drastically reduce the cost compared to conventional assays. As a result, for potential forms of utilization, this paper sensor is most likely to be fabricated as a fast screening or a single-use testing kit.

PFOA/PFOS Detection in Single Solutions

PFOA and PFOS aqueous solutions with concentrations from 0–500 ppt (pH = 7) were prepared for evaluating the detection performance of PFOA-MIP-PANI and PFOS-MIP-PANI electrodes. The resistivity ratios of NIP-PANI and MIP-PANI electrodes in PFOA and PFOS detection are summarized in Figure 7. A comprehensive summary of the linear regression ranges, the regression equations, the values of the coefficient of determination (R^2), and the estimated limit of detection (LoD) are summarized in Table 2. For PFOA detection, compared with NIP-PANI control, PFOA-MIP-PANI demonstrated a broader linear range up to 200 ppt. At the concentration of PFOA larger than 200 ppt, the resistivity of PFOA-imprinted electrodes reached saturation, and the response remained the same. NIP-PANI control without molecular imprinting treatment possessed a certain ability to detect PFOA at a linear range from 20 to 80 ppt. Beyond 100 ppt, the electrodes were saturated as well. For PFOS, the detecting efficiency was much better than which of NIP-PANI. The linear regression region of PFOS-MIP-PANI electrodes ranged from 20 to 100 ppt, followed by the saturated response. NIP-PANI expressed a poor capability of detecting PFOS with limited increased resistivity upon exposure.

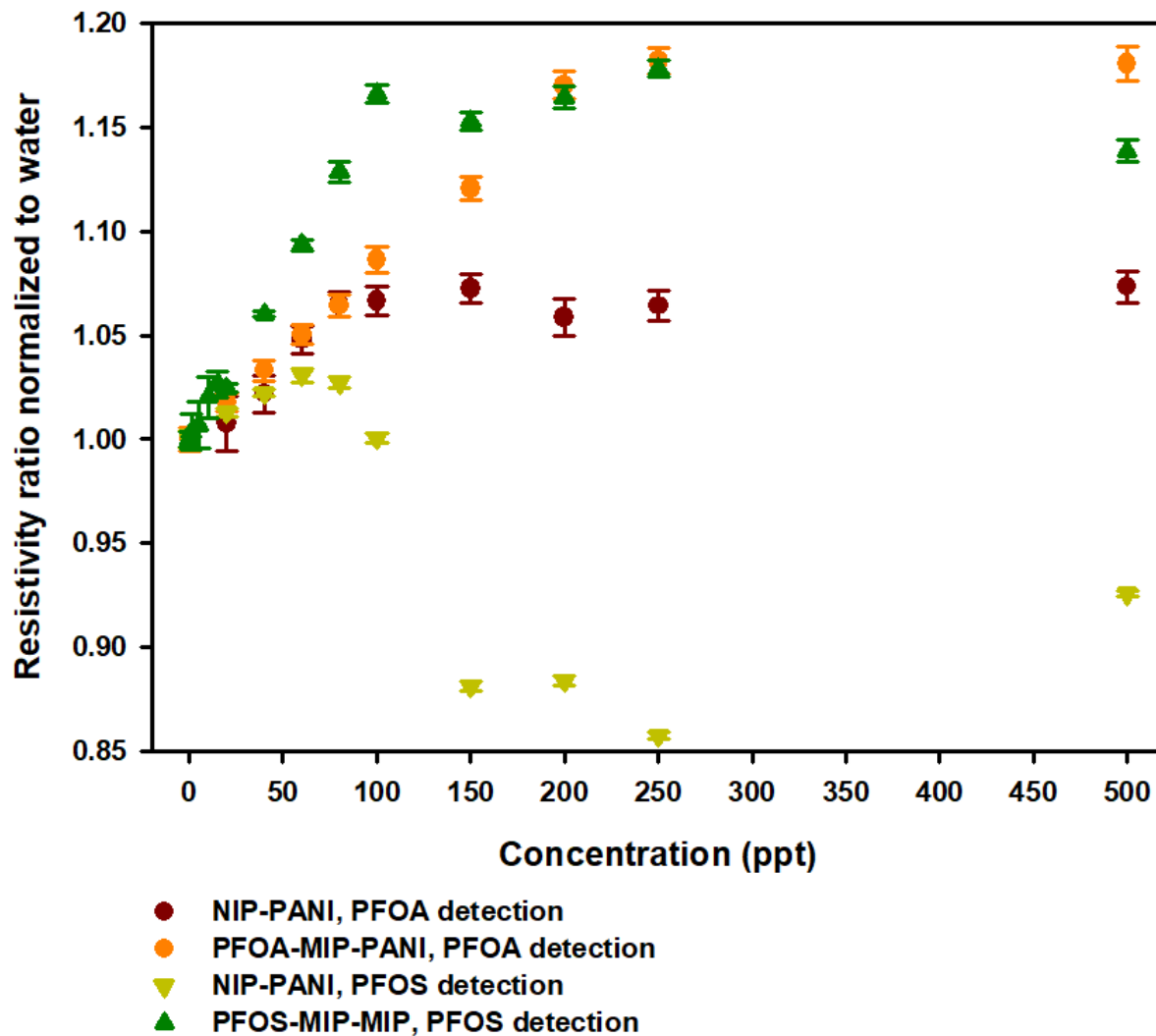


Figure 7 The resistivity ratios of the NIP-PANI and MIP-PANI sensors exposed to PFOA or PFOS. NIP-PANI: non-molecularly imprinted PANI; PFOA-MIP-PFOA: PFOA-imprinted PANI; PFOS-MIP-PANI: PFOS-imprinted PANI. The two types of MIP-PANI exposed to its designated analytes are denoted as PFOA detection and PFOS detection.

Table 2 The summary of the linear regression ranges, regression equations, coefficients of determination (R^2), and limits of determination (LoD) of each sensing element.

Sensing Element	Linear Regression Range (ppt)	Linear Regression Equation	R^2	LoD (ppt)
PFOA Detection				
NIP-PANI	20–80	$y = 0.0008x + 0.9945$	0.9669	21.7
PFOA-MIP-PANI	20–200	$y = 0.0008x + 0.9998$	0.9978	20.6
PFOS Detection				
NIP-PANI	20–60	$y = 0.0005x + 1.0013$	0.9887	27.3
PFOS-MIP-PANI	1–100	$y = 0.0016x + 0.9992$	0.9954	7.1

The calibration curve of PFOA-MIP-PANI and the resistivity data of NIP-PANI as the control for comparison are shown in Figure 8. The resistivity ratio was correlated with the concentration of PFOA in water. According to the linear regression line of PFOA-MIP-PANI, the linear range is from 20 to 200 ppt and saturates from 250 ppt. The NIP-PANI, however, has a lower response than PFOA-MIP-PANI beyond 100 ppt. The coefficients of determination (R^2) of NIP-PANI and PFOA-MIP-PANI are 0.9669 and 0.9978, respectively. The linear regression equation of NIP-PANI is $y = 0.0008x + 0.9945$ of a range from 20 to 80 ppt, and the linear regression equation of PFOA-NIP-PANI is $y = 0.0008x + 0.9998$ of a range from 20 to 200 ppt. The limits of detection of NIP-PANI and PFOA-MIP-PANI are estimated to be 21.7 ppt and 20.6 ppt, respectively. For the control of NIP-PANI, its calibration curve exists a narrower linear range, and the saturation point emerges at the lower concentration compared with which of PFOA-MIP-PANI.

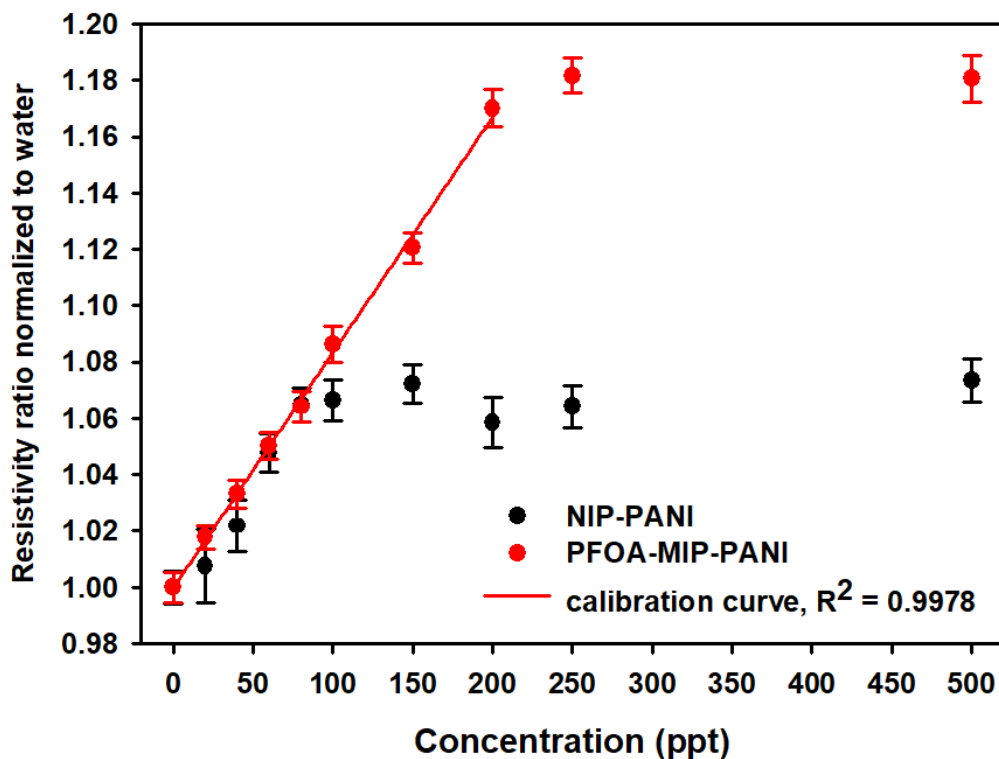


Figure 8 The resistivity ratios of NIP-PANI and PFOA-MIP-PANI paper sensors after dispensing PFOA aqueous samples on the sensors with different concentrations. Each point denotes the average value measured from three devices, and the error bars represent the standard deviations. The red line is the calibration curve with the coefficient of determination (R^2) estimated by using a linear regression model.

The calibration curve and the linear regression model of resistivity ratios of PFOS-MIP-PANI electrodes as a function of the concentration of PFOS are shown in Figure 9. The calibration curve of PFOS-MIP-PANI demonstrates a robust linear relationship between the resistivity ratios and concentrations of PFOS. The linear regression equation of $y = 0.0016x + 0.9992$ and the coefficient of determination (R^2) of 0.9954 were estimated by the linear regression model calculated by SigmaPlot. The linear range is from 1 to 100 ppt. On the other

hand, NIP-PANI demonstrates the estimated linear regression equation of $y = 0.0005x + 1.0013$ with its R^2 value of 0.9887 at a linear range from 20 to 60 ppt. According to Equation 3, the limits of detection of NIP-PANI and PFOS-MIP-PANI are estimated to be 27.3 ppt and 7.1 ppt, respectively.

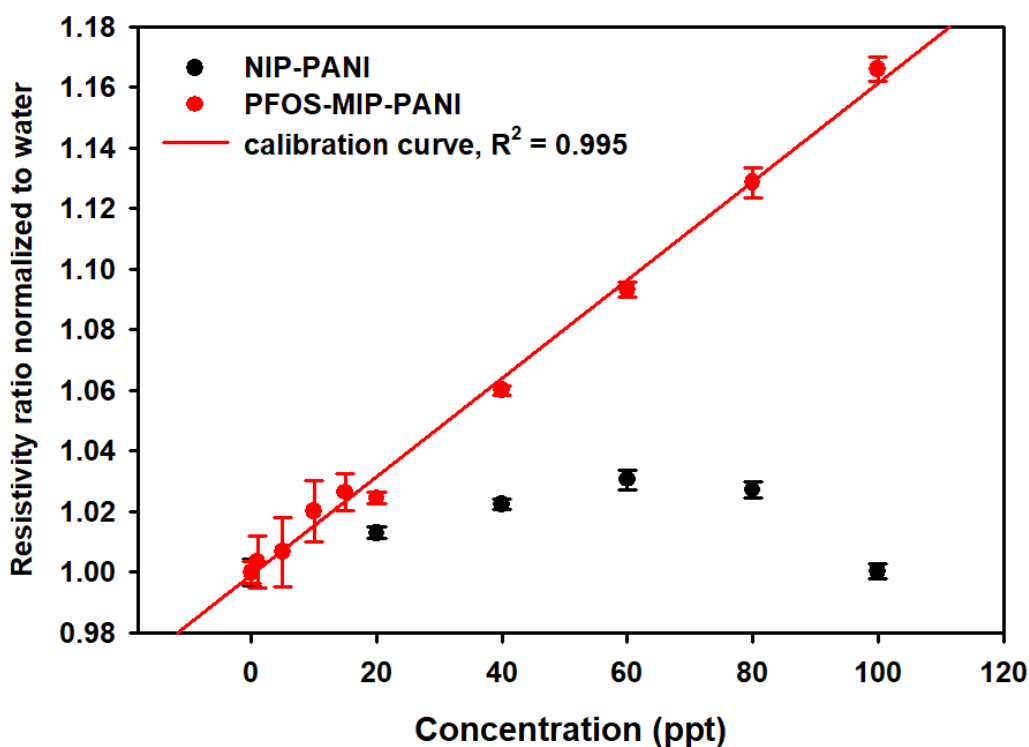


Figure 9 The calibration curve of NIP-PANI and PFOS-MIP-PANI exposed to various concentrations of PFOS aqueous solutions. The resistivity ratios were normalized to the resistivity ratio of DI water. The data points denote the averages of repeating measurements of DC resistance of at least three devices, from which the standard deviations are also calculated and marked as error bars. The red line is the calibration curve with the coefficient of determination (R^2) estimated by using a linear regression model.

PFOA/PFOS Detection in Mixed Solutions and by Hybrid Imprinted Polyaniline

For detecting PFOA and PFOS in their mixed solutions by PFOA-MIP-PANI and PFOS-MIP-PANI and the hybrid imprinted PANI (PFOA/PFOS-MIP-PANI), the identical procedures of the sample dispensing and resistivity measurement were executed for PFOA/PFOS mixtures, and the results are summarized in Figure 10. The three 3D diagrams are based on the same result but plotted by different software to emphasize the standard errors or averages. In Figure 10a plotted by Origin, the resistivity ratios of the three types of MIP-PANI and NIP-PANI exposed to PFOA/PFOS mixtures were demonstrated by a perspective view which is apparent for visualizing the standard errors. The error bars denote the standard deviations of each sample. Some of the data points express large standard errors. Figure 10b and Figure 10c present two 3D plots with the same data set but with different perspective angles to reveal the hindered bars from one side. The bar chart of SigmaPlot makes it easier to compare the mean values of resistivity ratios of the samples. In general, PFOS-MIP-PANI had a larger resistivity response as the concentration of PFOS increased, while PFOA-MIP-PANI seemed to be more responsive to PFOA as the concentration of PFOA increased. However, the trend is not obvious among the series of samples. PFOA/PFOS-MIP-PANI, the hybrid imprinted PANI, showed relatively low responses to all PFOA/PFOS mixtures except the samples with higher PFOS concentrations of 50 ppt and 70 ppt. The trend in NIP-PANI is unobvious as well.

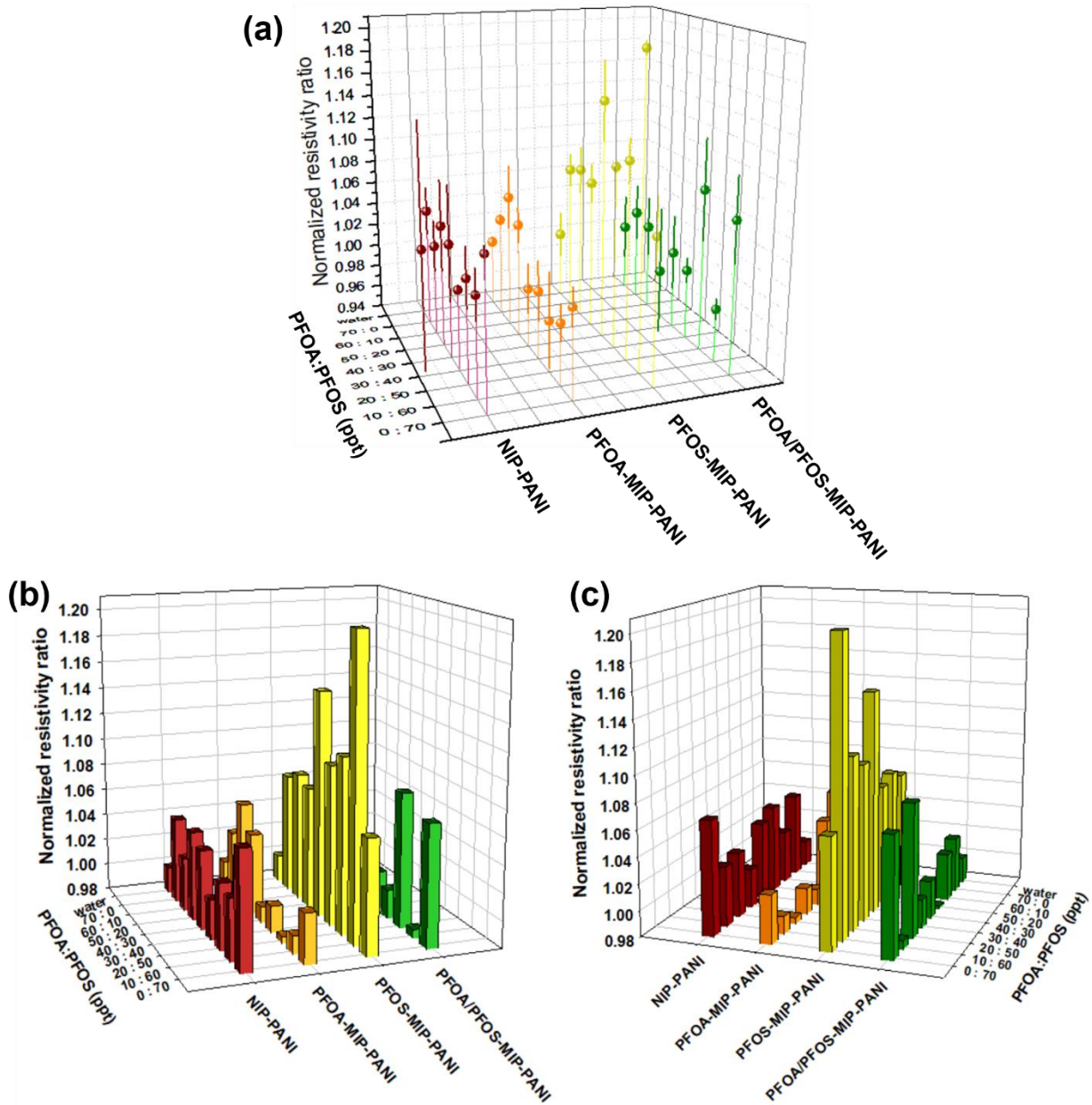


Figure 10 The 3D diagram of resistivity ratios of NIP-PANI, PFOA-MIP-PANI, PFOS-MIP-PANI, and the hybrid imprinted PANI (PFOA/PFOS-MIP-PANI) exposed to PFOA/PFOS mixed solutions at the combined concentration of 70 ppt. (a) The 3D figure is a perspective view plotted by Origin software, showing the error bars calculated from at least three devices. The dots represent the mean averages that came from at least three devices as well. (b, c) The complementary 3D figures plotted by SigmaPlot, which demonstrate two different viewing angles to reveal the concealed bars from the one side of view. All three figures are plotted based on the same set of data.

Attenuated Total Reflection Fourier-transform Infrared Spectroscopy Spectra

The ATR-FTIR spectra of the surface of NIP-PANI and MIP-PANI electrodes are shown in Figure 11. For NIP-PANI after PFOA exposure, the characteristic peak is found at 1571 cm^{-1} , and a redshift from 1571 cm^{-1} to 1577 cm^{-1} presents in the spectrum of PFOA-MIP-PANI. Meanwhile, an additional peak at 1460 cm^{-1} appears in the spectrum of PFOA-MIP-PANI after PFOA exposure. Moreover, a set of characteristic peaks at around 1027 cm^{-1} and 1036 cm^{-1} show in the spectra of PFOA-MIP-PANI and NIP-PANI as well, where a redshift also presents in the spectrum of PFOA-MIP-PANI after being exposed to PFOA.

For PFOS detection, the ATR-FTIR spectra (Figure 12) of the surface of PANI electrodes after being exposed to PFOS show a characteristic peak at around 1570 cm^{-1} and a redshift from 1570 cm^{-1} to 1576 cm^{-1} while molecular imprinting process was applied to the PANI. In addition, the spectrum of PFOS-MIP-PANI after PFOS exposure shows a characteristic peak at 1375 cm^{-1} , which is not found in the spectrum of NIP-PANI. Another group of characteristic peaks at around 1015 cm^{-1} and 1035 cm^{-1} also present in the spectra of NIP-PANI and PFOS-MIP-PANI, respectively.

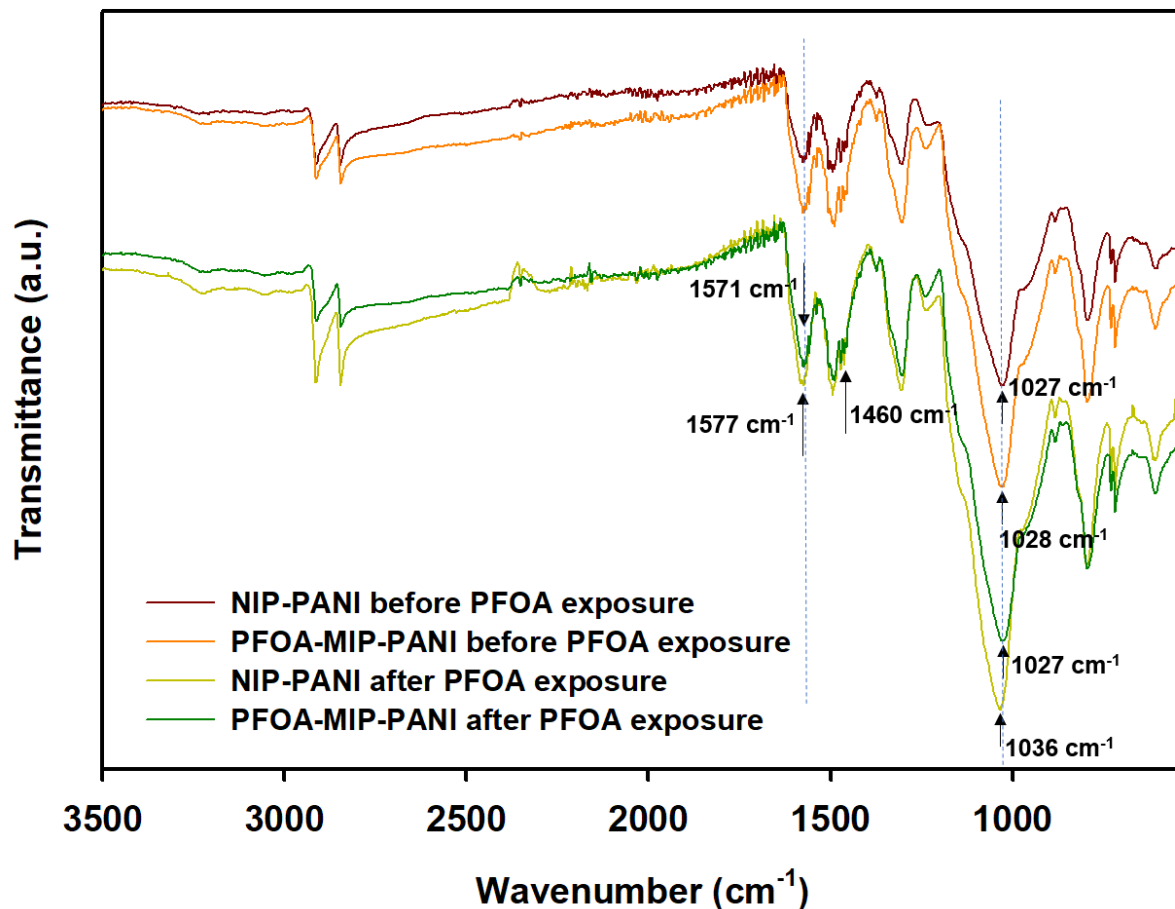


Figure 11 The ATR-FTIR spectra of the surface of PFOA-MIP-PANI and NIP-PANI. NIP-PANI denotes the polyaniline synthesized in the absence of PFOA templates while the template removal process including sonication was still performed. The y axis based on the transmission mode has been adjusted in order to compare the wavelengths of the characteristic peaks. The arrows point out the characteristic peaks with their corresponding wavenumbers. The blue dotted lines are provided for comparing the potential redshifts.

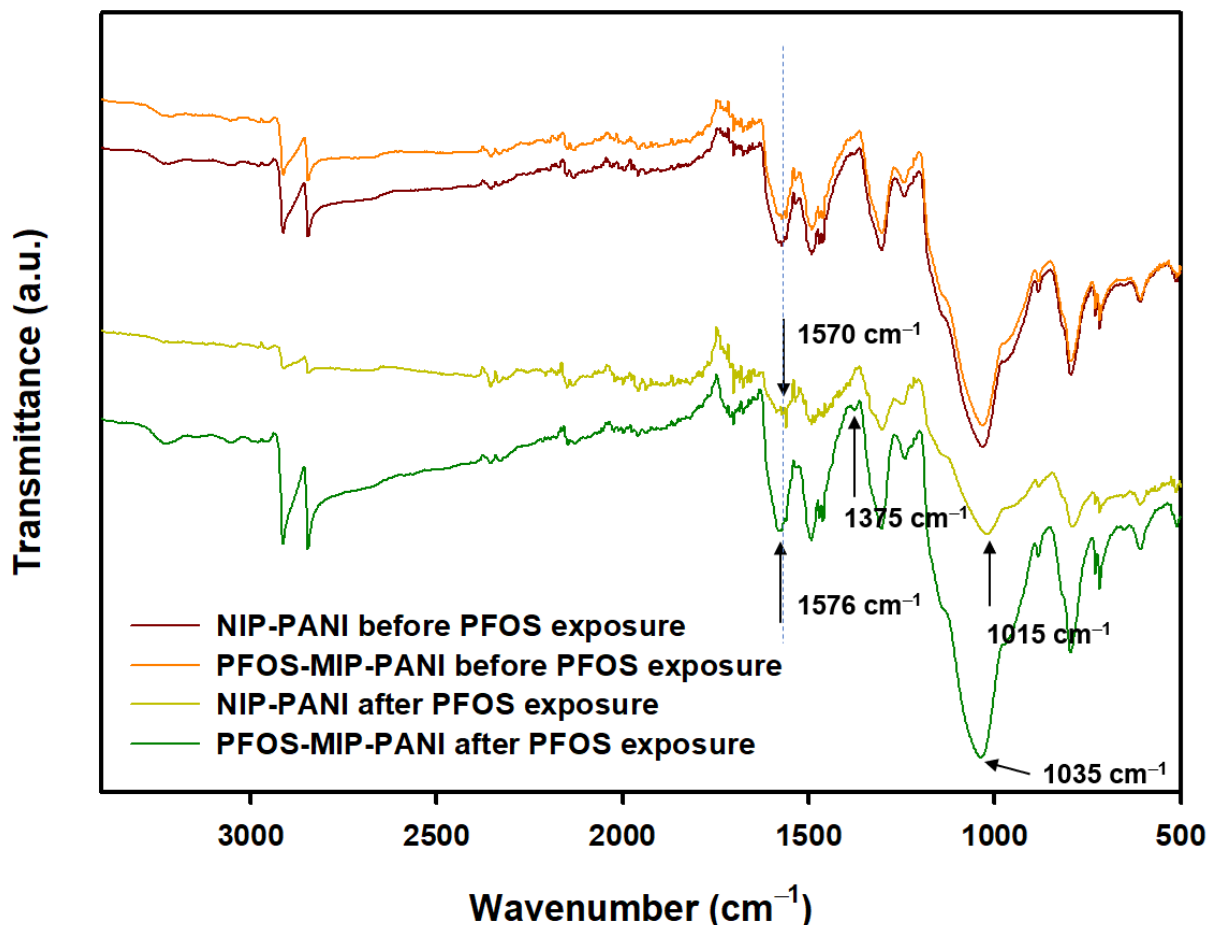


Figure 12 The ATR-FTIR spectra of the surface of PFOS-MIP-PANI and NIP-PANI. NIP-PANI denotes the polyaniline synthesized in the absence of PFOS templates while the template removal process including sonication was still performed. The y axis based on the transmission mode has been adjusted in order to compare the wavelengths of the characteristic peaks. The arrows point out the characteristic peaks with their corresponding wavenumbers. The blue dotted line is designated for comparing the potential redshift.

X-ray Photoelectron Spectroscopy Spectra

The XPS spectra of the surface of PFOA-MIP-PANI, PFOS-MIP-PANI, and NIP-PANI are shown in Figure 13. Two sets of spectra representing the binding energies from 1s atomic

orbitals of fluorine (F1s) and nitrogen (N1s) atoms are presented. For PFOA-MIP-PANI and PFOS-MIP-PANI before sonication, the spectra of F1s binding shows peaks at 688 eV and 684 eV; however, the peaks at 684 eV disappear after the MIP-PANI strips were treated by sonication and reappeared after the exposure to PFOA or PFOS aqueous solution. On PFOS-MIP-PANI, both the peaks at 688 eV and 684 eV disappear after the sonication process (the orange line in Figure 13b).

The XPS spectra of the NIP-PANI sample as the control group show a little difference between PFOA and PFOS experiments. In the PFOS experiment, the spectrum of NIP-PANI shows almost no peak at 688 eV after PFOS exposure, and the peak at 684 eV is not as significant as the peak of PFOS-MIP-PANI (the green line in Figure 13b). Such observation does not exist in the PFOA experiment where both the NIP-PANI control and PFOA-MIP-PANI reveal two characteristic peaks at 688 eV and 684 eV.

In addition, the N1s binding spectra show peaks at around 400 eV for all the processing conditions and types of MIP-PANI electrodes. After the exposure of PFOA, the spectra of PFOA-MIP-PANI and NIP-PANI show minor and nearly parallel redshifts to the lower binding energy of 399eV when compared with the peaks of PFOA-MIP-PANI before the exposure of PFOA (the maroon and orange lines in Figure 13c). In the meantime, for PFOS-MIP-PANI after PFOS exposure, the spectrum (the khaki line in Figure 13d) exhibits a redshift of the peak to 399 eV when compared with the peaks of PFOS-MIP-PANI before the exposure of PFOS and NIP-PANI control. The spectrum of PFOS-MIP-PANI demonstrates a more significant redshift than that of NIP-PANI.

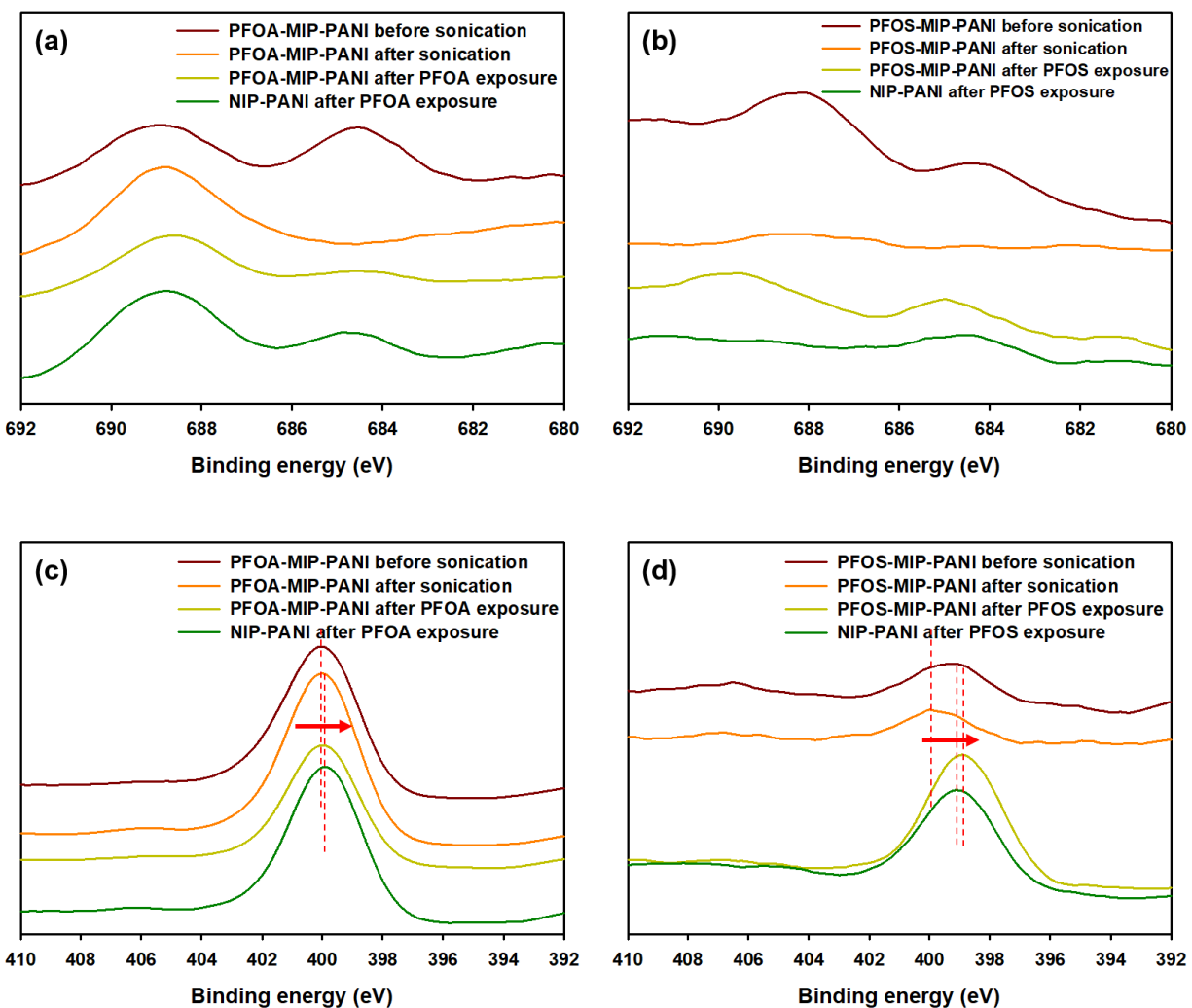


Figure 13 XPS spectra of the surface of MIP-PANI electrodes in each processing step of molecular imprinting and PFOA/PFOS exposure. Non-molecularly imprinted PANI (NIP-PANI) served as control. (a, b) F1s spectra (c, d) N1s spectra. The arrows represent the direction of redshift in binding energy. The y axis based on counts per second has been adjusted to the arbitrary unit in order to compare the binding energies of different samples.

Surface Morphology of MIP Electrodes by Scanning Electron Microscopy

The SEM images of the NIP-PANI and PFOA-MIP-PANI electrodes are shown in Figure 14. Before sonication, PFOA-MIP-PANI exhibits many separate and embedded spheres that might be nanocrystalline of PANI, while NIP-PANI shows irregular clusters (Figure 14a, d). In Figure 14b,e, after the sonication, the NIP-PANI and PFOA-MIP-PANI electrodes do not maintain a significant difference in their surface morphology, but some of the previous characteristic clusters and separate spheres diminish or even vanish. For NIP-PANI and PFOA-MIP-PANI after the exposure to PFOA, their SEM images are shown in Figure 14c,f, respectively. The irregular clusters of NIP-PANI in Figure 14a do not present on those surfaces after PFOA exposure (Figure 14c,f.). Instead, the individual spherical crystalline with brilliant color reappears on both NIP-PANI and PFOA-MIP-PANI. Overall, for the PFOA detection experiment, SEM does not provide noticeable results in microstructural changes.

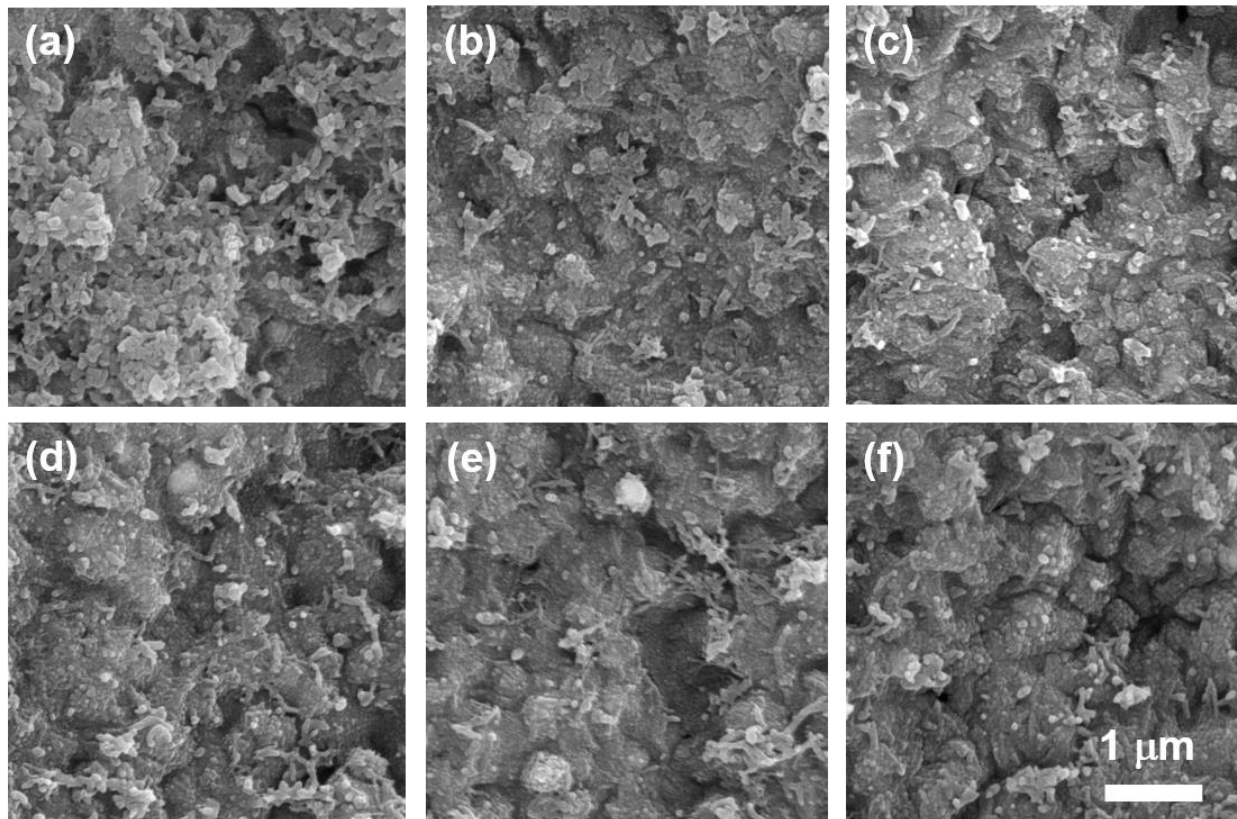


Figure 14 SEM images of the surface morphology of (a) NIP-PANI before sonication; (b) NIP-PANI after sonication and before the exposure to PFOA; (c) NIP-PANI after the exposure to PFOA; (d) PFOA-MIP-PANI before sonication; (e) PFOA-MIP-PANI after sonication and before the exposure to PFOS; (f) PFOA-MIP-PANI after the exposure to PFOS. The scale bar denotes 1 μm in length.

The surface morphology of PFOS-MIP-PANI and NIP-PANI electrodes is shown in Figure 15. Before the sonication treatment of the surface, PFOS-MIP-PANI exhibits a continuous phase with a few clusters and several nanosized spherical crystals of PANI, while NIP-PANI reveals irregular clusters as well as spherical crystals of PANI without a relatively continuous microstructure (Figure 15a, d). In Figure 15b,e, after the sonication, NIP-PANI and PFOS-MIP-PANI electrodes do not maintain a significant difference in surface morphology. The SEM images of the surfaces of NIP-PANI and PFOS-MIP-PANI after the exposure to PFOS are

shown in Figure 15c,f, respectively. NIP-PANI shows the morphology similar to the surface before sonication (Figure 15a) and before the exposure to PFOS (Figure 15b), upon which several fragmented and irregular clusters, as well as nanosized spherical crystals, exist. However, the continuous phase of clusters of a larger size than appearing on the surface of NIP-PANI after exposure to PFOS reappear on PFOS-MIP-PANI as shown in Figure 15f. The surface with the large and continuous domain of clusters and spherical nanocrystalline on PFOS-MIP-PANI in Figure 15f is comparable with the surface before sonication where PFOS templates were embedded in the PANI matrix.

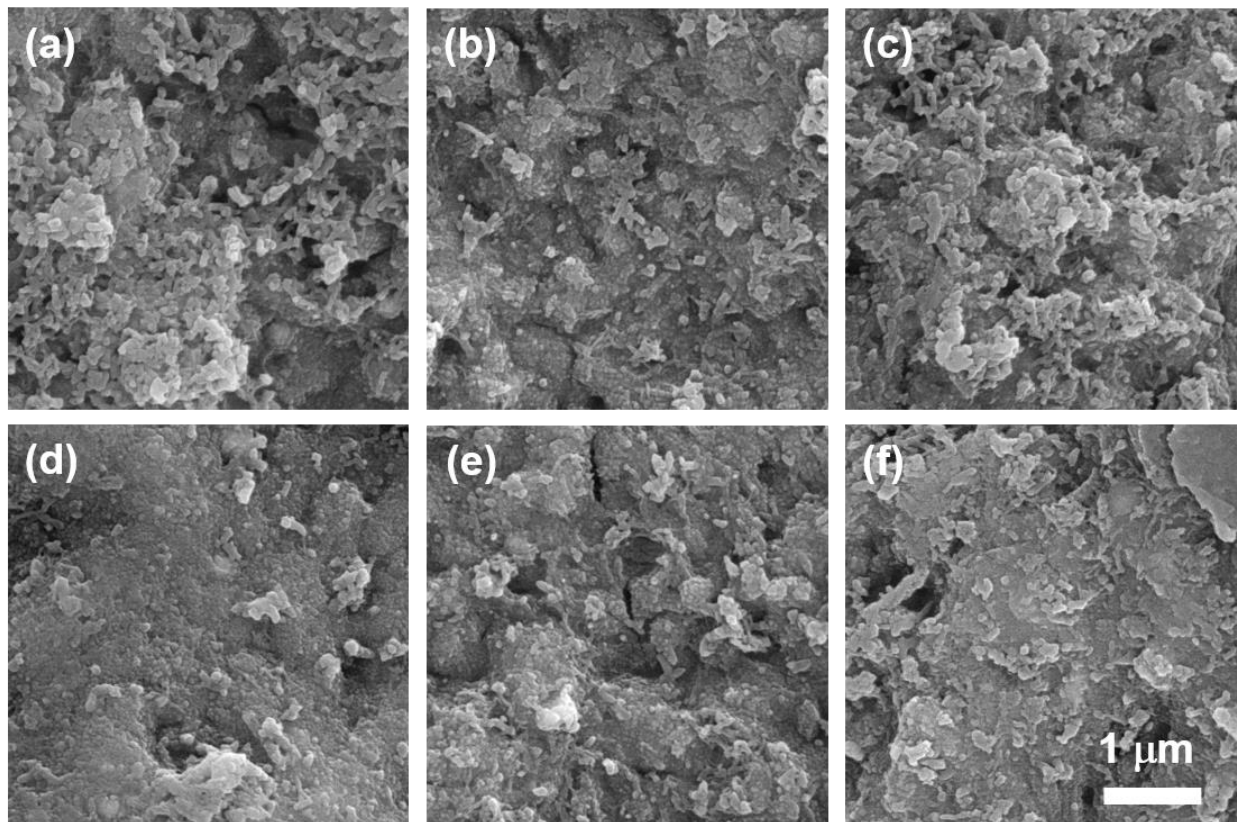


Figure 15 SEM images of the surface morphology of (a) NIP-PANI before sonication; (b) NIP-PANI after sonication and before the exposure to PFOS; (c) NIP-PANI after the

exposure to PFOS; (d) PFOS-MIP-PANI before sonication; (e) PFOS-MIP-PANI after sonication and before the exposure to PFOS; (f) PFOS-MIP-PANI after the exposure to PFOS. The scale bar denotes 1 μm in length.

Selectivity among Relevant Perfluorinated Compounds

The selectivity of the PFOA-MIP-PANI paper sensor to PFOA and other comparable PFCs with similar functionality and chemical structures including PFBA, PFHxA, and PFOS are shown in Figure 16. At the concentration of 70 ppt which is the maximum tolerance in drinking water suggested by USEPA, the PFOA-MIP-PANI demonstrated the resistivity ratio with significant difference ($p < 0.05$) from other types of PFCs. PFCs with the longer aliphatic groups of six or eight carbons demonstrate slightly higher resistivity ratios; however, the significance still exists as shown in Figure 16, suggesting the great selectivity to PFOA among other comparable PFCs of PFBA, PFHxA, and PFOS.

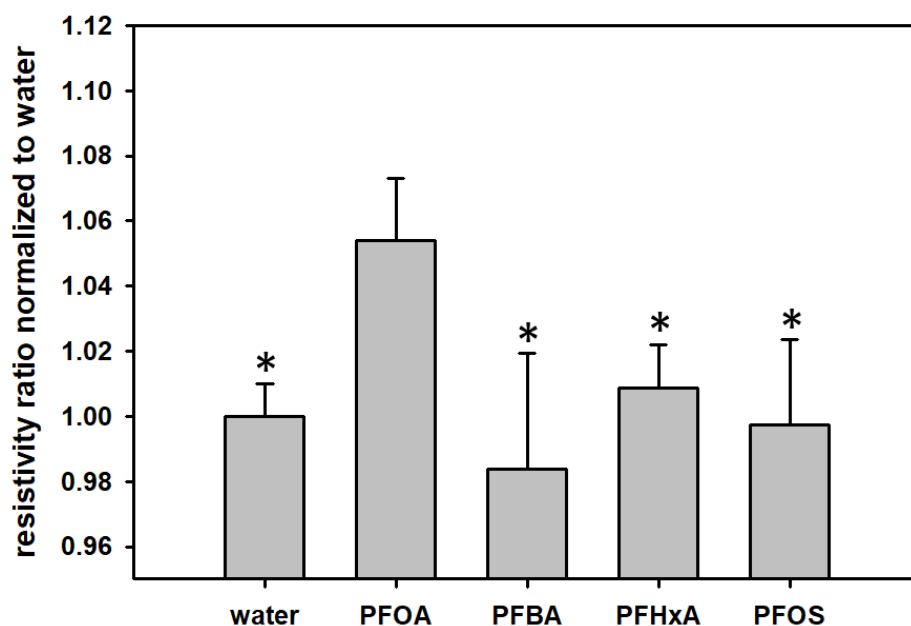


Figure 16 The selectivity of PFOA-MIP-PANI to PFOA, PFBA, PFH_xA, and PFOS. The concentration of each PFC in the aqueous sample was 70 ppt. The bars denote the average values of DC resistivity ratios normalized to which of water. The standard deviations as error bars were calculated from three devices. The asterisks represent the statistical significance ($p < 0.05$) compared with the ratio of PFOA.

The selectivity of PFOS-MIP-PANI to PFOS and the other three relevant PFCs of PFBA, PFH_xA, and PFOA is shown in Figure 17. After exposure to various PFC aqueous solutions with a concentration of 70 ppt, PFOS-MIP-PANI demonstrates the largest resistivity ratio to PFOS among other PFC chemical compounds. PFOS-MIP-PANI also indicates statistical significance ($p < 0.05$) between PFOS and relevant PFCs, indicating remarkable selectivity. The average responses of the other three types of PFCs slightly increase as the number of carbon atoms in the tail group increases.

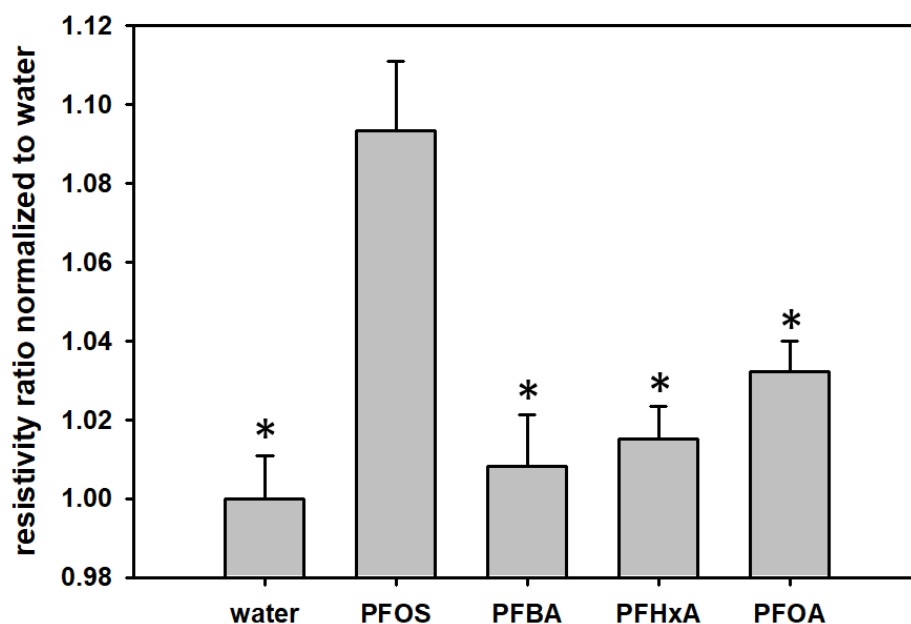


Figure 17 The selectivity of PFOS-MIP-PANI to PFOS, PFBA, PFHxA, and PFOA. The concentration for each chemical in the aqueous samples was 70 ppt. The data were normalized to water resistivity. Each bar denotes the average of DC resistivity ratios measured from three devices, and the standard deviations are also marked as the error bars. The asterisks represent significance ($p < 0.05$) lower than the response of PFOS.

Discussion

The long-term stability study was to validate the synthesis procedures and the stability of the synthetic PANI platform we used. The remarkable durability of the polyaniline synthesized on the polyester paper strips may be attributed to the hydrophobic surface and the greater affinity with aniline monomers, resulting in a dense and continuous film on the polyester paper substrate rather than Whatman 40 filter paper. As a result, PANI on the polyester paper might have stronger intermolecular interaction and contribute to the durability of the electrodes. The relatively hydrophobic paper additionally allows the strips to remain whole in the solution

without being disintegrated by vigorous stirring. There are minor deviations found in Figure 6, which may be due to changes in temperature and humidity that are less than 10% of resistivity.

According to the technical fact sheet released by USEPA, the suggested environmental tolerance of a combined concentration of PFOA and PFOS in drinking water is 70 ppt [41], which locates on the linear regression range of the calibration curves for molecularly imprinted PANI for both PFOA and PFOS detection. From the calibration curves, these devices can determine whether the concentration of PFOA or PFOS in aqueous solutions exceeds the maximum tolerance or not. As a result, the molecular imprinting process provides a promising method to remarkably improve the detection performance of PANI to PFOA and PFOS.

The calibration curve reveals a positive and linear correlation of normalized resistivity ratios as a function of PFOA or PFOS concentrations in aqueous solutions, which means that the resistance of PFOA-MIP-PANI and PFOS-MIP-PANI electrodes increased after exposure to PFOA and PFOS. The larger standard deviation of the responses at the lower concentrations may result from the slight variation in resistance. The extremely low concentration may also limit the association between PFC and PFC-MIP-PANI and prolong the time for reaching equilibrium, increasing the standard deviation. PANI itself may possess a certain ability to react with PFOA due to the electrostatic interaction, however, the linear range is limited according to the early saturation. Therefore, PANI with molecularly imprinted structures provides a broader linear range for detecting PFOA compared with which of the pristine matrix, suggesting better effectiveness.

ATR-FTIR uses a reflective mode to collect spectra down to a strictly limited depth from the surface, providing an effective tool for surface characterization. The relevant characteristic peaks of PANI, PFOA, and PFOS are summarized in Table 3 [56-62]. According to the ATR-

FTIR spectra in Figure 11, the characteristic peak at around 1571 cm^{-1} represents C=N stretching of the quinoid form of aromatic rings in the PANI matrix [56, 57, 62]. The aromatic rings have resonance structures as quinoid and benzenoid forms while electric charges are transferred through the PANI backbones. Lal et al. found that the quinoid rings of PANI were attributed to the intermolecular interaction between multiwall carbon nanotubes (MWCNT) and the PANI matrix, further improving the thermal stability as the glass transition temperature of the MWCNT-PANI nanocomposite increased [63]. Therefore, this redshift indicates the potential intermolecular interaction and hybridization between PFOA and PFOA-MIP-PANI, and that possible binding sites could be located on quinoid rings in the PANI matrix. In addition, the characteristic peak at 1460 cm^{-1} may result from C=C stretching of aromatic rings and N=N stretching [62], or it can be the splitting of the native peak of benzenoid rings associated with the quinoid-benzenoid transition upon the PFOA exposure. Moreover, The characteristic peak at around 1036 cm^{-1} may suggest the vibrational stretch of C-C single bonds of PFOA [60, 61] on PFOA-MIP-PANI. Nevertheless, this type of peak may merely represent the C-H bond in-plane bending of the 1,4-aromatic ring [58] or N-H stretching in charged polymers of PANI [57], especially that the wavelength is located in the fingerprint region lower than 1200 cm^{-1} where the relevance of characteristic peaks and functional groups is uncertain and the molecular vibration modes play the more critical role [64]. In this situation, the spectrum of PFOA-MIP-PANI after PFOA exposure additionally has a redshift at 1036 cm^{-1} , indicating the reactive sites locate on aromatic rings. As a result, this specific peak may be less valuable in determining the functional groups but with potential in fingerprint analysis due to the uniqueness of molecular vibration.

Table 3 The reference of the characteristic peaks in the FTIR spectra of PANI, PFOA, and PFOS. Adapted from [56-62].

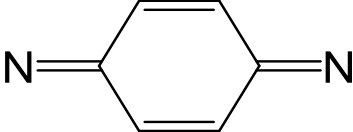
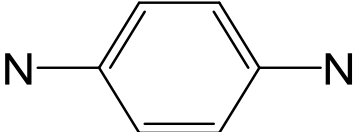
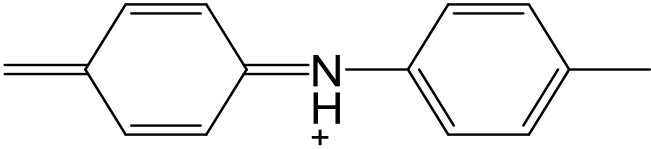
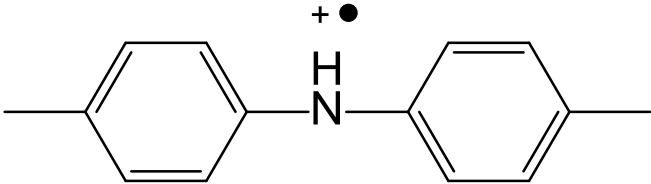
Wavenumber (cm ⁻¹)	Assignments
1574	Quinoid ring-stretching [56, 62] 
1478	Benzenoid ring-stretching [56, 62] 
1445–1451	C=C or N=N stretching [62]
1329, 1372	CF ₂ axial stretching of PFOS [59]
1319, 1363	CF ₂ axial stretching of PFOA [59]
1354	C-N stretching of aromatic amines [57]
1312	C-N stretching of secondary aromatic amines [57, 62]
1286	C-N stretching of benzenoid rings [56]
1267, 1283	CF ₂ vibrational stretching of PFOS [59]
1248, 1257	C-N stretching in the polaron form of PANI emeraldine salt [57, 62]
1243	C-N stretching of benzenoid rings [56] Asymmetric stretching of CF ₂ + R-SO ³⁻ of PFOS [59]
1238	CF ₂ asymmetric stretching of PFOA [59, 61]
1215	R-SO ³⁻ asymmetric stretching of PFOS [59]
1204	Asymmetric stretching of CF ₂ + CF ₃ of PFOA [59, 61]
1152	CF ₂ symmetric stretching of PFOS [59]

Table 3 (Continued) The reference of the characteristic peaks in the FTIR spectra of PANI, PFOA, and PFOS.

Wavenumber (cm ⁻¹)	Assignments
1149	CF ₂ symmetric stretching of PFOA [59]
1148, 1167	C-H in-plane deformation on quinoid rings or (quinoid)=NH ⁺ -(benzenoid)
	
	or (benzenoid)-NH ⁺ •-(benzenoid) [62]
	
1079	N-H stretching in charged polymers [57]
1066	R-SO ³⁻ symmetric stretching of PFOS [59]
1045	HSO ⁴⁻ or SO ³⁻ on aromatic rings [62]
1037	C-C vibrational stretching of PFOS [59]
1014, 1102	C-C vibrational stretching of PFOA [59-61]
1031	C-H in-plane bending of 1,4-rings [58]
1010	N-H stretching in charged polymers [57]
795	C-C and C-H of benzenoid rings [56]

In the meantime, for PFOS detection, its ATR-FTIR spectra as shown in Figure 12 also suggest the redshift of quinoid rings as the potential binding sites in the molecularly imprinted

structure. The characteristic peak at 1375 cm^{-1} of PFOS-MIP-PANI indicates the axial stretch of CF_2 binding [59], which suggests the presence of PFOS on MIP-PANI electrodes whereas NIP-PANI does not present the similar functional group. The peaks at around 1035 cm^{-1} may be attributed to the vibrational C-C stretch of PFOS [59] or the sulfonate group absorbed on the aromatic rings of PANI [62, 65], indicating additional evidence of the capitulation of PFOS molecules by the recognition sites generated by the molecular imprinting process. Again, such the peak contains complex information from various sources as mentioned above [58], making the assignment of corresponding chemical bonds trickier and more challenging.

In the molecular imprinting process, templates coexist with monomers in the solution during polymerization, after which templates must be removed and leave cavities as recognition sites to target molecules. Therefore, the procedure of removing template molecules from a polymer matrix plays an important role in synthesizing MIPs. Sonication in a cosolvent of acetic acid/methanol was utilized to extract PFOS templates from the PANI matrix. Herein, the XPS experiments were to investigate the efficiency of PFOS template removal from the PANI substrate. Table 4 [66-76] lists the XPS reference peaks in F1s spectra of various species and binding energies. According to the spectra representing F1s bonding as shown in Figure 13a and Figure 13b, because fluorine atoms do not exist in the chemical structure of PANI, the peaks indicate the presence of PFOA or PFOS on the surface of MIP-PANI electrodes. Before sonication, PFOS-MIP-PANI contained PFOS templates and its F1s spectrum (Figure 13b) shows a peak at around 688 eV which represents aliphatic fluorine (CF_2) bonding [66, 77]. After sonication in the cosolvent, the corresponding CF_2 peak in the F1s spectrum disappears, suggesting the successful removal of PFOS templates from PFOS-MIP-PANI. Once the PFOS-MIP-PANI was exposed to PFOS, PFOS molecules were captured by the molecularly imprinted

recognition sites in PFOS-MIP-PANI proven by the reemerged CF₂ peak in the XPS results. In contrast, NIP-PANI did not show the aliphatic fluorine peaks due to the lack of specific binding cavities.

Table 4 The binding energies of the 1s orbital of fluorine (F) in the FTIR spectra of various chemicals. Adapted from [66-76].

Element	Species	Binding Energy (eV)
F	SF ₆ [70]	690.3
	(-CF ₂ CF ₂ -) _n [71]	689.9
	-CF ₃ [66]	689.2
	(-CHFCHF-) _n [72]	689.1
	(-CF ₂ CH ₂ -) _n [72]	688.8
	(-CHFCH ₂ -) _n [72]	688.0
	PF ₆ [73]	687.8
	AlF ₃ [74, 75]	687.7
	Fluorine in vinyl polymers [69]	687.0
	AlF ₃ •3H ₂ O [67]	686.3
	SiF ₆ [76]	686.3
	BF ₃ [67]	686.1
	Metallic phenyl ligands [68]	686.0
	Metallic fluoride [66, 67]	682.4–687.8

Nevertheless, such the principle does not perfectly apply to the F1s spectra of PFOA-MIP-PANI (Figure 13a). Only the peak at 684 eV disappears and reappears after sonication and PFOA exposure. In principle [66, 78], the characteristic peak at around 684 eV represents metallic or ionic fluoride. Because the secondary binding of electrostatic attraction force is not strong enough to break covalent C-F bonds, the PFOA was unlikely to be decomposed into fluorine ions while being detected by PFOA-MIP-PANI. Metallic-phenyl coordination [68] and fluorine in vinyl polymers [69] could have lower F1s binding energies, but the detailed reason is yet to be determined. Further investigation and peak deconvolution could also be helpful to recover the potential corresponding species [79]. Overall, the XPS spectra can still provide the supplemental view for visualizing the molecular imprinting processes which are usually difficult to be described by solely narrative description.

Additionally, according to the nitrogen spectra in Figure 13c and Figure 13d representing the N1s binding in PANI, the peak-shifting to the lower binding energy after exposure to PFOA or PFOS suggests the potential secondary bonds between PANI and PFOA/PFOS. In contrary to F1s binding, N1s binding only presents in the PANI matrix. The electrostatic force between negatively charged fluorine atoms as well as acid functional groups in PFCs and positively charged nitrogen atoms in PANI may generate induced-dipole moments on N1s binding and weaken the original binding energy within PANI, causing the redshift of the XPS spectra. In other words, nitrogen atoms in PANI may serve as the key parameter for recognizing target PFCs. The values of 1s binding energies of various organic nitrogen species are summarized in Table 5 [66, 67, 69, 80-86]. Depending on the resonance structures, PANI could have N1s XPS peaks combined with binding energies ranging from 398.5 eV (imine, C=N-C) to 399.5 eV (amine, C-NH-C) and 401.5 eV (protonated imine, C=(NH⁺)-C) [80]. In Figure 13c and Figure

13d, after PFOA or PFOS was captured, the redshift towards the lower energy implies that the PANI expressed more affinity with imine structures. Particularly, PFOS-MIP-PANI shared more characteristics of imine functional groups than NIP-PANI did (Figure 13d), and the tendency of imine structures agrees with the quinoid rings referred to the ATR-FTIR spectra in Figure 11 and Figure 12. Therefore, quinoid rings and nitrogen atoms could be the functional groups of the recognition sites that allow MIP-PANI to detect PFOA and PFOS.

Table 5 The binding energies of the 1s orbital of organic nitrogen (N) in the FTIR spectra of various chemicals. Adapted from [66, 67, 69, 80-86].

Element	Species	Binding Energy (eV)
N (organic)	Nitro, -NO ₂ [81]	405.7
	Malononitrile, N≡C-CH ₂ -C≡N [81]	402.3
	Protonated amine, C=(NH ⁺)-C [80]	401.5
	Imide, (C=O)-N-(C=O) [82]	400.6
	N-(C=O)-O- [85]	400.3
	N-(C=O)-N [66]	399.9
	Amide, N-(C=O)- [66]	399.7
	Leucoemeraldine [80]	399.5
	N within aromatic ring (like pyridine) [83, 84]	399.5
	Nitrile, -C≡N [66, 86]	399.5
	Amine, C-NR ₂ [80]	399.4
	Imine, C=N-C [80]	399.0
	Imine, R=N-R [80]	398.3

Moreover, the existence of the characteristic peak at 688 eV of the F1s spectra of the NIP-PANI control as shown in Figure 13a might explain the certain capability of detecting PFOA by NIP-PANI because only the presence of PFOA would contribute to the peaks in F1s spectra. This inference might also correspond to the N1s spectra as shown in Figure 13c, in which PFOA-MIP-PANI and NIP-PANI retain a similar level of redshift. For PFOS detection, NIP-PANI did not possess an adequate response to PFOS, which might result in its weaker XPS peak at 688 eV in Figure 13b. On the other hand, the redshift is more obvious in Figure 13d (PFOS detection) than in Figure 13c (PFOA detection), indicating that the N1s binding within the PANI matrix of PFOS-MIP-PANI after PFOS exposure was weaker than which in PFOA-MIP-PANI. In other words, the intermolecular interaction between PFOS and PFOS-MIP-PANI was stronger. This might be related to the larger slope of the calibration curve of PFOS as shown in Figure 7, which means that PFOS molecules were captured by PFOS-MIP-PANI more easily; however, its calibration curve reached the saturation earlier than that of PFOA-MIP-PANI. The reasons might be attributed to the smaller number of recognition sites on PFOS-MIP-PANI caused by the dynamics or kinetics between PFCs and the PANI matrix during copolymerization. The detailed mechanism deserves future attention.

Since PFOA and PFOS are both small molecules on a nearly atomic scale, the theoretical cavities created from the molecular imprinting process are extremely difficult to be observed under SEM. For NIP-PANI and MIP-PANI exposed to PFOA, the separate spherical structure might imply the recognition sites of PFOA templates embedded in PANI matrix (Figure 14a,d) because such the specific structure was removed after sonication (Figure 14b,e) and presented again after PFOA exposure (Figure 14c,f). For NIP-PANI, the surface structure was refined from irregular clusters (Figure 14a) to spheres (Figure 14b) by sonication process, which might be

caused by the vibrational energy separating the primitive structure apart. After PFOA exposure, the separate spheres reappeared as shown in Figure 14c, corresponding to the certain capability of detecting PFOA by NIP-PANI. This implies that NIP-PANI and MIP-PANI capturing PFOA molecules might reveal structures as individual spheres.

Simultaneously, the presence of PFOS during polymerization may result in the structural refinement of irregular and fragmented clusters, leading to a continuous phase embedding the PFOS templates in the PFOS-MIP-PANI before being treated with an ultrasonic bath (Figure 15d). The removal process disposed of the PFOS templates and brought the surface morphology back to fragmented clusters (Figure 15e). Finally, after dispensing the sample solutions on the surface, the PFOS-MIP-PANI recognized and captured PFOS molecules as if they were embraced after polymerization, causing a continuous phase to emerge again (Figure 15f). On the contrary, NIP-PANI did not undergo a significant transformation of the surface morphology between those steps in the PFOS experiment (Figure 15a-c).

Among the PFOA and PFOS experiments, the dominant microstructures in MIP-PANI varied. As discussed in the XPS spectra (Figure 13), the N1s binding within PANI was weakened after capturing PFOA and PFOS, in which PFOA-MIP-PANI has the relatively stronger inter-PANI binding strength than that of PFOS-MIP-PANI, suggesting that the PANI chains of PFOA-MIP-PANI might tend to aggregate into spherical structures. On the other hand, because of the weaker inter-PANI binding strength, a continuous structure like an amorphous phase is more favorable than the well-defined spherical structures in PFOA-MIP-PANI. Although SEM contains its theoretical limitation in observing the actual molecularly imprinted cavities, these images provide a morphological point of view to describe the behavior of detaching templates

and recognizing targets for MIPs. Systematic investigation and other supporting information to precisely locate and visualize the realistic cavities are needed in future work.

The detection mechanism of MIP-PANI has been proposed from the obstruction of electric hole transfer caused by the occupation of the recognition sites by the target molecules [12]. The absorption of target molecules can modulate the conductivity of PANI. As shown in Figure 18, polyaniline exists in two types of configurations: emeraldine salt and emeraldine base. Because of the presence of the positive charges as the charge carriers for the electrical conductance through the PANI matrix which is like a p-type semiconductor, emeraldine salt is conductive while emeraldine base is much less so. In the synthesis of PANI, the addition of HCl as the dopant provides the conductance of the PANI by the emeraldine salt. PFOA and PFOS are aliphatic acids that are rich in negative charges and electron lone pairs, which could attract the electron holes on nitrogen atoms of PANI and shift the functional groups from the bulk to the surface during the molecular imprinting polymerization, resulting in a mutually compensated structure of PFOA/PFOS and PANI matrix through the electrostatic interaction. When PFOA or PFOS samples are dispensed on the surface of the PFOA-MIP-PANI or PFOS-MIP-PANI electrodes where the recognition sites are rich in positive charges, the negative charges of PFOA or PFOS might bind with the PANI by neutralizing those electron holes, resulting in a reduction of the number of charge carriers as well as in the conductivity. This also agrees with the increased characteristics of imine groups indicated by the XPS spectra in Figure 13, suggesting that the partial emeraldine salt in the PANI might have been transferred into the less conductive emeraldine base, causing the increased resistance of the calibration curves in Figure 8 and Figure 9. Since the pH value of the PFOS sample solution was close to 7, the exposure of trace PFOA or PFOS in a ppt level might be unable to reveal a visible colorimetric change of the PANI

electrode from green (emeraldine salt) to blue (emeraldine base). Alternatively, the absorption of PFOS is demonstrated in the FTIR and XPS spectra, and the peak shift in XPS indicates more characteristics of imine groups that contribute to the less conductive emeraldine base. Although XPS is not designed for precise quantitative analysis due to lack of calibration standards, and the actual balance of salt form and base form implied by the addition of PFOA or PFOS is yet to be determined, the spectra still provide a comparable and corresponsive proof of PFOA and PFOS detection and a reduction of conductivity.

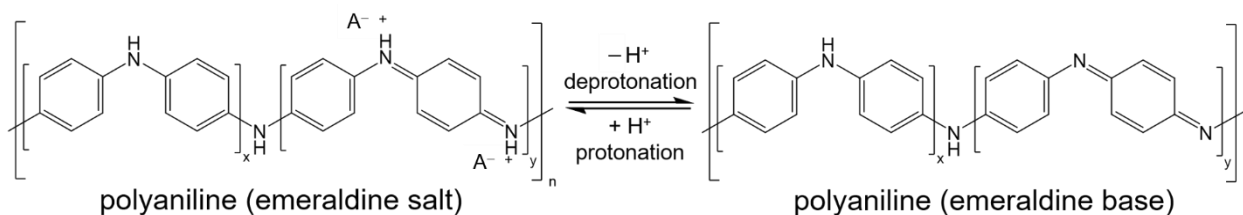


Figure 18 The transformation between the forms of polyaniline emeraldine salt and emeraldine base. The symbol of A- denotes the counter ion of the positively charged electron-hole.

Molecular imprinting technology provides a promising method for fabricating specific binding sites, which benefit from the intermolecular interaction between templates and polymer matrix. Since the approach of detection depends on the intermolecular interaction and structural complementarity, we used relevant PFCs with a different functional group (carboxylic acid or sulfonate group) and varied lengths of aliphatic groups from four to eight carbons (PFBA, PFHxA, and PFOA or PFOS) to evaluate the effectiveness of molecular imprinting for PFOA and PFOS detection. The slightly increased resistivity ratios for the longer PFCs might result

from the more similar geometry to the corresponding target, PFOA or PFOS. Particularly, PFOA and PFOS share a similar chemical structure consisting of eight fully fluorine-substituted carbons and functional groups of carboxylic acid and sulfonate, making these two PFCs more responsive to their analogous hosts of PFOS- and PFOA-MIP-PANI compared with PFBA and PFHxA are. However, the responses for those shorter PFCs or PFCs with different functional groups still have statistical significance to the response of PFOA and PFOS as shown in Figure 16 and Figure 17, respectively. Molecular imprinting of PFOA and PFOS on PANI can fabricate receptor-like structures facilitating the recognition of target molecules; therefore, PFOA-MIP-PANI and PFOS-MIP-PANI demonstrate excellent selectivity to their designated target molecules of PFOA and PFOS among other comparable PFCs.

As discussed before, the 70 ppt of the advisory maximum is what we are interested in. To test if a sample solution exceeds the legal tolerance and is safe to be consumed, this PFC-MIP-PANI is expected to identify the concentration not only in a single-solute solution but also in a mixture of PFOA and PFOS. Therefore, a series of mixed solutions of PFOA and PFOS were dispensed on the PFOA-MIP-PANI and PFOS-MIP-PANI paper sensors. In addition to a single template, this study used a hybrid template consisting of PFOA and PFOS for the first time to test the efficacy of the hybrid imprinting approach and to investigate the sensing mechanism.

According to the calibration curves in Figure 7, the normalized resistivity ratio increased after PFOA and PFOS exposure, and PFOS-MIP-PANI is more responsive to its target molecule, PFOS, than PFOA-MIP-PANI does from the larger slope in the linear region under 100 ppt. Ideally, PFOS-MIP-PANI should have nearly no response to PFOA at any concentrations, so the resistivity ratios should gradually decrease as the PFOS concentration decreases in the mixture. The similar hypothesis also applies to the PFOA system. The response of PFOS-MIP-PANI

should be larger than that of PFOA-MIP-PANI, which is confirmed by Figure 10. PFOS-MIP-PANI was more responsive in those mixtures with higher concentrations of PFOS, and the resistivity ratios were higher than those of PFOA-MIP-PANI; however, some of the concentration sets did not perfectly follow this rule. In the meantime, PFOA-MIP-PANI experienced the larger response in PFOA-rich solutions, then the responses decreased as the concentration of PFOA decreased. Once more, the data did not strictly follow this trend. The structural similarity of PFOA and PFOS might result in a minor competitive effect in the mixtures as discussed in the selectivity experiment.

Moreover, the PFOA/PFOS-MIP-PANI hybrid demonstrates a fluctuation in the responses of resistivity ratios. The two types of templates might compete together with the aniline monomers during polymerization, establishing their specific binding sites coexist in the PANI matrix. Because of the stronger interaction of PFOS and PANI at the concentration lower than 100 ppt, the resulted hybrid might have a tendency slightly toward PFOS, and the resistivity ratios fluctuated up and down until more PFOS was presented in the mixed solutions. Although current data and hypotheses do not perfectly support the trends observed in Figure 10, the detection efficacy in mixed solutions and the effect of hybrid imprinting are still worth further investigations.

CHAPTER III

WIRELESS GAS DETECTION BASED ON MOLECULARLY IMPRINTED POLYANILINE

Introduction

Molecular Imprinting in Gas Sensing

Air pollution has been one of the most serious issues of the world since the last decades and costs many lives annually. The toxic pollutants in outdoor and indoor environments are categorized by a variety of volatile organic compounds (VOCs) like ammonia (NH_3) [87-89], ethanol [89, 90], toluene [91], and methanol [92-94]. These gases are regulated by the Occupational Safety and Health Administration (OSHA), and many operational standards particularly for industrial safety have been released. Taking NH_3 gas as an example, the background level in the atmosphere is below 5 ppb [95], and the maximum exposure tolerance for humans is 25 ppm for 8 h and 35 ppm for 10 min [96]. Inhaling overdose of NH_3 gas may cause acute illnesses to eyes, skin, and lungs. As a result, a sensitive and accurate assay for detecting these VOCs is in high demand.

Conventional methods for detecting gases rely on gas chromatography/mass spectroscopy which is expensive and complicated in sampling procedures. Portable gas sensors with high sensitivity and a low-cost are commercially available, however, the disadvantages include selectivity and limited types of target gases. According to the principle of molecular imprinting, this approach offers the potential in synthesizing gas-imprinted polymers with a low-cost, high sensitivity, and good selectivity for detecting VOCs [94]. Many gas sensors based on MIPs have been reported for detecting multiple VOCs like ammonia [97], toluene/xylene [91], formaldehyde [98, 99], and acetonitrile [100]. Another example for ethanol detection by quasi-

molecularly imprinted SnO₂ nanoparticles was also suggested by Tan et al [101]. Compared with the molecular imprinting process with target analytes in liquid solutions, the template removal process for gas imprinting could be even easier by simply letting the VOCs evaporated on the MIP surface through heating or vacuum drying [91]. Although MIP gas sensors might have a longer response and recovery time, molecular imprinting gas sensors still possess a good sensitivity and stability [92].

Wireless Radio-frequency Identification Sensors

Wireless chemical sensors are electronic paired devices that retrieve the signal variation upon the exposure to chemicals at one side and transmit signals to another side for analysis as schemed in Figure 19 [102]. Numerous wireless and contactless protocols are available for chemical sensing nowadays such as Bluetooth, ZigBee, radio-frequency identification (RFID), near-field communication (NFC), and short-range device (ISM/SRD860). The features of each communication protocol are summarized in Table 6 [102-112]. Among these technologies, RFID as one of the common communication protocols has been widely used in sensor applications [102, 113]. The advantages of RFID include but would not limit to battery-free antennas, simple installation, low-cost, medium transmitting ranges available for both contactless and short-range communication, and smartphone capability [102, 114-117]. Particularly, RFID antennas can collect and transfer chemical data through nontransparent and sealed packaging, which is an outstanding advantage over other optical sensors [114]. For such logistic tracking or quality control of food packages, the ultra-high frequency (UHF) band is currently in practical use by ISO 18000-6 and EPC GEN2 Standards [103]. The battery-free RFID antennas are powered by the antenna reader while measurement, enabling the antennas to be attached in the food packages

without external power supplies. Therefore, RFID sensors are excellent candidates for gas sensing and monitoring, especially for those sealed and air-tight packages of which gas sampling is unrealistic [114, 118, 119].

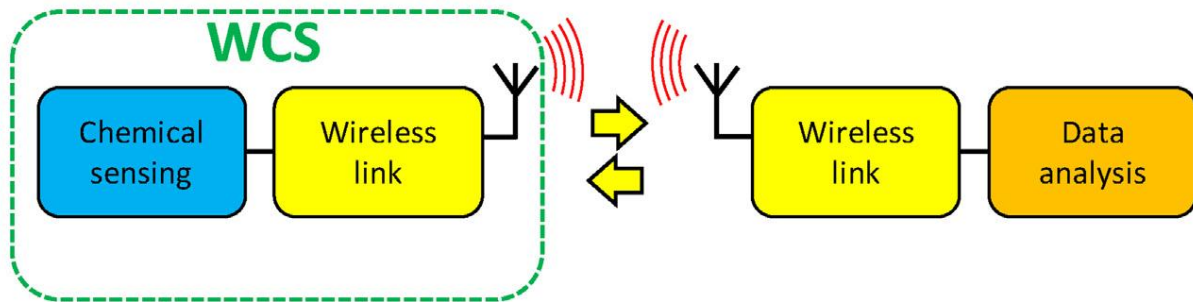


Figure 19 The scheme of the concept of wireless chemical sensors (WCS). Reprinted from [102].

Table 6 The features of common wireless communication protocols for chemical sensing. Adapted from [102-112]. LF: low frequency; HF: high frequency; UHF: ultra-high frequency

Protocol	Mode	Power	Radio Band	Data Rate	Range
Bluetooth	Active	Battery	2.4 GHz	1 Mbps	10–100 m
ZigBee	Active	Battery	868 MHz, 915 MHz, 2.4 GHz	24 Mbps, < 250 kbps	10–100 m
RFID	Passive	Battery or Battery-free	LF: < 135 kHz; HF: 13.56 MHz; UHF: 860–960 MHz	< 100 kbps	< 15 m, depending on frequencies
NFC	Passive	Battery or Battery-free	13.56 MHz	< 424 kbps	< 5 cm
SRD	Active	Battery	433 MHz, 863–870 MHz	< 200 kbps	50 m–2 km
Protocol	Features				
Bluetooth	Massive and real-time data transfer, good indoor range, smartphone available				
ZigBee	Very low power, good indoor range, good network capability				
RFID	Ultra-low power, battery-free, short-range, limited data transfer, e-labeling, and smartphone available for HF band				
NFC	Ultra-low power, very short range for contactless only, smartphone available				
SRD	Very low power, good range but low data rate, good local network				

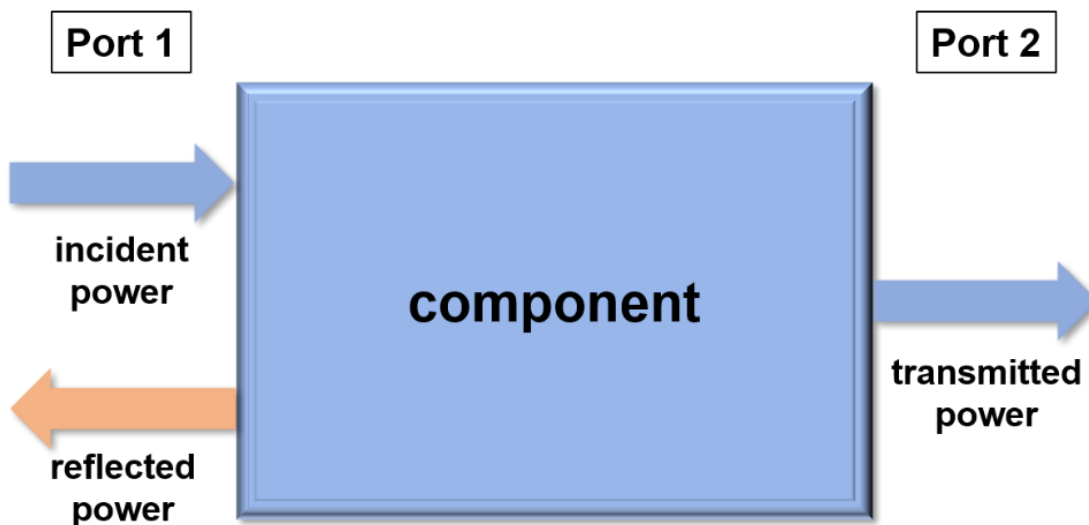
In principle, the relationship between the input-output ports is defined as S-parameter, S_{xy} , in an electronic component. The x and y represent the two ports of the component, and the

sequence of “xy” means the transmitting direction from Port x to Port y. S_{xy} represents the power ratio of the wave delivered from Port x to Port y [120, 121]. The schematic diagram and definition of the S-parameter are demonstrated in Figure 20. Practically speaking, S_{11} is the most widely utilized S-parameter in evaluating how much power or energy is reflected by the antenna tag. For its correlation with impedance, the S_{11} as a function of impedance can be written as [118]:

$$S_{11} = \log \Gamma = \log\left(\frac{Z_L - Z_0}{Z_L + Z_0}\right)$$

Equation 4

where Γ is the reflection coefficient calculated by the complex impedance of the load of the antenna tag (Z_L) and the reference which is the antenna reader (Z_0). The larger the absolute value of S_{11} is, the more reflected power is lost by being absorbed by the antenna; therefore, the reflection coefficient Γ is sometimes identified as return loss [122]. By the principle of the logarithm, the reflection coefficient is always equal or less than one, and S_{11} is either zero or always negative. As the impedance of the antenna tag increases, the reflection coefficient increases, then the S_{11} parameter increases with the decreased absolute value closer to zero. Note that the impedance of the tag can never be lower than the impedance of the reader, otherwise, the log-equation would be invalid due to the negative variable.



S_{xy} : the ratio of reflected wave to at port x to the incident wave at port y

Figure 20 The schematic illustration of the definition of the S-parameter.

Materials and Methods

Materials

For the gas templates in the synthesis of gas imprinted PANI, ammonium hydroxide solution (ACS reagent, 28.0–30.0%) was purchased from Sigma-Aldrich (St. Louis, MO, USA), and Koptec 190 Proof ethanol (95%) was purchased from DeconLabs (King of Prussia, PA, USA). The polyester film as the printed antenna substrate was obtained from Xerox (Norwalk, CT, USA). The curable silver ink for printing the antenna was purchased from NovaCentrix (JS ADEV 291, Round Rock, TX, USA).

Synthesis of Ammonia and Ethanol Imprinted PANI

To synthesize ammonia molecularly imprinted PANI (NH₃-MIP-PANI), the template in the monomer solution as the previous synthetic protocol in Chapter II was replaced with 70 μ l of the ammonium hydroxide solution, followed by adjusting the total volume of the monomer solution to 5 ml by adding DI water. NH₃-MIP-PANI was then synthesized on paper strips by following the same protocol. The resulted NH₃-MIP-PANI paper strips were air-dried without sonication to let the NH₃ templates evaporated from the surface. For making ethanol molecularly imprinted PANI (EtOH-MIP-PANI), 62.7 μ l of 95% ethanol as the template was added to the aniline monomer solution, followed by the same procedures and the template removal process for NH₃-MIP-PANI. The molar ratio of the monomer to the template was 1:1.

Gas Detection by Resistance Measurement

The NH₃-MIP-PANI or EtOH-MIP-PANI paper strips were integrated with copper connecting electrodes and silver paste on a stencil substrate as previously mentioned. Subsequently, two electric wires were soldered on the copper electrodes to connect the multimeter and the sensor in the sealed gas test chamber as shown in Figure 21a.

The VOCs of NH₃ or ethanol gases were introduced into the test chamber by dispensing a certain amount of VOC liquid on a small disk in the chamber, and the concentration of the fully vaporized gas can be calculated by the following equation:

$$\frac{\left(\frac{V \times d \times c}{M}\right)}{\left(\frac{V_t}{24.45}\right)} = \frac{n_g}{n_t} = \text{ppm}$$

Equation 5

V is the volume of the dispensed liquid. d is the density of the liquid. c is the concentration of the liquid. M is the molecular weight of the chemical. V_t is the total volume of the test chamber calculated by the dimensions in Figure 21b. The value of 24.45 is the volume in liters of one mole of air molecules from the ideal gas law. The ratio of n_g to n_t represents the ratio of the number of VOC gas molecules to the number of total gas molecules in the test chamber; therefore, the concentration of VOC gas in the chamber can be calculated. Once the VOC sample was dispensed and the chamber was sealed, the real-time DC resistance of the MIP-PANI electrodes was measured at each incremental time, followed by opening the chamber for recovery, and further increasing the gas concentration on the same device. Besides, for the experiment detecting ethanol saturated vapor, an excess amount of ethanol solution was added into an opened petri dish and stood for 1 h in the test chamber before inserting the sensor.

Several parameters like t_{90} , t_{10} , and S for evaluating the kinetic response of the electrodes to the gas. t_{90} represents the response time needed to reach 90% of the total response, and t_{10} means the recovery time needed to relax back to 10% of the baseline from the peak value [123]. The parameter of S is the sensitivity of the sensor, defined as [124, 125]:

$$S (\text{sensitivity}) = \frac{\Delta R}{R_0} = \frac{R_g - R_0}{R_0}$$

Equation 6

where R_0 and R_g represent the resistances of the MIP-PANI electrodes before and after exposure to VOC gases, respectively.

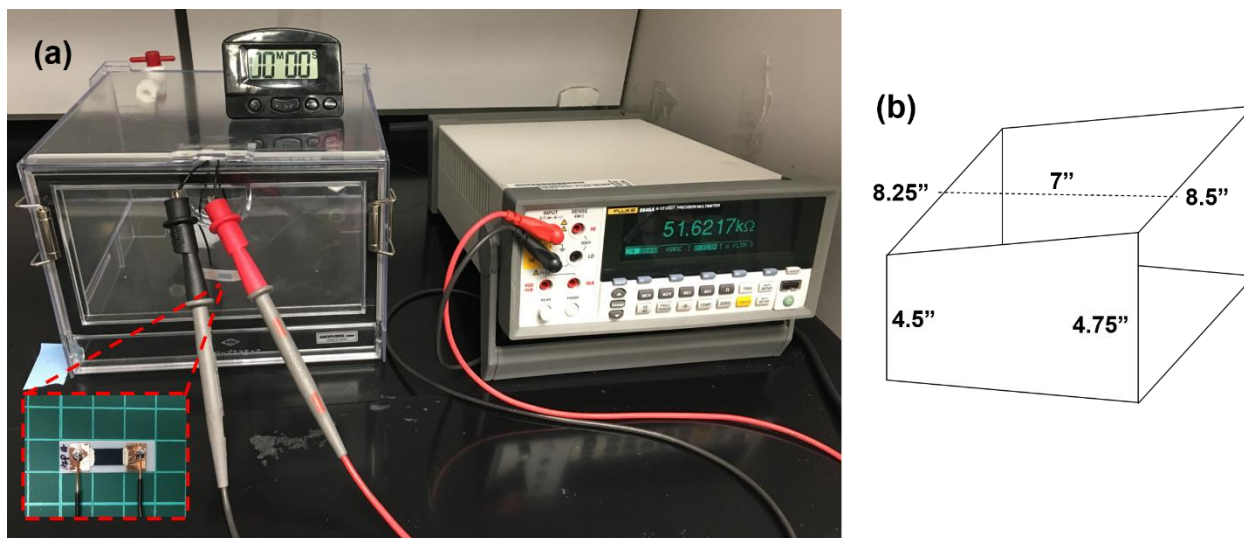


Figure 21 (a) The photographic image of the experimental setting of DC resistance measurement for gas sensing. The pop-out figure presents the sensor integrated with two electric wires for connecting the probes with the sensor in the sealed test chamber. (b) The scheme of the gas test chamber with its dimensional information for calculating the total volume.

Fabrication of Antenna and Deposition of MIP-PANI

The antenna was printed on a polyester film by inkjet printing using the Dimatix Material Printer 2830 (DMP-2830, Fujifilm Dimatix, Santa Clara, CA, USA) with silver conductive ink. The detailed operating parameters can be found in the appendix from the previous publication [12]. After the antenna was printed, the silver ink was cured at 110°C for 1 h to achieve optimal conductivity. The polymer solution of NH₃-MIP-PANI or EtOH-MIP-PANI was prepared by the procedures above, and 1 μl of the solution was deposited on the opened space on the middle of the antenna as shown in Figure 22, followed by being air-dried overnight at 25°C.

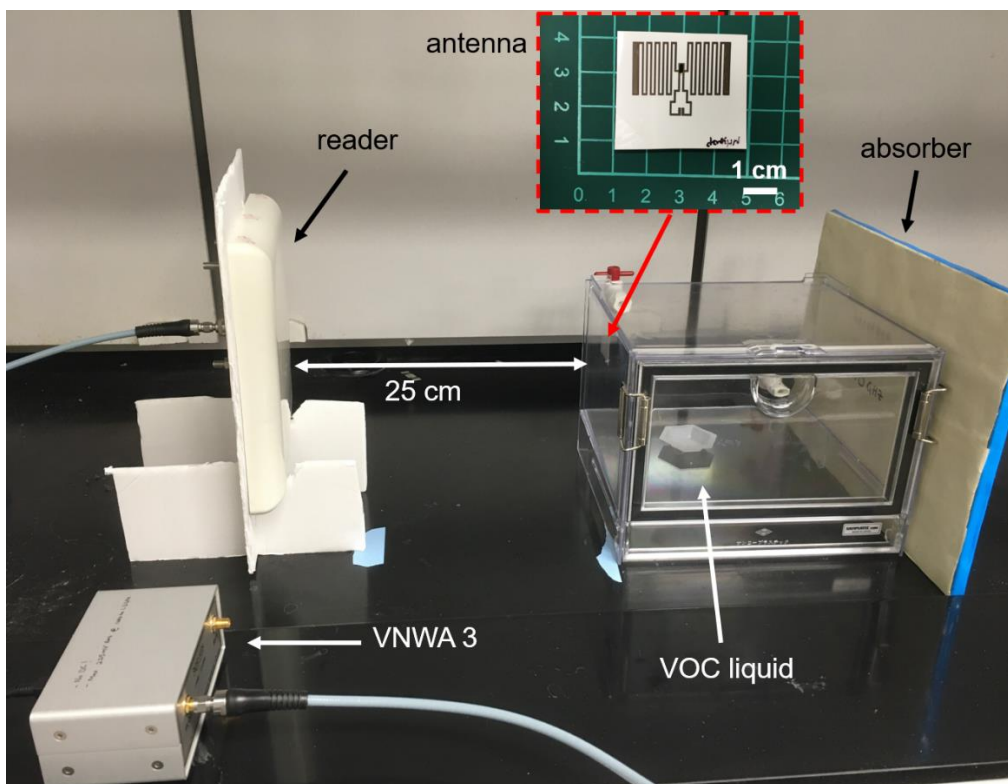


Figure 22 The instrumental setup of the wireless sensing experiment. The inserted picture displays the inkjet-printed antenna on a flexible substrate of a polyester film. Note that the excess wires connecting the reader and the vector network analyzer (VNA) were hindered in this figure.

Gas Detection by Wireless Method

The experimental setup (Figure 22) of the wireless sensing consists of four major components: a vector network analyzer (VNA, DG8SAQ VNWA 3, SDR-Kits, United Kingdom), an antenna reader (MT-242025, MTI Wireless Edge, Israel), the printed antenna in the gas test chamber, and an absorber (AB7050HF, 3M, Saint Paul, MN, USA) at the end. The VNA served as the signal analyzer as well as the power supply for the antenna reader. The rear end of the VNA is connected to a laptop for the controlling purpose. Signal pulses were generated by the VNA, partially reflected by the antenna, and read by the antenna reader. The

absorber was to reduce the environmental interference from the reflection beyond the test chamber which might be induced by metal pieces or walls. The distance between the antenna and the reader was fixed at 25 cm, and all the accessories were fixed at their initial positions during the entire experiment. Unnecessary stuff should be cleared from the chemical hood where the experiment would be executed, especially metal parts.

Figure 23 shows a sample interface of the VNA operating software which directs the signal pulses and analyzes the signal returns. Calibration should be carefully done before each experiment because the signal responses are sensitive to the experimental setup. The detailed calibration procedures of the VNA are demonstrated in Appendix A. The 1,000 data points in total were collected in a single signal sweep at a range from 700 to 1,200 MHz of a scan rate of 100 msec/point. To acquire the wireless signal, after 10 min from the time that the VOC sample was dispensed into the test chamber, a single sweep was initiated by the VNA and the S_{11} responses as a function of frequency were automatically recorded. When finishing the data collection, the chamber was opened and left for 10 min to release the gas. A higher concentration of VOC sample liquid was then added into the chamber, and the same procedure was repeated.

For data processing of the wireless signals, the original signal response presented as the reduced reflection coefficient ($S_{11, \text{sample}}$) was subtracted by the response of the blank antenna without the deposition of MIP-PANI ($S_{11, \text{blank}}$) to obtain the change in reduced reflection coefficient (ΔS_{11}) as illustrated by Equation 7.

$$\Delta S_{11} = S_{11, \text{sample}} - S_{11, \text{blank}}$$

Equation 7

In other words, the processed signals should merely reveal the response from the MIP-PANI and the exposure of VOCs. At least three multiple sweeps were used to calculate the standard deviations and the limit of detection.

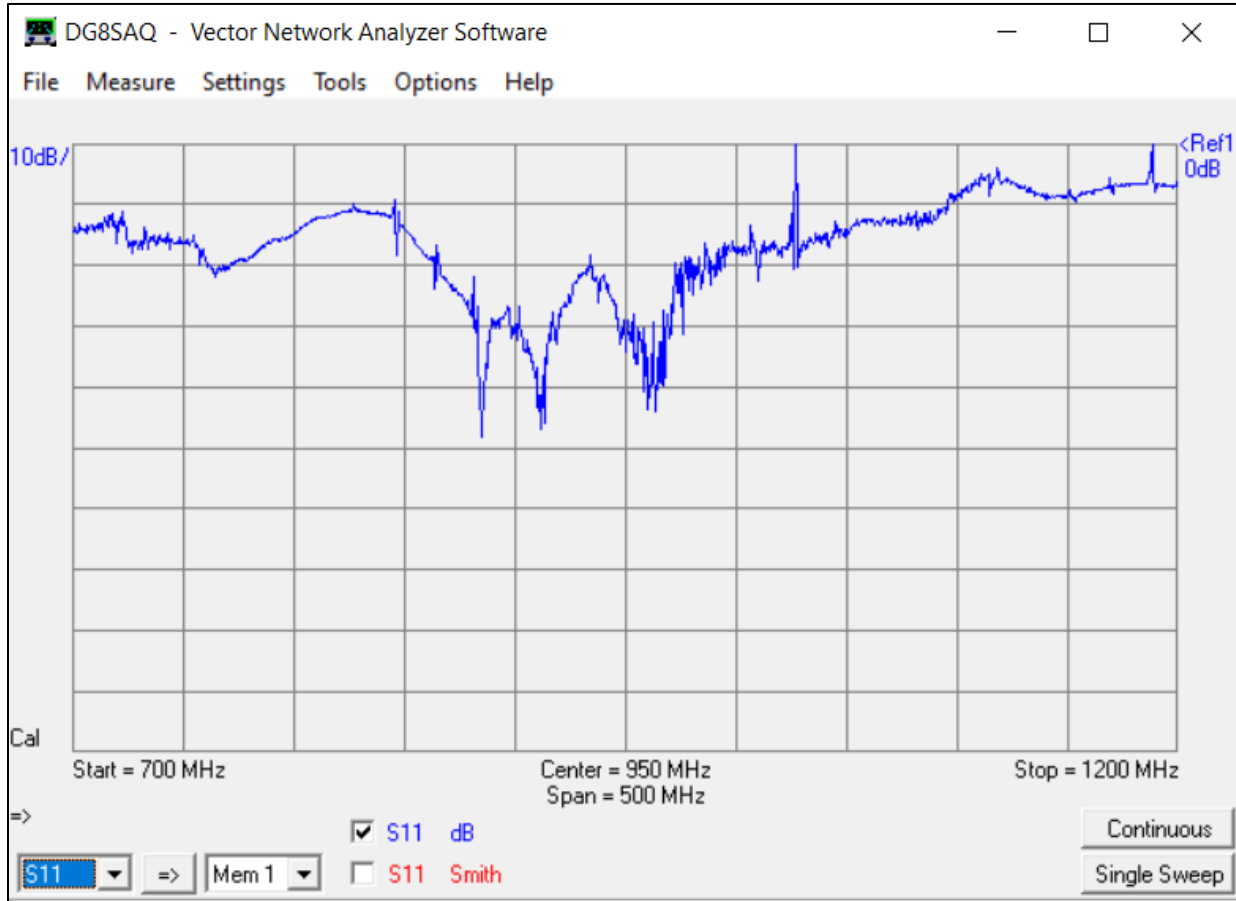


Figure 23 The screenshot of the VNA software including the frequency range and the y axis of the S₁₁ parameter with the unit of decibels.

Results

Gas Sensing by DC Resistance Measurement

The results of real-time measurement of DC resistances of NH₃-MIP-PANI and EtOH-MIP-PANI electrodes in NH₃ and ethanol gases are shown in Figure 24. The NIP-PANI served as the control for each experiment. For NH₃ detection in Figure 24a, NH₃-MIP-PANI was more responsive to NH₃ gas and quickly reached saturation after 10 to 15 min, while NIP-PANI needed more than 20 min to reach saturation. The total response of NH₃-MIP-PANI was also larger than that of NIP-PANI. At 35 min, the chamber was opened, and the resistance dropped. The two electrodes both exhibit the recovery behavior; however, none of the resistances decreased to the baselines after 25 min of recovery. The recovery also reached saturation, and it is unlikely the resistance would keep decreasing afterward. Meanwhile, for ethanol detection, both responses of EtOH-MIP-PANI and NIP-PANI reached saturation after 9 min, and the profiles show that the recovery ability was better than the recovery in NH₃ detection. NIP-PANI was less responsive than EtOH-MIP-PANI due to the lower resistance change from the beginning to the ultimate point before opening the chamber.

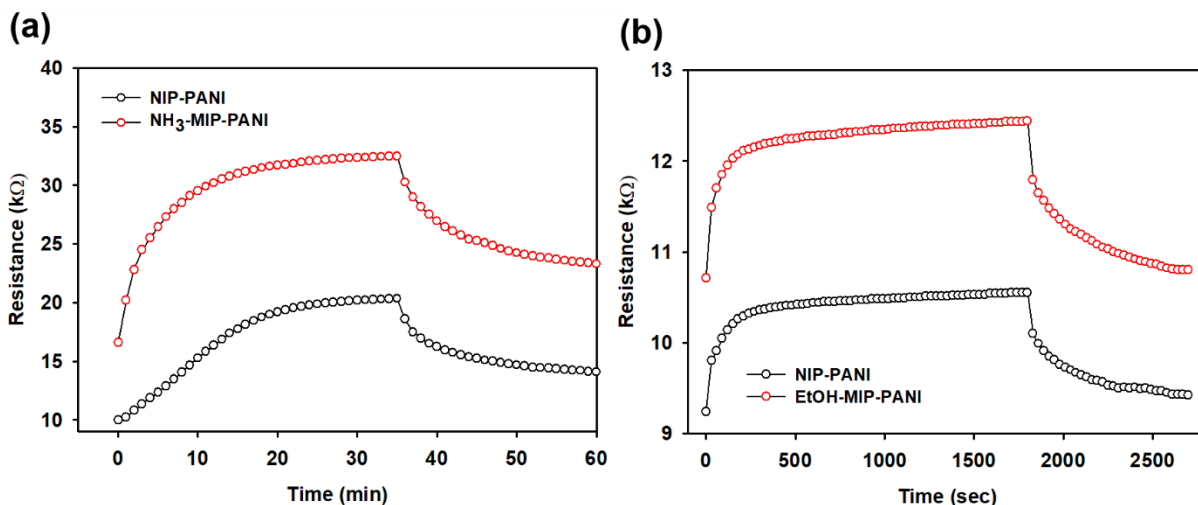


Figure 24 The real-time DC resistances of (a) NIP-PANI and NH₃-MIP-PANI electrodes after exposure to 100 ppm NH₃ gas (b) NIP-PANI and EtOH-MIP-PANI electrodes after exposure to saturated ethanol vapor (concentration ~ 58,684 ppm).

According to the response data in Figure 24, a few parameters for evaluating the real-time response are summarized in Table 7. NH₃-MIP-PANI had a faster response time of 15 min than NIP-PANI did of 21 min. Both values of recovery time t_{10} are not available in NH₃ detection. Moreover, the sensitivity of NH₃-MIP-PANI at 15 min is better than that of NIP-PANI as calculated by using Equation 6. In addition, for ethanol detection, EtOH-MIP-PANI and NIP-PANI have similar response time of 9 min; however, the response of NIP-PANI never recovered to the time of t_{10} . The recovery time of EtOH-MIP-PANI was 11 min. The sensitivity of EtOH-MIP-PANI is a little bit better than that of NIP-PANI by a minute difference of 0.02.

Table 7 The summary of parameters for evaluating the response of the molecularly imprinted gas sensors for NH₃ and ethanol detection. n/a: data not available

NH₃ Detection		
Parameters	NIP	MIP
t₉₀	21 min	15 min
t₁₀	n/a	n/a
R_{g, 15 min}/R₀	1.78	1.87
S_{15 min}	0.78	0.87
Ethanol Detection		
Parameter	NIP	MIP
t₉₀	9 min	9 min
t₁₀	n/a	11 min
R_g/R₀	1.142	1.162
S	0.142	0.162

The real-time results of NH₃ and ethanol detection with more detailed concentrations are shown in Figure 25. Again, NH₃-MIP-PANI was unable to sufficiently recover after each exposure to NH₃; therefore, the baseline gradually increased as the concentration of NH₃ increased. The peak values right before the recovery step are used to construct the calibration curve of the linear regression equation of $y = 0.1225 + 25.872x$ and the R² value of 0.992. The linear range was from 25 to 100 ppm. Meanwhile, EtOH-MIP-PANI expresses the better recovery capability, leading the baseline increase only to exist at the higher concentrations. The

peak values also increased as the concentrations of ethanol increased, resulting in the calibration curve with the linear regression equation of $y = 0.0001x + 21.7189$ and the R^2 value of 0.9757. The calibration curve has reached saturation from 5,000 ppm to 10,000 ppm. The linear region was not prominent according to the few data points and the smaller coefficient of determination.

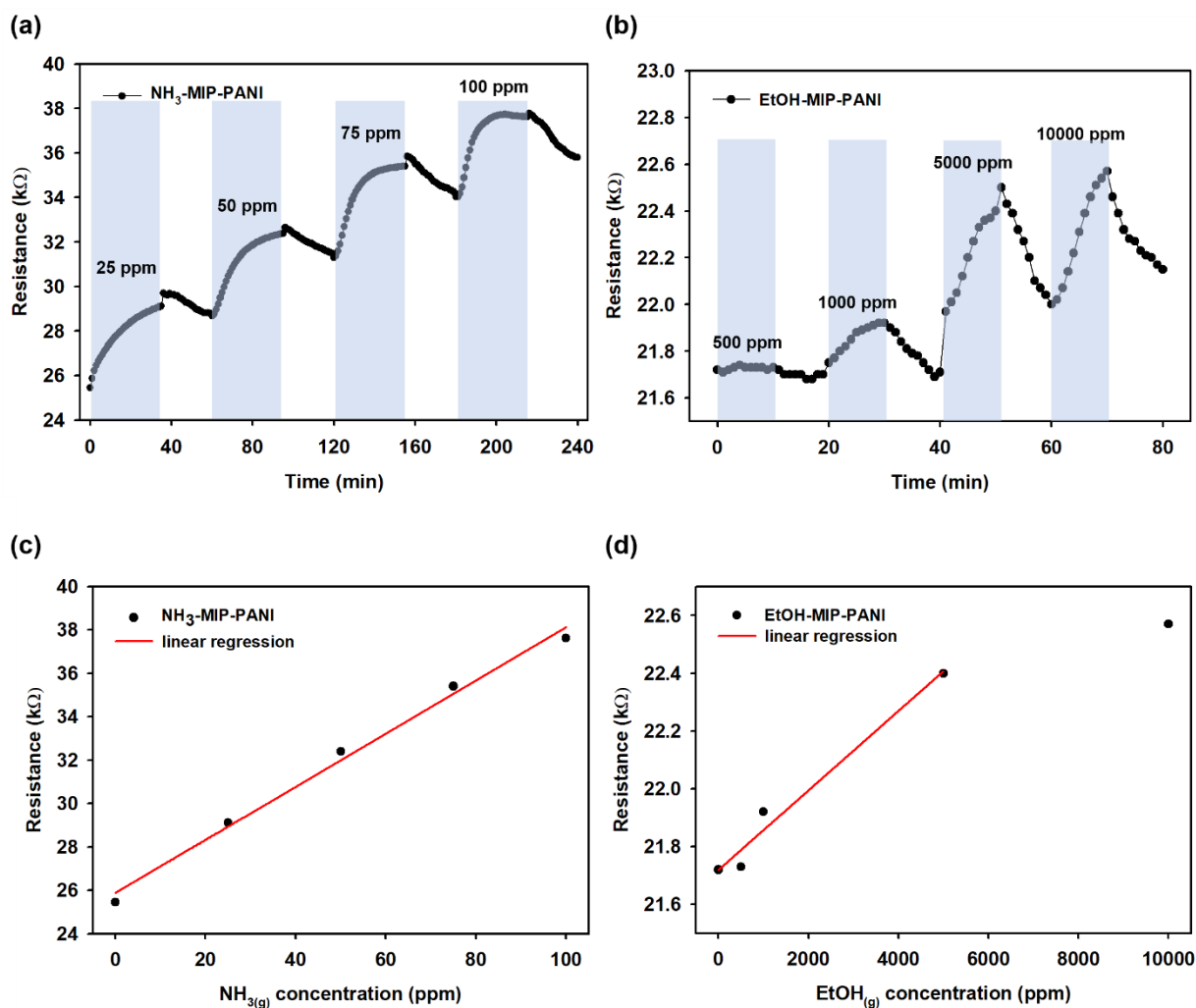


Figure 25 The real-time resistance responses and the corresponding linear regression curves as a function of VOC gas concentration. (a, c) NH₃ detection using the NH₃-MIP-PANI electrode. After exposure to NH₃ gas for 35 min, the test chamber was opened for 25 min for recovery, followed by injecting the higher concentration of NH₃. (b, d) Ethanol

detection by using the EtOH-MIP-PANI electrode. The exposure and recovery time was 10 min. The data points in the calibration curves were obtained from the peak values in the real-time responses.

Wireless Gas Sensing

The wireless sensing profiles of NH_3 gas detection and the calibration curve are shown in Figure 26. Although the figure demonstrates multiple noisy profiles, certain trends in NH_3 concentrations can still be observed at some of the frequencies such as 982 MHz. The difference in S_{11} as a function of NH_3 concentrations was analyzed in Figure 26b, giving the linear regression equation of $y = 0.0812x + 0.9227$ with the linear range from 25 to 100 ppm of NH_3 and the R^2 value of 0.978. For all the partial wireless data in this section, their full-spectrum data of the wireless sensing can be found in Appendix B.

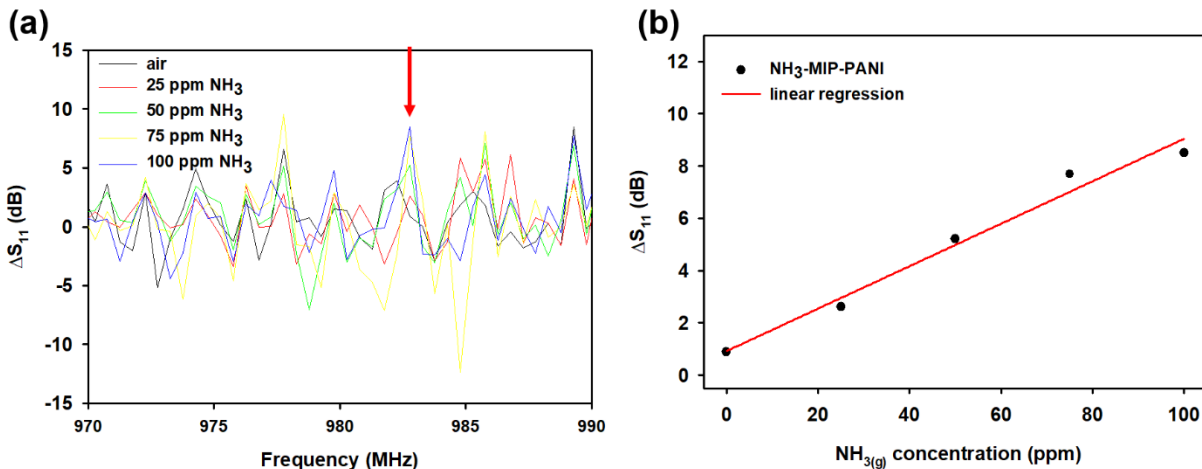


Figure 26 (a) The wireless response of ΔS_{11} of the printed antenna with NH_3 -MIP-PANI upon exposure to NH_3 gas. The red arrow points out the peak at 982 MHz (b) The

calibration curve calculated from the ΔS_{11} values at 982 MHz by using a linear regression model.

For ethanol gas detection, the wireless data in a selected range is demonstrated in Figure 27a. Profiles including few peaks with trends in NH_3 concentrations also present in the data, from which the peak at around 949 MHz was selected to build the calibration curve as shown in Figure 27b. The calibration curve has a linear range from 500 to 10,000 ppm of ethanol concentrations and a linear regression equation of $y = 0.001x + 0.4914$. The coefficient of determination of the calibration curve is 0.9849.

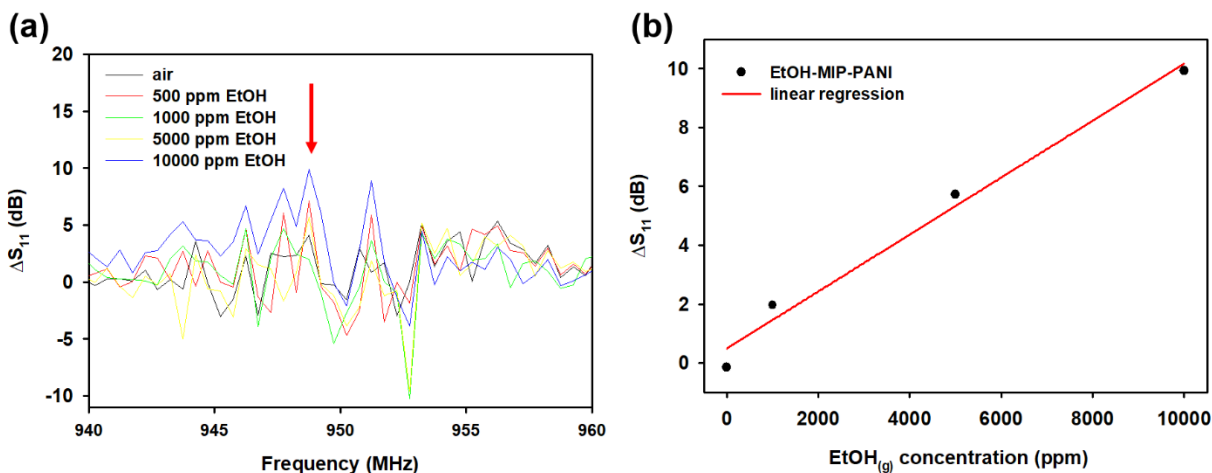


Figure 27 (a) The ΔS_{11} -frequency data of ethanol gas detection. The red arrow indicates the peak being analyzed by linear regression. (b) The calibration curve of ΔS_{11} as a function of ethanol concentration at 949 MHz.

For the NH₃ at lower concentrations of the ppb level, an additional experiment of wireless sensing was performed, and the results can be found in Figure 28. In Figure 28a, the signals from 0 to 10 ppm seem to have an increasing trend in the plateau region from 905 to 920 MHz indicated by the red arrow. Although some of the concentrations might be exceptions from this trend, the overall tendency of increasing ΔS_{11} can be found. A certain peak with the large ΔS_{11} response and a trend in concentrations is identified in Figure 28b at the frequency of 974 MHz. The corresponding calibration curve is demonstrated in Figure 29 with a linear regression region ranges from 500 ppb to 2.5 ppm, followed by a saturation beyond 5 ppm. The fitted curve has the linear equation of $y = 2.3455x + 0.0032$, and the value of R^2 is 0.98.

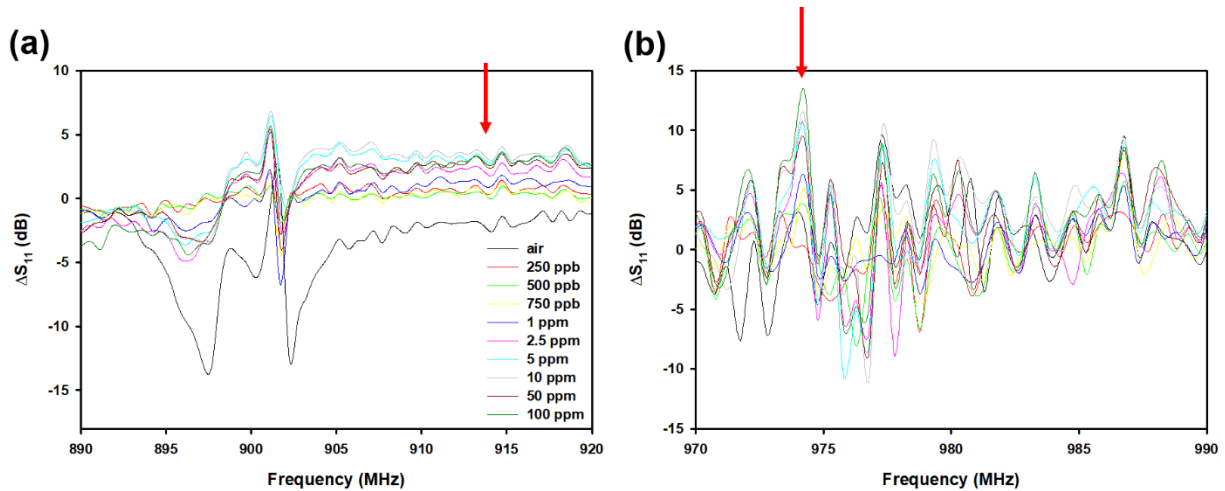


Figure 28 The ΔS_{11} -frequency data of NH₃ gas detection at the range of (a) 890 to 920 MHz (b) 970 to 990 MHz. The two figures share the same figure caption as shown in part (a). Arrows indicate the region and peak of interest with a correlation of ΔS_{11} with the concentration of NH₃ gas.

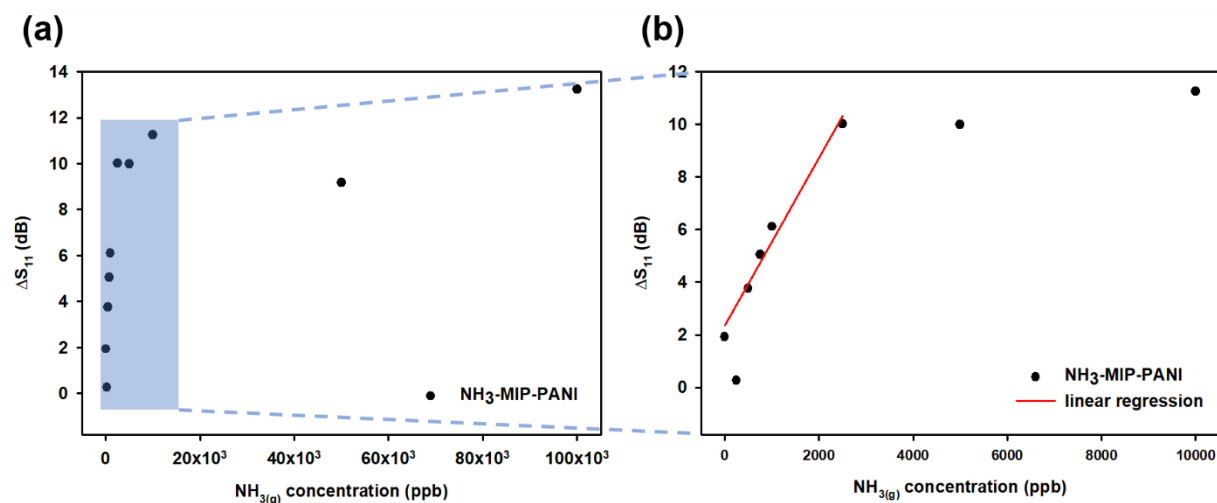


Figure 29 The calibration curves at 974 MHz calculated from the wireless data as shown in Figure 28b. (a) The full set of the data points from 0 to 100 ppm of NH_3 gas. (b) the calibration curve plotted by the partial wireless data from 0 to 10 ppm (10,000 ppb) as the blue shade in part a. The red line denotes the linear regression line from 0 to 2.5 ppm.

Another experiment to investigate the calibration curve was performed, and the average profiles from three repeating wireless measurements of each concentration are shown in Figure 30. Figure 30b and Figure 30c are the enlarged figures showing the peak of interests at 882.7 MHz where the correlation between ΔS_{11} and NH_3 concentration can be found. The calibration curve of ΔS_{11} response as a function of NH_3 concentration is shown in Figure 31. The linear regression equation of the curve in Figure 31c is $y = 0.0013x + 15.0143$ with the R_2 value of 0.9468. The calibration curve reaches a saturation beyond 2.5 ppm. The linear range is from 250 ppb to 1 ppm. From the standard deviation of the blank sample (NH_3 -MIP-PANI exposed to ambient air) and the slope of the linear regression line, the limit of detection for NH_3 gas is estimated to be 122 ppb by using Equation 3.

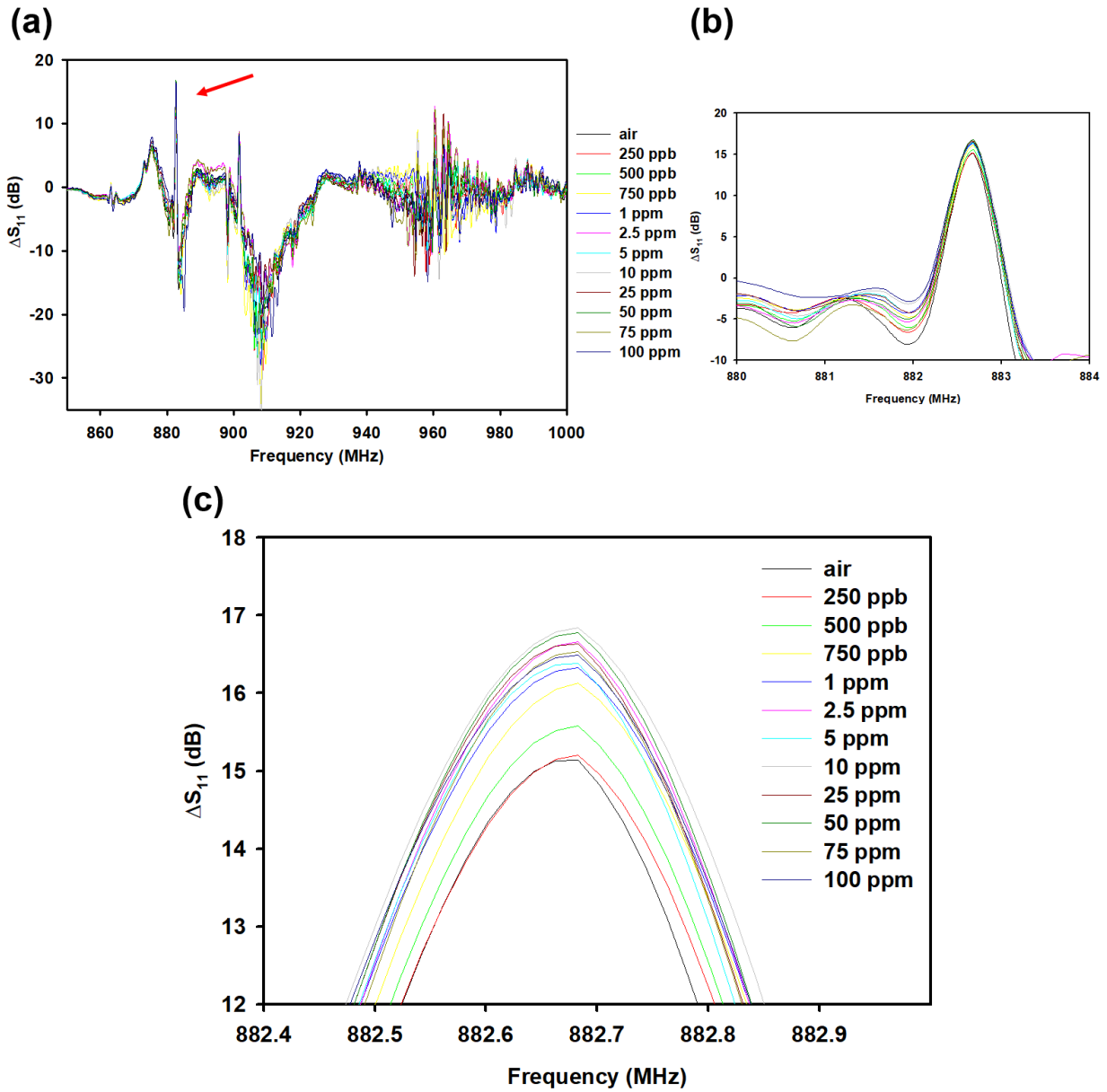


Figure 30 The ΔS_{11} -frequency diagrams of NH_3 gas detection. (a) The diagram from 870 to 1,000 MHz with a red arrow suggesting the characteristic peak being analyzed. (b, c) The enlarged figures of different magnification from part a. The peak locates at around 882.7 MHz. All the figures use the same notation of NH_3 concentrations with different colors of the profiles.

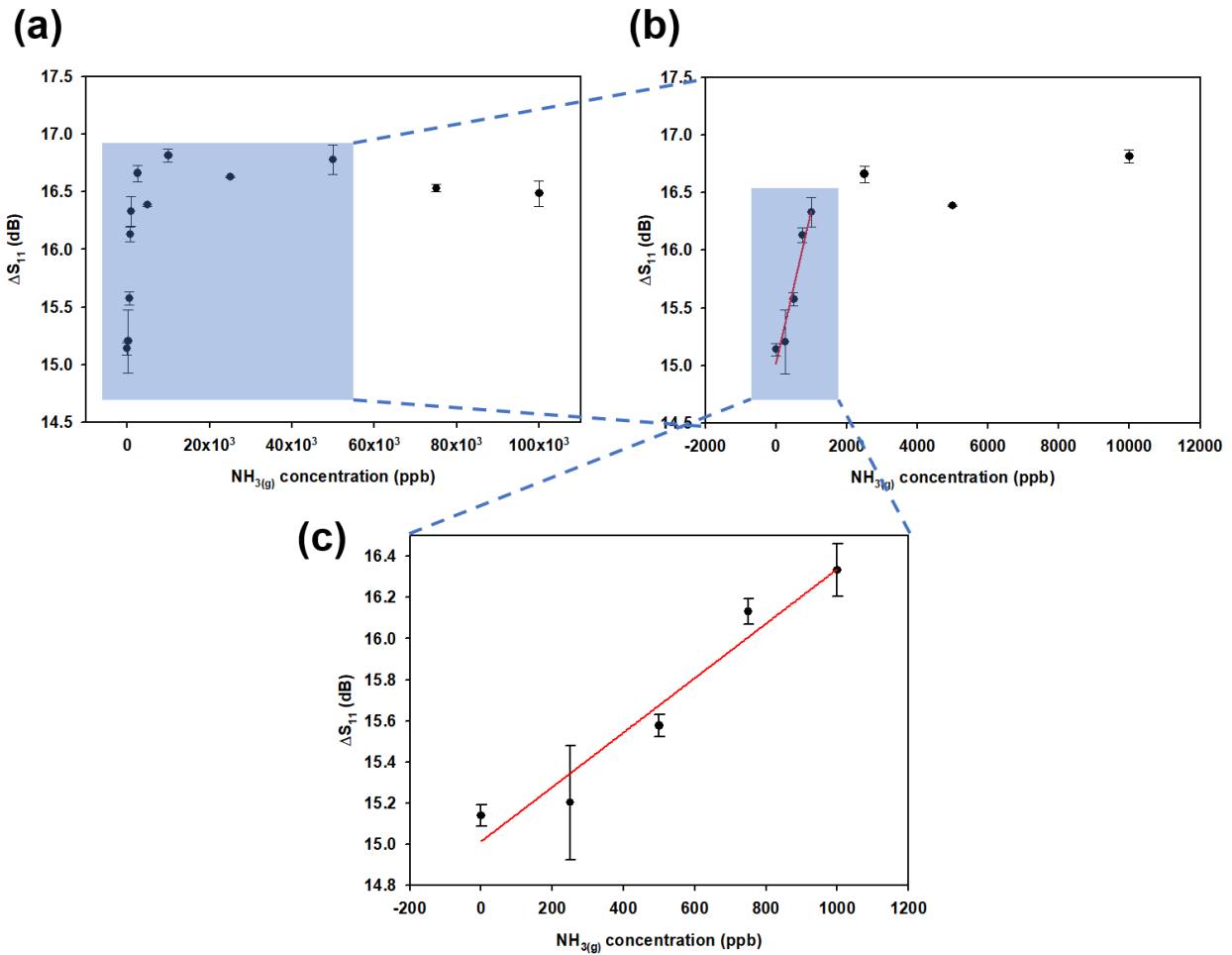


Figure 31 (a) The calibration curve calculated from Figure 30c. (b) The calibration curve plotted by selecting the partial data from 0 to 10 ppm. (c) The partial calibration curve selected by the range of 0 to 1,000 ppb (1 ppm). The standard errors were collected from at least three repeating sweeps provided by the VNA.

Discussion

Passive wireless sensing using RFID provides a promising way to detect and monitor environmental gases on a large scale. Antenna tags can be placed in the locations of interest to collect more comprehensive data from multiple sites and monitor the in-situ concentration by wireless sensing. Wireless sensing is also critical in monitoring the substances in sealed packages

because sampling of the internal gas is not feasible. The antenna tag we developed does not need a battery to operate, and the power to drive the battery-free antenna comes from an external power supply of the VNA. The antenna can be placed in a sealed package, just as we put the antenna in the test chamber. By analyzing the signal gain/loss between the antenna tag and the antenna reader, the reduced reflection coefficient, S_{11} , correlating with the gas concentration can be analyzed to build the calibration curve and identify the linear detecting range as well as the limit of detection.

MIPs have been demonstrated to be excellent sensing elements for fabricating chemical sensors. To promote the potentials of environmental sensing in different ways, the second part of this dissertation study focuses on wireless sensing using MIPs. This platform of MIP-PANI was then firstly evaluated by the same method of DC resistance measurement to validate the efficacy in detecting VOCs like NH_3 or ethanol. Rather than being contacted with the sample solution in PFOA/PFOS experiments, the paper sensor was exposed to the target gas distributed in the entire test chamber in gas experiments. Also, most realistic situations are open systems where gases can flow freely in a certain space and cause localized concentrations. On the other hand, the homogeneity of dissolved analytes in a sample solution usually has not much spatial variation and fluidity as a gas phase. Therefore, the measurement of dynamic response and recovery time is crucial. According to the results in Figure 24 and Table 1, MIP-PANI has the better response time and sensitivity to its target gases of NH_3 and ethanol, suggesting that this molecular imprinting platform is also applicable to gaseous analytes by using liquid templates. Because the dynamic response of NH_3 -MIP-PANI is significantly faster than that of NIP-PANI, the responses at the time of 15 min were used to calculate the sensitivity. The limited recovery ability in NH_3 detection might result from the irreversible absorption of NH_3 molecules on the PANI, in which

NH₃ acted as a dopant and changed the doping level of PANI. On the other hand, for ethanol detection, since ethanol cannot serve as a dopant to PANI, the absorption of ethanol on the surface of PANI was reversible, making the recovery time measurable in the dynamic response profile. Despite the results that both the control and NH₃-MIP-PANI never recovered to the baseline, the recovery ability of NH₃-MIP-PANI was still better.

The better linear regression of NH₃-MIP-PANI compared with EtOH-MIP-PANI might be benefited from the better affinity of NH₃ gas and PANI due to the doping ability as discussed above. Even the testing concentrations of ethanol were much higher than that of NH₃, the calibration curve of EtOH-MIP-PANI was not very promising, indicating that the molecular imprinting process for ethanol imprinting needs to be further improved in the future. For the wireless sensing of ethanol, the R₂ value and the linear range were a bit larger than which in the wired sensing, suggesting the wireless setup might be better for ethanol sensing using EtOH-MIP-PANI. Nevertheless, the lack of specific intermolecular interaction between ethanol and PANI molecules makes molecular imprinting not very effective in this case. Incorporating with other responsive aptamers may be the option to improve the ethanol-imprinting strategy.

For NH₃ wireless sensing, through multiple measurements among concentrations from 250 ppb to 100 ppm, the characteristic peaks with trends of concentrations were identified at around 970 to 980 MHz and around 883 MHz. According to Figure 34 in Appendix A, NH₃-MIP-PANI contributes to the signal variation at around 900 MHz and from 950 to 1,000 MHz, which means that the two regions should be the characteristic signals of interest for MIP-PANI electrodes. In other words, for wireless sensing, one should focus on the peaks and trends around these frequencies and calculate the calibration curves. Because the wireless signals are easy to be affected by many environmental parameters and experimental setups like the presence of metal

parts and liquids in front of the antenna reader. The relative positions of the antenna tag and each accessory also influence the signal response [126]. The surrounding materials and air media may either absorb or reflect the signal, causing the change of signal response and different S_{11} . It is difficult to exclude all the interference among each experiment, so the characteristic peak with trends may happen at the different frequencies with minor shifts. However, the reactive frequencies should remain identical in general. Of course, more experiments and data are needed to acquire a more detailed picture of the wireless profiles with specific peaks and frequencies. The reproducibility of wireless sensing is yet to be further improved. Replacing by a more powerful power supply and VNA might also be helpful with improving the stability and signal-to-noise ratios.

The group of profiles from 905 to 920 MHz also presented a trend of NH_3 concentrations from 250 ppb to 10 ppm, but the variation was not significant. The plateau-like region may serve as another characteristic information of PANI since Figure 34 also shows similar profiles. Together with the two characteristic regions as previously discussed, these flat lines might be the third informational region, but it only includes limited information of the concentration trend. Based on the wireless results in Figure 28 and Figure 30, the NH_3 -MIP-PANI paper sensor seemed to be more sensitive at concentrations lower than 10 ppm, but the sensor would quickly reach saturation according to the calibration curves. The linear range could be improved to adapt the larger applicable detection range for practical use. More detailed studies on the characteristic regions are desired as well.

As mentioned above, the S_{11} represents the reduced reflection coefficient. Based on the principle, a positive value of ΔS_{11} means that the reduced reflection coefficient of the sample has its absolute value smaller than which of the blank (an antenna without PANI deposition). Note

that S_{11} is always negative unless there is no return loss of the signals. That is to say, the antenna of the blank absorbed more power than the sample did, or the antenna of the sample reflected more power to the antenna reader. This explanation is based on the principled definition of S-parameters. As stated in Equation 4, the S_{11} can be calculated by using the complex impedance of the antenna tag and the antenna reader. When the NH_3 -MIP-PANI electrode absorbed NH_3 gas, the doping level of PANI changed to the state which is more favorable to the undoped form of emeraldine base as shown in Figure 18, causing the increase in the impedance and the decrease in the S_{11} of the antenna tag. By principle, the doping level decreases as the NH_3 concentration increases; as a result, we can see the larger ΔS_{11} in those peaks of interest we have previously identified.

In future work, the selectivity to NH_3 gas among multiple gases such as nitrogen oxides (NO_x) and hydrogen sulfide (H_2S) as interferences in the test chamber should be investigated to verify the specific recognition provided by the molecularly imprinted structure. Mixed gas samples can be purged into the test chamber for measuring the wireless signal response in the presence of interference gases to simulate the more practical situations of air pollution or a contaminated indoor environment. Furthermore, the potential in multiplexing sensing of multiple gases on a single antenna tag could be evaluated as well. Possible approaches may involve the integration of different types of molecularly imprinted polymer electrodes on a single antenna tag and the analysis of wireless signals from exposure to samples with multiple target gases.

CHAPTER IV

FURTHER APPLICATIONS OF MOLECULARLY IMPRINTED POLYANILINE

Introduction

Virus Detection and Molecular Imprinting

In addition to chemical compounds, biomolecules or even larger microorganisms can be the templates for molecular imprinting. The synthesis protocol for the virus imprinting would be analogous to the molecular imprinting process for small chemicals, in which templates were replaced by virus samples. The virus template was then removed from the polymer matrix after polymerization, leaving cavities for recognizing the specific virus. A schematic diagram of virus-imprinted polymers with cavities for recognizing the H5N1 influenza virus as an example can be found in Figure 32 [26].

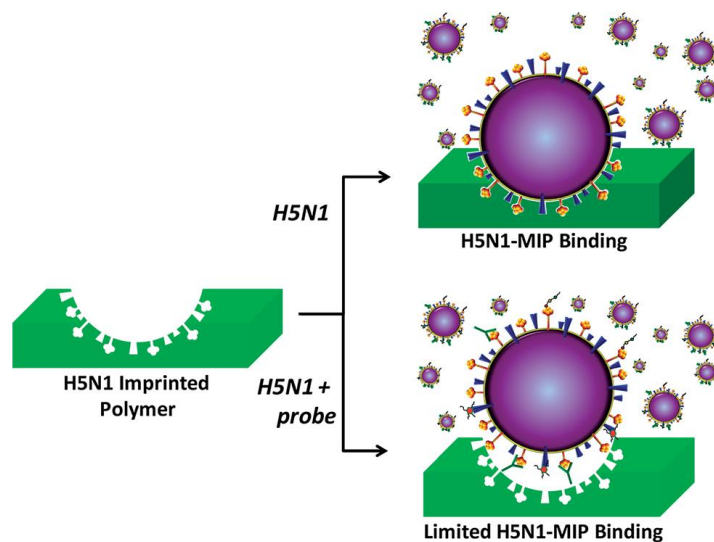


Figure 32 The schematic example of virus-imprinted polymers. As the typical molecular imprinting process, the virus was co-polymerized and removed from the matrix, leaving

cavities for recognizing the H5N1 virus as shown in the scheme. The probe mentioned here in this study was to inhibit the binding with the MIP matrix. Reprinted from [26].

The natural recognition systems like antibodies provide exceptionally sensitive and selective properties; however, they are costly and vulnerable to a harsh environment, and the stability in vitro remains a question that limits the practical application. Therefore, the use of MIPs is to overcome these disadvantages from the intrinsic properties of natural antibodies by the synthetic matrix with a more stable, chemo-resistive, and low-cost surface [32]. A variety type of viruses such as H5N1 influenza [26, 127], human immunodeficiency virus (HIV) [128, 129], poliovirus [129], coronavirus [130, 131], and Zika virus [132] have been molecularly imprinted in various polymer matrices. Moreover, because of the relatively considerable size of viruses compared with small chemical compounds, the theoretical cavities in virus-imprinted polymers may be visualized by surface morphology images of high-resolution field-emission scanning electron microscopy [133] or by atomic force microscopy that produce morphological as well as cross-sectional topology images [134, 135].

As a genus belonging to the family of Retroviridae, lentiviruses, or lentiviral vectors, are a type of RNA viruses containing reverse transcriptase enzyme to deploy the gene of interest to the host cells. The typical example of lentivirus is HIV. Lentiviruses possess the capability of carrying genes up to 8 kb and the genome transducing capacity enables long-term gene expression on the hosts, which is crucial for gene therapies [136, 137]. Some luminescence compounds like green fluorescence proteins can be added to lentiviruses for labeling purposes [138]. As the virus model for molecular imprinting in this study, the green fluorescent protein (GFP)-labeled lentivirus was used as the template.

The MIP-PANI platform developed in the previous chapters had been applied in other analytes like glucose [12, 14], and it is expected to further adapt biomolecules like proteins or viruses. Protein imprinting on PANI using the C-reactive protein is under development by our group, and the results are being wrapped up for forthcoming publications. For the virus detection, we cooperate with Dr. Dung-Fang Lee's group from the University of Texas Health Science Center at Houston, and lentivirus samples were gratefully provided by them. The lentivirus was imprinted in the PANI matrix just as the procedures in the previous chapters of PFC and gas imprinting. While this study of virus imprinting is proceeding at its developmental stage, the results of calibration curves suggest a promising potential in virus sensing application by using virus molecularly imprinted PANI.

Materials and Methods

Materials

The sample vials of GFP-labeled lentivirus were kindly provided by Dr. Dung-Fang Lee's research group from the Department of Integrative Biology and Pharmacology in the University of Texas Health Science Center at Houston. The virus concentration of the vials from a particular batch was estimated to be 2.2×10^5 TU/ml if transducing to cancer cells. The unit of TU/ml represents the number of cells transduced by the virus per ml [139]. The lentivirus was stored at 4°C in a stock solution of Dulbecco's Modified Eagle Medium (DMEM) with 10% of fetal bovine serum (FBS). Phosphate-buffer saline (PBS) for adjusting the virus concentration was diluted from the PBS stock solution (10X concentration) purchased from Sigma-Aldrich (St. Louis, MO, USA).

Synthesis of Lentivirus-Imprinted PANI

The synthesis of lentivirus-imprinted PANI followed the same protocol for PFOA-MIP-PANI and PFOS-MIP-PANI in Chapter II. First, 0.5 ml of the virus stock solution as the template was added to the monomer solution, followed by adding DI water to adjust the total volume to 5 ml. The following steps of addition of the oxidant solution, polymerization, and template removal remained the same. The final virus concentration in the polymer solution was 1.1×10^4 TU/ml. The resulted lentivirus molecularly imprinted PANI (Virus-MIP-PANI) paper strips were air-dried at ambient temperature overnight.

Lentivirus Detection and Resistance Measurement

The fabrication process of the Virus-MIP-PANI paper sensor was the same as the process in Chapter II. For lentivirus detection, virus samples were prepared by diluting the stock solution with PBS. Four different concentrations of 5.5×10^4 TU/ml, 1.1×10^5 TU/ml, 1.65×10^5 TU/ml, and 2.2×10^5 TU/ml were prepared, and PBS served as the control of zero concentration. As previously mentioned, a 30- μ l aliquot of the virus sample was dispensed on the Virus-MIP-PANI electrode, followed by reacting for 30 min. Then, the droplet was removed by a pipette, and the surface was air-dried at ambient temperature. The resistance of the Virus-MIP-PANI electrode was measured in a DC mode of the multimeter after the drying time of 30 min and 24 h. The 30-min is the time required for the remaining liquid on the electrode to be just air-dried without a visible pattern.

Results

Lentivirus Detection

The normalized resistivity ratios of the Virus-MIP-PANI electrodes upon exposure to lentivirus were calculated by Equation 1 as well as Equation 2 and plotted as shown in Figure 33. For the virus-imprinted electrodes, the resistivity ratios after 30 min of drying had a significant difference from the control electrode of NIP-PANI as well as the Virus-MIP-PANI electrode after 24 h of drying. The calibration curve of Virus-MIP-PANI had a transition in its slope at the concentration of 1.1×10^5 TU/ml. The slope increases beyond that concentration, and the data in that region was used to analyze the linear regression line presented in Figure 33. The linear range is from 1.1×10^5 to 2.2×10^5 TU/ml, and the regression equation is $y = 0.000015432x - 0.2667$ with R^2 value of 0.999. Figure 33b shows the enlarged figure of Figure 33a. After 24 h of drying, only the Virus-MIP-PANI electrode exposed to the largest concentration of lentivirus had the statistical difference from the control. The resistivity ratios of the Virus-MIP-PANI electrode also dropped when the drying time was prolonged.

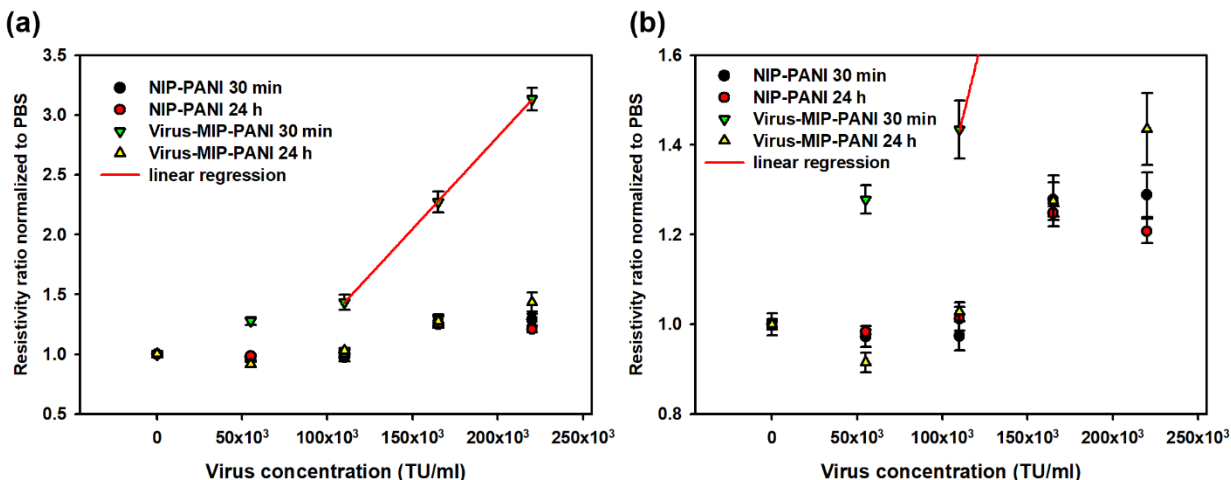


Figure 33 (a) The resistivity ratios and the calibration curves of NIP-PANI and Virus-MIP-PANI electrodes after different time of drying. The red line is the linear regression line calculated from the data between 1.1×10^5 to 2.2×10^5 TU/ml. (b) The enlarged figure focusing on the control groups of NIP-PANI in part a.

Discussion

The virus stock solution was diluted with PBS, while the solvent for the stock solution is DMEM/FBS mixture. The first concern is that whether the DMEM and FBS in the sample solution would affect the signal response or not, especially for the response of Virus-MIP-PANI. Based on Figure 33, since the NIP-PANI did not experience significant responses even for the highest concentration of 2.2×10^5 TU/ml, the responses must be contributed by the virus itself, and the presence of DMEM and FBS in the solution did not significantly affect the signals.

For Virus-MIP-PANI, the decrease in resistivity ratios after 24 h of drying might result from the denatured virus particles on the surface. After the last remaining medium was evaporated, the dried surface was critical for the virus to survive, leading to the denaturation of the virus and the reduced reactivity with Virus-MIP-PANI. In other words, this Virus-MIP-PANI

sensor had the maximum sensitivity after the surface was just air-dried because the viability of the virus particles dropped afterward.

The Virus-MIP-PANI electrode had a larger change in resistivity ratios than the previous studies for PFOA and PFOS. Why the affinity of the virus with PANI is seemingly better is still yet to be determined by more repeating tests and surface characterization to find out the active functional groups. In addition, the strongly acidic environment in the monomer solution remains the typical concern of imprinting biomolecules into the polymer matrix. The viability and functionality of the virus in the monomer solution are also yet to be evaluated to prove the viral compatibility of the synthetic process. Using an analogue or derivative of the target analyte is feasible in molecular imprinting if the target analyte is not applicable in the monomer solution. For example, we used ammonium hydroxide solution and ethanol solvent as the templates for synthesizing the MIP-PANI sensor for gas sensing. Another example that we have cited before is the use of the TNT analogue for fabricating the MIP targeting TNT molecules [17]. Even if the viability of the virus is diminished by the strong acid, the virus could still be imprinted in the PANI matrix so long as the active functional groups or the geometric structure of the virus remain intact. This would need the further characterization of the polymer solution.

The future work includes the use of airborne virus samples for evaluating the practical application of detecting virus concentrations in the air, especially that the detection of airborne viruses has become the most popular topic due to the pandemic of coronavirus disease 2019 (COVID-19). The virus particle concentrations reported in the literature range from 2.9×10^5 to 1.2×10^6 particle/m³ [140]. Theoretically, the particle concentration would be larger than the transduced concentration; however, the different culture media and the unknown correlation factor between the number of virus particles and the transduction units make the direct

comparison very difficult. Other units such as colony-forming unit (CFU)/ml [141] and median tissue culture infectious dose (TCID₅₀)/ml [142] have been reported as well. The use of units should be carefully reviewed before any conclusion can be deployed. In summary, by combining the MIP-PANI and the wireless assay, the device provides the potential for detecting virus aerosols and alerting people if the virus concentration in the residential environment exceeds the infectious threshold.

CHAPTER V

CONCLUSIONS

In this dissertation, we have developed a platform of MIP-PANI paper sensors for detecting different target analytes including PFCs, NH₃ gas, ethanol gas, and lentivirus. Molecular imprinting as a synthetic approach fabricates the polymer matrix with the capability of being imprinted by various types of templates. Artificial antibodies with recognition sites complementary to the target analytes are stable, low-cost, and with good processibility compared with natural antibodies and proteins that are vulnerable to harsh conditions and easy to denature. An overview of the history of molecular imprinting, the principles of synthesis, and the state-of-the-art applications has been elaborated in the introduction part. Then MIP-PANI paper sensors of two types of detection methods of DC resistivity measurement and wireless sensing have been fabricated and investigated in detail.

PFCs are aliphatic acids on which all hydrogen atoms are substituted by fluorine atoms. The series of PFCs are considered carcinogens and water pollutants, and USEPA has released guidelines listing the legal tolerance in drinking water, especially for PFOA and PFOS. The PFC-MIP-PANI paper sensor has been developed with its low-cost compared with conventional assays like LC/MS that are expensive and complex. We synthesized an MIP-PANI electrode on paper in the presence of PFOA or PFOS as the template and integrated it into a flexible electronic paper sensor. The sensor responses based on resistivity ratios were measured and calculated to construct the calibration curves of PFOA and PFOS with the linear ranges from 1 to 200 ppt and with the limits of detection of a ppt level at around 20 ppt or below. By the surface characterization of the MIP-PANI electrode using ATR-FTIR and XPS, the molecular imprinting

process can be visualized on the spectra step-by-step. The detecting mechanism of the transition from emeraldine salts to emeraldine bases associated with the exposure to PFCs was discussed according to the spectroscopy evidence. The investigation on ATR-FTIR and XPS N_{1s} spectra also suggested that the potential binding sites located at quinonoid rings and nitrogen atoms in the PANI matrix. The selectivity tests among the analogous PFCs with shorter alkyl groups or different functional acids showed the good selectivity of the MIP-PANI paper sensor to its designated target molecule of PFOA or PFOS. Comprehensive tests of detecting PFOA or PFOS in their mixture solutions and by using a PFOA/PFOS-hybrid imprinted PANI were performed to evaluate the potential competitive effect as presented in the 3D diagram. In summary, these PFOA-MIP-PANI and PFOS-MIP-PANI paper sensors provide an attractive and alternative way of detecting PFCs in aqueous samples without employing conventional expensive methods.

To expand the potentials of our platform of MIP-PANI, the MIP-PANI paper sensor specially designed for wireless gas sensing was proposed and fabricated. This wireless sensor utilized the RFID communication protocol at a UHF band. In the first place, NH₃-MIP-PANI and EtOH-MIP-PANI paper sensors for gas sensing were evaluated by DC resistance measurement, and the results showed the better performance of MIP-PANI against NIP-PANI for both gases. Although the wireless sensing for ethanol detection was not very promising, three potential characteristic frequencies of around 970 to 980 MHz, 902 to 920 MHz, and around 883 MHz have been identified by the trends in NH₃ concentrations. The calibration curve suggested the possible limit of detection to be 122 ppb. Even though the linear detecting range and the stability of the signal response are yet to be improved, the NH₃-MIP-PANI paper sensor integrated with the antenna tag is still a promising candidate for applications in environmental monitoring or quality control of sealed food packaging. Further studies of using a mixture gas sample of the

target gas and interferences could be performed to prove the selectivity of the gas-imprinted polyaniline sensor. Multiplexing sensing of VOCs on a single device may be possible by redesigning the antenna tag and integrating with multiple types of MIPs.

In addition to detecting aqueous and gaseous chemicals, PANI had been directly imprinted by GFP-lentiviruses and integrated into the Virus-MIP-PANI paper sensor. The DC resistivity ratios after exposure to lentivirus samples increased significantly right after the electrode was just air-dried after 60 min of sample dispensing than the electrode after 24 h of drying, suggesting the denaturation of virus particles on the surface as the sensing element resulted from the lack of culture medium. The resistivity response of the Virus-MIP-PANI electrode was much higher than that of the NIP-PANI control, indicating better detection efficacy. This preliminary study on virus-imprinting further broadens the possible applications of our MIP-PANI platform in biomedical sensing.

Several challenges remain in the MIP-PANI paper sensor. For example, the selectivity among other similar analytes and common interferences coexisting in the real samples needs to be improved and investigated. In conjunction with the selectivity, the sensitivity of the PFC-MIP-PANI paper sensor could be enhanced to identify the types of PFCs at extremely low concentrations. In addition, the synthesis protocol could be further optimized to fabricate the more stable MIP-PANI deposited on a paper substrate which can reduce the cost and provide better sensitivity. The 3D diagrams in this study would need more experiments and data to analyze the thorough competitive effects and distinguish the individual concentration of PFOA or PFOS in the sample solution. For wireless sensing, upgrading with the more powerful VNA as well as reader and optimizing the experimental setup could be helpful to improve the reproducibility of the peak frequencies. The response and recovery time of the gas sensor should

be shortened for practical uses and competing with the commercial gas sensors. Lastly, the potential denaturation of viruses and their viability during the co-polymerization step should be validated by spectroscopy or other biological viability assays to verify the effectiveness of molecular imprinting for microorganisms. Studies based on aerosol-based viral samples could be tested combining with wireless sensing for detecting infectious pathogens in the air. Other applicable investigations include discovering the active functional groups contributing to the interaction between viruses and the polymer matrix.

In conclusion, molecular imprinting technology offers a promising approach to generate synthetic antibodies with the capability of recognizing their designated target. The simple fabrication process, the long-term stability of the sensing element, and the advanced sensitivity of the molecularly imprinted paper-based sensor provide the potential for low-cost sensing and large-scale monitoring of PFCs in wastewater, ammonia gas in the surrounding air, or virus particles in aqueous buffers, addressing related public health and occupational issues, especially for those underserved communities.

REFERENCES

- [1] L. Pauling, "A theory of the structure and process of formation of antibodies," *Journal of the American Chemical Society*, vol. 62, no. 10, pp. 2643-2657, 1940.
- [2] K. Haupt and K. J. C. r. Mosbach, "Molecularly imprinted polymers and their use in biomimetic sensors," vol. 100, no. 7, pp. 2495-2504, 2000.
- [3] G. Anantha-Iyengar *et al.*, "Functionalized conjugated polymers for sensing and molecular imprinting applications," *Progress in Polymer Science*, vol. 88, pp. 1-129, 2019, doi: 10.1016/j.progpolymsci.2018.08.001.
- [4] M. J. Whitcombe, N. Kirsch, and I. A. Nicholls, "Molecular imprinting science and technology: a survey of the literature for the years 2004-2011," *J Mol Recognit*, vol. 27, no. 6, pp. 297-401, Jun 2014, doi: 10.1002/jmr.2347.
- [5] M. J. Whitcombe, M. E. Rodriguez, P. Villar, and E. N. J. J. o. t. A. C. S. Vulfson, "A new method for the introduction of recognition site functionality into polymers prepared by molecular imprinting: synthesis and characterization of polymeric receptors for cholesterol," vol. 117, no. 27, pp. 7105-7111, 1995.
- [6] G. J. A. C. I. E. i. E. Wulff, "Molecular imprinting in cross-linked materials with the aid of molecular templates—a way towards artificial antibodies," vol. 34, no. 17, pp. 1812-1832, 1995.
- [7] J. U. Klein, M. J. Whitcombe, F. Mulholland, and E. N. J. A. C. I. E. Vulfson, "Template-mediated synthesis of a polymeric receptor specific to amino acid sequences," vol. 38, no. 13-14, pp. 2057-2060, 1999.
- [8] Z. Guo *et al.*, "Molecularly Imprinted Polymer/Metal Organic Framework Based Chemical Sensors," *Coatings*, vol. 6, no. 4, 2016, doi: 10.3390/coatings6040042.
- [9] S. Chen, A. Li, L. Zhang, and J. Gong, "Molecularly imprinted ultrathin graphitic carbon nitride nanosheets-Based electrochemiluminescence sensing probe for sensitive detection of perfluorooctanoic acid," *Anal Chim Acta*, vol. 896, pp. 68-77, Oct 8 2015, doi: 10.1016/j.aca.2015.09.022.

- [10] I. Chianella *et al.*, "Direct replacement of antibodies with molecularly imprinted polymer nanoparticles in ELISA--development of a novel assay for vancomycin," *Anal Chem*, vol. 85, no. 17, pp. 8462-8, Sep 3 2013, doi: 10.1021/ac402102j.
- [11] J. Luo, J. Sun, J. Huang, and X. Liu, "Preparation of water-compatible molecular imprinted conductive polyaniline nanoparticles using polymeric micelle as nanoreactor for enhanced paracetamol detection," *Chemical Engineering Journal*, vol. 283, pp. 1118-1126, 2016, doi: 10.1016/j.cej.2015.08.041.
- [12] Z. Chen, C. Wright, O. Dincel, T.-Y. Chi, and J. Kameoka, "A Low-Cost Paper Glucose Sensor with Molecularly Imprinted Polyaniline Electrode," *Sensors*, vol. 20, no. 4, p. 1098, 2020.
- [13] T.-Y. Chi, Z. Chen, and J. Kameoka, "Perfluorooctanesulfonic Acid Detection Using Molecularly Imprinted Polyaniline on a Paper Substrate," *Sensors*, vol. 20, no. 24, p. 7301, 2020.
- [14] Z. Chen, T.-Y. Chi, O. Dincel, L. Tong, and J. Kameoka, "A Low-cost and Enzyme-free Glucose Paper Sensor," in *2020 42nd Annual International Conference of the IEEE Engineering in Medicine & Biology Society (EMBC)*, 2020: IEEE, pp. 4097-4100.
- [15] S. Majumdar, U. Saikia, and D. Mahanta, "Polyaniline-Coated Filter Papers: Cost Effective Hybrid Materials for Adsorption of Dyes," *Journal of Chemical & Engineering Data*, vol. 60, no. 11, pp. 3382-3391, 2015, doi: 10.1021/acs.jced.5b00645.
- [16] J. Luo, J. Huang, Y. Wu, J. Sun, W. Wei, and X. Liu, "Synthesis of hydrophilic and conductive molecularly imprinted polyaniline particles for the sensitive and selective protein detection," *Biosens Bioelectron*, vol. 94, pp. 39-46, Aug 15 2017, doi: 10.1016/j.bios.2017.02.035.
- [17] L. Shi, A. G. Hou, L. Y. Chen, and Z. F. Wang, "Electrochemical sensor prepared from molecularly imprinted polymer for recognition of TNT," *Polymer Composites*, vol. 36, no. 7, pp. 1280-1285, 2015, doi: 10.1002/pc.23032.
- [18] P. Paik, A. Gedanken, and Y. Mastai, "Chiral-mesoporous-polypyrrole nanoparticles: Its chiral recognition abilities and use in enantioselective separation," *Journal of Materials Chemistry*, vol. 20, no. 20, 2010, doi: 10.1039/c000232a.

- [19] T.-C. Tsai, H.-Z. Han, C.-C. Cheng, L.-C. Chen, H.-C. Chang, and J.-J. J. Chen, "Modification of platinum microelectrode with molecularly imprinted over-oxidized polypyrrole for dopamine measurement in rat striatum," *Sensors and Actuators B: Chemical*, vol. 171-172, pp. 93-101, 2012, doi: 10.1016/j.snb.2011.07.052.
- [20] Y. Lattach *et al.*, "Molecularly imprinted surface acoustic wave sensors: The synergy of electrochemical and gravimetric transductions in chemical recognition processes," *Electrochimica Acta*, vol. 73, pp. 36-44, 2012, doi: 10.1016/j.electacta.2011.11.119.
- [21] K.-C. Ho, W.-M. Yeh, T.-S. Tung, and J.-Y. Liao, "Amperometric detection of morphine based on poly(3,4-ethylenedioxythiophene) immobilized molecularly imprinted polymer particles prepared by precipitation polymerization," *Analytica Chimica Acta*, vol. 542, no. 1, pp. 90-96, 2005, doi: 10.1016/j.aca.2005.02.036.
- [22] M. Kempe and K. J. J. o. C. A. Mosbach, "Separation of amino acids, peptides and proteins on molecularly imprinted stationary phases," vol. 691, no. 1-2, pp. 317-323, 1995.
- [23] H. R. Culver, S. D. Steichen, and N. A. Peppas, "A Closer Look at the Impact of Molecular Imprinting on Adsorption Capacity and Selectivity for Protein Templates," *Biomacromolecules*, vol. 17, no. 12, pp. 4045-4053, Dec 12 2016, doi: 10.1021/acs.biomac.6b01482.
- [24] S. Tokonami, E. Shimizu, M. Tamura, and T. Iida, "Mechanism in External Field-mediated Trapping of Bacteria Sensitive to Nanoscale Surface Chemical Structure," *Sci Rep*, vol. 7, no. 1, p. 16651, Nov 30 2017, doi: 10.1038/s41598-017-15086-1.
- [25] B. Yang, H. Gong, C. Chen, X. Chen, and C. Cai, "A virus resonance light scattering sensor based on mussel-inspired molecularly imprinted polymers for high sensitive and high selective detection of Hepatitis A Virus," *Biosens Bioelectron*, vol. 87, pp. 679-685, Jan 15 2017, doi: 10.1016/j.bios.2016.08.087.
- [26] T. Wangchareansak, A. Thitithanyanont, D. Chuakheaw, M. P. Gleeson, P. A. Lieberzeit, and C. Sangma, "A novel approach to identify molecular binding to the influenza virus H5N1: screening using molecularly imprinted polymers (MIPs)," *Med. Chem. Commun.*, vol. 5, no. 5, pp. 617-621, 2014, doi: 10.1039/c3md00272a.

- [27] G. M. Birnbaumer *et al.*, "Detection of viruses with molecularly imprinted polymers integrated on a microfluidic biochip using contact-less dielectric microsensors," *Lab Chip*, vol. 9, no. 24, pp. 3549-56, Dec 21 2009, doi: 10.1039/b914738a.
- [28] S. P. Graham *et al.*, "Evaluation of Molecularly Imprinted Polymers as Synthetic Virus Neutralizing Antibody Mimics," *Front Bioeng Biotechnol*, vol. 7, p. 115, 2019, doi: 10.3389/fbioe.2019.00115.
- [29] F. Cui, Z. Zhou, and H. S. Zhou, "Molecularly Imprinted Polymers and Surface Imprinted Polymers Based Electrochemical Biosensor for Infectious Diseases," *Sensors (Basel)*, vol. 20, no. 4, Feb 13 2020, doi: 10.3390/s20040996.
- [30] S. Ansari and S. Masoum, "Molecularly imprinted polymers for capturing and sensing proteins: Current progress and future implications," *TrAC Trends in Analytical Chemistry*, vol. 114, pp. 29-47, 2019, doi: 10.1016/j.trac.2019.02.008.
- [31] Q. Wang, R. Xue, H. Guo, Y. Wei, and W. Yang, "A facile horseradish peroxidase electrochemical biosensor with surface molecular imprinting based on polyaniline nanotubes," *Journal of Electroanalytical Chemistry*, vol. 817, pp. 184-194, 2018, doi: 10.1016/j.jelechem.2018.04.013.
- [32] M. Gast, H. Sobek, and B. Mizaikoff, "Advances in imprinting strategies for selective virus recognition a review," *TrAC Trends in Analytical Chemistry*, vol. 114, pp. 218-232, 2019, doi: 10.1016/j.trac.2019.03.010.
- [33] L. Luo, J. Yang, K. Liang, C. Chen, X. Chen, and C. Cai, "Fast and sensitive detection of Japanese encephalitis virus based on a magnetic molecular imprinted polymer-resonance light scattering sensor," *Talanta*, vol. 202, pp. 21-26, Sep 1 2019, doi: 10.1016/j.talanta.2019.04.064.
- [34] J. Han *et al.*, "Preliminary investigations into surface molecularly imprinted nanoparticles for *Helicobacter pylori* eradication," *Acta Pharm Sin B*, vol. 5, no. 6, pp. 577-82, Nov 2015, doi: 10.1016/j.apsb.2015.09.003.
- [35] A. B. Lindstrom, M. J. Strynar, and E. L. Libelo, "Polyfluorinated compounds: past, present, and future," *Environ Sci Technol*, vol. 45, no. 19, pp. 7954-61, Oct 1 2011, doi: 10.1021/es2011622.

- [36] C. Xu, H. Chen, and F. Jiang, "Adsorption of perfluorooctane sulfonate (PFOS) and perfluorooctanoate (PFOA) on polyaniline nanotubes," *Colloids and Surfaces A: Physicochemical and Engineering Aspects*, vol. 479, pp. 60-67, 2015, doi: 10.1016/j.colsurfa.2015.03.045.
- [37] Y. Zushi, T. Takeda, and S. Masunaga, "Existence of nonpoint source of perfluorinated compounds and their loads in the Tsurumi River basin, Japan," *Chemosphere*, vol. 71, no. 8, pp. 1566-73, Apr 2008, doi: 10.1016/j.chemosphere.2007.11.055.
- [38] L. B. Biegel, M. E. Hurtt, S. R. Frame, J. C. O'connor, and J. C. J. T. S. Cook, "Mechanisms of extrahepatic tumor induction by peroxisome proliferators in male CD rats," vol. 60, no. 1, pp. 44-55, 2001.
- [39] C. Lau, K. Anitole, C. Hodes, D. Lai, A. Pfahles-Hutchens, and J. J. T. s. Seed, "Perfluoroalkyl acids: a review of monitoring and toxicological findings," vol. 99, no. 2, pp. 366-394, 2007.
- [40] P. Thomford, "104-week dietary chronic toxicity and carcinogenicity study with perfluorooctane sulfonic acid potassium salt (PFOS; T-6295) in rats," *Final Report, 3M T-6295 (Covance Study No. 6329-183, vol. I-IX, 4068 pgs, 3M, St. Paul, MN, 2002.*
- [41] "Technical fact sheet—Perfluorooctane Sulfonate (PFOS) and Perfluorooctanoic Acid (PFOA)," ed. Washington, DC: US Environmental Protection Agency, 2017, pp. 1-8.
- [42] "Regulations, guidance, and advisories for per-and polyfluoroalkyl substances (PFAS)," ed. Washington, DC, USA: Interstate Technology Regulatory Council, 2017.
- [43] Q. Chen, P. Zhu, J. Xiong, L. Gao, and K. Tan, "A sensitive and selective triple-channel optical assay based on red-emissive carbon dots for the determination of PFOS," *Microchemical Journal*, vol. 145, pp. 388-396, 2019, doi: 10.1016/j.microc.2018.11.003.
- [44] Z. Cheng *et al.*, "Highly selective fluorescent visual detection of perfluorooctane sulfonate via blue fluorescent carbon dots and berberine chloride hydrate," *Spectrochim Acta A Mol Biomol Spectrosc*, vol. 207, pp. 262-269, Jan 15 2019, doi: 10.1016/j.saa.2018.09.028.

- [45] C. Fang, X. Zhang, Z. Dong, L. Wang, M. Megharaj, and R. Naidu, "Smartphone app-based/portable sensor for the detection of fluoro-surfactant PFOA," *Chemosphere*, vol. 191, pp. 381-388, Jan 2018, doi: 10.1016/j.chemosphere.2017.10.057.
- [46] P. Wang, G. Sun, L. Ge, S. Ge, J. Yu, and M. Yan, "Photoelectrochemical lab-on-paper device based on molecularly imprinted polymer and porous Au-paper electrode," *Analyst*, vol. 138, no. 17, pp. 4802-11, Sep 7 2013, doi: 10.1039/c3an00694h.
- [47] R. Gerbers, W. Foellscher, H. Chen, C. Anagnostopoulos, and M. Faghri, "A new paper-based platform technology for point-of-care diagnostics," *Lab Chip*, vol. 14, no. 20, pp. 4042-9, Oct 21 2014, doi: 10.1039/c4lc00786g.
- [48] Z. Nie *et al.*, "Electrochemical sensing in paper-based microfluidic devices," *Lab Chip*, vol. 10, no. 4, pp. 477-83, Feb 21 2010, doi: 10.1039/b917150a.
- [49] M. Pozuelo, P. Blondeau, M. Novell, F. J. Andrade, F. Xavier Rius, and J. Riu, "Paper-based chemiresistor for detection of ultralow concentrations of protein," *Biosens Bioelectron*, vol. 49, pp. 462-5, Nov 15 2013, doi: 10.1016/j.bios.2013.06.007.
- [50] M. Santhiago and L. T. Kubota, "A new approach for paper-based analytical devices with electrochemical detection based on graphite pencil electrodes," *Sensors and Actuators B: Chemical*, vol. 177, pp. 224-230, 2013, doi: 10.1016/j.snb.2012.11.002.
- [51] S. Choi, S.-K. Kim, G.-J. Lee, and H.-K. Park, "Paper-based 3D microfluidic device for multiple bioassays," *Sensors and Actuators B: Chemical*, vol. 219, pp. 245-250, 2015, doi: 10.1016/j.snb.2015.05.035.
- [52] Y. Wu, P. Xue, K. M. Hui, and Y. Kang, "A paper-based microfluidic electrochemical immunodevice integrated with amplification-by-polymerization for the ultrasensitive multiplexed detection of cancer biomarkers," *Biosens Bioelectron*, vol. 52, pp. 180-7, Feb 15 2014, doi: 10.1016/j.bios.2013.08.039.
- [53] M. Liu, S. He, W. Fan, Y.-E. Miao, and T. Liu, "Filter paper-derived carbon fiber/polyaniline composite paper for high energy storage applications," *Composites Science and Technology*, vol. 101, pp. 152-158, 2014, doi: 10.1016/j.compscitech.2014.07.008.

- [54] H. Wang, D. Liu, P. Du, and P. Liu, "Flexible and robust amino-functionalized glass fiber filter paper/polyaniline composite films as free-standing tensile-tolerant electrodes for high performance supercapacitors," *Electrochimica Acta*, vol. 228, pp. 371-379, 2017, doi: 10.1016/j.electacta.2017.01.017.
- [55] A. S. Panggabean, H. S. Silaban, S. P. Pasaribu, and Alimuddin, "Method validation of Cd (II) determination in lubrication oil by direct dilution method using atomic absorption spectrophotometer," *Journal of Physics: Conference Series*, vol. 1277, p. 012004, 2019/07 2019, doi: 10.1088/1742-6596/1277/1/012004.
- [56] H. Lee, W. Vogel, and P. P. Chu, "Polyaniline coated active carbon as binary catalysts support for direct methanol fuel cell," *ECS Transactions*, vol. 19, no. 27, p. 127, 2009.
- [57] U. Bogdanovic *et al.*, "Nanomaterial with High Antimicrobial Efficacy-Copper/Polyaniline Nanocomposite," *ACS applied materials & interfaces*, vol. 7, no. 3, pp. 1955-1966, 2015.
- [58] J. Molina, M. Esteves, J. Fernández, J. Bonastre, and F. Cases, "Polyaniline coated conducting fabrics. Chemical and electrochemical characterization," *European Polymer Journal*, vol. 47, no. 10, pp. 2003-2015, 2011.
- [59] X. Gao and J. Chorover, "Adsorption of perfluorooctanoic acid and perfluorooctanesulfonic acid to iron oxide surfaces as studied by flow-through ATR-FTIR spectroscopy," *Environmental Chemistry*, vol. 9, no. 2, pp. 148-157, 2012.
- [60] Q. Liu, A. Huang, N. Wang, G. Zheng, and L. Zhu, "Rapid fluorometric determination of perfluorooctanoic acid by its quenching effect on the fluorescence of quantum dots," *Journal of Luminescence*, vol. 161, pp. 374-381, 2015.
- [61] H. Lin, Y. Wang, J. Niu, Z. Yue, and Q. Huang, "Efficient sorption and removal of perfluoroalkyl acids (PFAAs) from aqueous solution by metal hydroxides generated in situ by electrocoagulation," *Environmental science & technology*, vol. 49, no. 17, pp. 10562-10569, 2015.
- [62] M. Trchová and J. Stejskal, "Polyaniline: The infrared spectroscopy of conducting polymer nanotubes (IUPAC Technical Report)," *Pure and Applied Chemistry*, vol. 83, no. 10, pp. 1803-1817, 2011.

- [63] S. Lal, S. K. Tripathi, N. Sood, and S. Khosla, "Impact of the concentration of multiwall carbon nanotubes on polyaniline," *Journal of Information Display*, vol. 15, no. 3, pp. 111-117, 2014, doi: 10.1080/15980316.2014.916630.
- [64] A. Ramírez-Hernández, C. Aguilar-Flores, and A. Aparicio-Saguilán, "Fingerprint analysis of FTIR spectra of polymers containing vinyl acetate," *Dyna*, vol. 86, no. 209, pp. 198-205, 2019.
- [65] J. Chiguma and W. E. Jones Jr, "Template-Free Synthesis of Aligned Polyaniline Nanorods/Tubes and Copper/Copper Hydroxide Nanowires for Application as Fillers in Polymer Nanocomposites," *Advances in Materials Physics and Chemistry*, vol. 8, no. 01, p. 71, 2018.
- [66] G. Beamson and D. Briggs, "High resolution XPS of organic polymers: the Scienta ESCA300 database," 1992, doi: <https://doi.org/10.1002/adma.19930051035>. Wiley.
- [67] A. V. Naumkin, A. Kraut-Vass, S. W. Gaarenstroom, and C. J. Powell, "NIST X-ray Photoelectron Spectroscopy Database Version 4.1," ed, 2012.
- [68] R. Mason, D. Mingos, G. Rucci, and J. Connor, "Electron emission spectroscopic studies of olefin and other complexes of d 8 and d 10 metal ions," *Journal of the Chemical Society, Dalton Transactions*, no. 16, pp. 1729-1731, 1972.
- [69] C. Worley, M. Vannet, G. Ball, and W. Moddeman, "Surface chemistry of a microcoated energetic material, pentaerythritoltetranitrate (PETN)," *Surface and interface analysis*, vol. 10, no. 6, pp. 273-279, 1987.
- [70] T. Chuang, H. Coufal, and F. Träger, "Infrared laser photoacoustic spectroscopy of adsorbed species," *Journal of Vacuum Science & Technology A: Vacuum, Surfaces, and Films*, vol. 1, no. 2, pp. 1236-1239, 1983.
- [71] B. R. Strohmeier, "Evaluation of polymeric standard reference materials for monitoring the performance of X-ray photoelectron spectrometers," *Applied surface science*, vol. 47, no. 3, pp. 225-234, 1991.
- [72] D. Clark, W. Feast, D. Kilcast, and W. Musgrave, "Applications of ESCA to polymer chemistry. III. Structures and bonding in homopolymers of ethylene and the

- fluoroethylenes and determination of the compositions of fluoro copolymers," *Journal of Polymer Science: Polymer Chemistry Edition*, vol. 11, no. 2, pp. 389-411, 1973.
- [73] P. T. M. Van Attekum, J. Van der Velden, and J. Trooster, "X-ray photoelectron spectroscopy study of gold cluster and gold (I) phosphine compounds," *Inorganic Chemistry*, vol. 19, no. 3, pp. 701-704, 1980.
- [74] E. Kemnitz and K. Niedersen, "Mechanistic aspects of the isomerization reactions of 1, 1, 2, 2-tetrafluoroethane on a CFC-conditioned chromia catalyst," *Journal of fluorine chemistry*, vol. 79, no. 2, pp. 111-119, 1996.
- [75] A. Hess, E. Kemnitz, A. Lippitz, W. Unger, and D. Menz, "ESCA, XRD, and IR characterization of aluminum oxide, hydroxyfluoride, and fluoride surfaces in correlation with their catalytic activity in heterogeneous halogen exchange reactions," *Journal of Catalysis*, vol. 148, no. 1, pp. 270-280, 1994.
- [76] V. Nefedov, Y. V. Salyn, G. Leonhardt, and R. Scheibe, "A comparison of different spectrometers and charge corrections used in X-ray photoelectron spectroscopy," *Journal of Electron Spectroscopy and Related Phenomena*, vol. 10, no. 2, pp. 121-124, 1977.
- [77] D. Briggs, *Handbook of X-Ray and Ultraviolet Photoelectron Spectroscopy*. John Wiley & Sons Canada, Limited, 1977.
- [78] K. Zhang, J. Huang, G. Yu, Q. Zhang, S. Deng, and B. Wang, "Destruction of perfluorooctane sulfonate (PFOS) and perfluorooctanoic acid (PFOA) by ball milling," *Environmental science & technology*, vol. 47, no. 12, pp. 6471-6477, 2013.
- [79] D. Barpaga *et al.*, "Probing the Sorption of Perfluorooctanesulfonate Using Mesoporous Metal–Organic Frameworks from Aqueous Solutions," *Inorganic chemistry*, vol. 58, no. 13, pp. 8339-8346, 2019.
- [80] A. Mohtasebi, T. Chowdhury, L. H. H. Hsu, M. C. Biesinger, and P. Kruse, "Interfacial Charge Transfer between Phenyl-Capped Aniline Tetramer Films and Iron Oxide Surfaces," *The Journal of Physical Chemistry C*, vol. 120, no. 51, pp. 29248-29263, 2016, doi: 10.1021/acs.jpcc.6b09950.

- [81] A. Katrib, B. El-Issa, R. Budeir, and A. Potts, "The He (I) and X-ray photoelectron spectra of some substituted benzalmalonitrile compounds," *Journal of electron spectroscopy and related phenomena*, vol. 49, no. 2, pp. 233-245, 1989.
- [82] J. Peeling, F. E. Hruska, D. M. McKinnon, M. S. Chauhan, and N. S. McIntyre, "ESCA studies of the uracil base. The effect of methylation, thionation, and ionization on charge distribution," *canadian Journal of chemistry*, vol. 56, no. 18, pp. 2405-2411, 1978.
- [83] K. Neoh, E. Kang, and K. Tan, "Structural dependence of polyanilines on reaction medium," *Synthetic metals*, vol. 40, no. 3, pp. 341-354, 1991.
- [84] E. Kang, K. Neoh, T. Tan, S. Khor, and K. Tan, "Structural studies of poly (p-phenyleneamine) and its oxidation," *Macromolecules*, vol. 23, no. 11, pp. 2918-2926, 1990.
- [85] M. Bozack, Y. Zhou, and S. Worley, "Structural modifications in the amino acid lysine induced by soft x-ray irradiation," *The Journal of chemical physics*, vol. 100, no. 11, pp. 8392-8398, 1994.
- [86] M. Devillers, O. Dupuis, A. Janosi, and J.-P. Soumillion, "Coordination compounds as precursors for laser deposition of nickel-based conducting films," *Applied surface science*, vol. 81, no. 1, pp. 83-93, 1994.
- [87] B. Kuswandi, Jayus, A. Restyana, A. Abdullah, L. Y. Heng, and M. Ahmad, "A novel colorimetric food package label for fish spoilage based on polyaniline film," *Food Control*, vol. 25, no. 1, pp. 184-189, 2012, doi: 10.1016/j.foodcont.2011.10.008.
- [88] L. Ding *et al.*, "Morphology-promoted synergistic effects on the sensing properties of polyaniline ultrathin layers on reduced graphene oxide sheets for ammonia and formaldehyde detection," *Journal of Materials Science*, vol. 53, no. 10, pp. 7595-7608, 2018, doi: 10.1007/s10853-018-2109-7.
- [89] S. C. Deogaonkar and N. V. Bhat, "Polymer based fabrics as transducers in ammonia & ethanol gas sensing," *Fibers and Polymers*, vol. 16, no. 8, pp. 1803-1811, 2015, doi: 10.1007/s12221-015-5172-6.
- [90] S. Kladsomboon and T. Kerdcharoen, "A method for the detection of alcohol vapours based on optical sensing of magnesium 5,10,15,20-tetraphenyl porphyrin thin film by an

- optical spectrometer and principal component analysis," *Anal Chim Acta*, vol. 757, pp. 75-82, Dec 13 2012, doi: 10.1016/j.aca.2012.10.054.
- [91] M. Matsuguchi and T. Uno, "Molecular imprinting strategy for solvent molecules and its application for QCM-based VOC vapor sensing," *Sensors and Actuators B: Chemical*, vol. 113, no. 1, pp. 94-99, 2006, doi: 10.1016/j.snb.2005.02.028.
- [92] Y. Zhang, J. Zhang, and Q. Liu, "Gas Sensors Based on Molecular Imprinting Technology," *Sensors (Basel)*, vol. 17, no. 7, Jul 4 2017, doi: 10.3390/s17071567.
- [93] R. A. Potyrailo, H. Ghiradella, A. Vertiatchikh, K. Dovidenko, J. R. Cournoyer, and E. Olson, "Morpho butterfly wing scales demonstrate highly selective vapour response," *Nature Photonics*, vol. 1, no. 2, pp. 123-128, 2007.
- [94] Q. Zhu, Y. M. Zhang, J. Zhang, Z. Q. Zhu, and Q. J. Liu, "A new and high response gas sensor for methanol using molecularly imprinted technique," *Sensors and Actuators B: Chemical*, vol. 207, pp. 398-403, 2015, doi: 10.1016/j.snb.2014.10.027.
- [95] G. K. Mani and J. B. B. Rayappan, "A highly selective room temperature ammonia sensor using spray deposited zinc oxide thin film," *Sensors and Actuators B: Chemical*, vol. 183, pp. 459-466, 2013.
- [96] G. K. Mani and J. B. B. Rayappan, "A highly selective and wide range ammonia sensor—Nanostructured ZnO: Co thin film," *Materials Science and Engineering: B*, vol. 191, pp. 41-50, 2015.
- [97] Z. Han, Y. Xu, H. Wang, H. Tian, B. Qiu, and D. Sun, "Synthesis of ammonia molecularly imprinted adsorbents and ammonia adsorption separation during sludge aerobic composting," *Bioresour Technol*, vol. 300, p. 122670, Mar 2020, doi: 10.1016/j.biortech.2019.122670.
- [98] M. Hussain, K. Kotova, and P. A. Lieberzeit, "Molecularly imprinted polymer nanoparticles for formaldehyde sensing with QCM," *Sensors*, vol. 16, no. 7, p. 1011, 2016.
- [99] Y. Zhang, Q. Liu, J. Zhang, Q. Zhu, and Z. Zhu, "A highly sensitive and selective formaldehyde gas sensor using a molecular imprinting technique based on Ag–LaFeO₃," *J. Mater. Chem. C*, vol. 2, no. 47, pp. 10067-10072, 2014, doi: 10.1039/c4tc01972e.

- [100] T. Alizadeh and L. Hamedsoltani, "Graphene/graphite/molecularly imprinted polymer nanocomposite as the highly selective gas sensor for nitrobenzene vapor recognition," *Journal of Environmental Chemical Engineering*, vol. 2, no. 3, pp. 1514-1526, 2014.
- [101] W. Tan, Q. Yu, X. Ruan, and X. Huang, "Design of SnO₂-based highly sensitive ethanol gas sensor based on quasi molecular-cluster imprinting mechanism," *Sensors and Actuators B: Chemical*, vol. 212, pp. 47-54, 2015.
- [102] P. Kassal, M. D. Steinberg, and I. M. Steinberg, "Wireless chemical sensors and biosensors: A review," *Sensors and Actuators B: Chemical*, vol. 266, pp. 228-245, 2018, doi: 10.1016/j.snb.2018.03.074.
- [103] C. Pannek, K. Schmitt, I. Schumacher, S. Rademacher, and J. Wöllenstein, "E8. 1- Colorimetric gas sensors for RFID-Applications," *Proceedings SENSOR 2015*, pp. 718-722, 2015.
- [104] L. Ruiz-Garcia, L. Lunadei, P. Barreiro, and I. Robla, "A review of wireless sensor technologies and applications in agriculture and food industry: state of the art and current trends," *sensors*, vol. 9, no. 6, pp. 4728-4750, 2009.
- [105] M. Chen, S. Gonzalez, A. Vasilakos, H. Cao, and V. C. Leung, "Body area networks: A survey," *Mobile networks and applications*, vol. 16, no. 2, pp. 171-193, 2011.
- [106] C. Chen, F. Tsow, K. D. Campbell, R. Iglesias, E. Forzani, and N. Tao, "A wireless hybrid chemical sensor for detection of environmental volatile organic compounds," *IEEE sensors journal*, vol. 13, no. 5, pp. 1748-1755, 2013.
- [107] P. Lorwongtragool, E. Sowade, N. Watthanawisuth, R. R. Baumann, and T. Kerdcharoen, "A novel wearable electronic nose for healthcare based on flexible printed chemical sensor array," *Sensors*, vol. 14, no. 10, pp. 19700-19712, 2014.
- [108] P. Kassal *et al.*, "Smart bandage with wireless connectivity for uric acid biosensing as an indicator of wound status," *Electrochemistry Communications*, vol. 56, pp. 6-10, 2015.
- [109] P. Clément *et al.*, "Oxygen plasma treated carbon nanotubes for the wireless monitoring of nitrogen dioxide levels," *Sensors and Actuators B: Chemical*, vol. 208, pp. 444-449, 2015.

- [110] A. Martínez-Olmos, J. Fernández-Salmerón, N. Lopez-Ruiz, A. Rivadeneyra Torres, L. Capitan-Vallvey, and A. Palma, "Screen printed flexible radiofrequency identification tag for oxygen monitoring," *Analytical chemistry*, vol. 85, no. 22, pp. 11098-11105, 2013.
- [111] M. Mortellaro and A. DeHennis, "Performance characterization of an abiotic and fluorescent-based continuous glucose monitoring system in patients with type 1 diabetes," *Biosensors and Bioelectronics*, vol. 61, pp. 227-231, 2014.
- [112] R. Shepherd, S. Beirne, K. T. Lau, B. Corcoran, and D. Diamond, "Monitoring chemical plumes in an environmental sensing chamber with a wireless chemical sensor network," *Sensors and Actuators B: chemical*, vol. 121, no. 1, pp. 142-149, 2007.
- [113] S. G. Kim, J. Jun, J. S. Lee, and J. Jang, "A highly sensitive wireless nitrogen dioxide gas sensor based on an organic conductive nanocomposite paste," *Journal of Materials Chemistry A*, vol. 7, no. 14, pp. 8451-8459, 2019, doi: 10.1039/c9ta00198k.
- [114] R. A. Potyrailo, N. Nagraj, Z. Tang, F. J. Mondello, C. Surman, and W. Morris, "Battery-free radio frequency identification (RFID) sensors for food quality and safety," *J Agric Food Chem*, vol. 60, no. 35, pp. 8535-43, Sep 5 2012, doi: 10.1021/jf302416y.
- [115] G. Iddan, G. Meron, A. Glukhovsky, and P. Swain, "Wireless capsule endoscopy," *Nature*, vol. 405, no. 6785, pp. 417-417, 2000.
- [116] H. Messer, A. Zinevich, and P. Alpert, "Environmental monitoring by wireless communication networks," *Science*, vol. 312, no. 5774, pp. 713-713, 2006.
- [117] R. A. Potyrailo, C. Surman, N. Nagraj, and A. Burns, "Materials and transducers toward selective wireless gas sensing," *Chemical reviews*, vol. 111, no. 11, pp. 7315-7354, 2011.
- [118] Z. Ma *et al.*, "Highly Sensitive, Printable Nanostructured Conductive Polymer Wireless Sensor for Food Spoilage Detection," *Nano Lett*, vol. 18, no. 7, pp. 4570-4575, Jul 11 2018, doi: 10.1021/acs.nanolett.8b01825.
- [119] S. Matindoust, A. Farzi, M. Baghaei Nejad, M. H. Shahrokh Abadi, Z. Zou, and L.-R. Zheng, "Ammonia gas sensor based on flexible polyaniline films for rapid detection of spoilage in protein-rich foods," *Journal of Materials Science: Materials in Electronics*, vol. 28, no. 11, pp. 7760-7768, 2017, doi: 10.1007/s10854-017-6471-z.

- [120] P. J. Pupaikis, *S-parameters for Signal Integrity*. Cambridge University Press, 2020.
- [121] F. Caspers, "RF engineering basic concepts: S-parameters," *arXiv preprint arXiv:1201.2346*, 2012.
- [122] B. I. o. R. Engineers, "The Journal of the British Institution of Radio Engineers," vol. 16, ed. London, UK: British Institution of Radio Engineers., 1956.
- [123] N. Gupta, H. M. Fahad, M. Amani, X. Song, M. Scott, and A. Javey, "Elimination of response to relative humidity changes in chemical-sensitive field-effect transistors," *ACS sensors*, vol. 4, no. 7, pp. 1857-1863, 2019.
- [124] A. S. Alshammari, M. R. Alenezi, K. T. Lai, and S. R. P. Silva, "Inkjet printing of polymer functionalized CNT gas sensor with enhanced sensing properties," *Materials Letters*, vol. 189, pp. 299-302, 2017, doi: 10.1016/j.matlet.2016.11.033.
- [125] J. G. Hester, M. M. Tentzeris, and Y. Fang, "Inkjet-printed, flexible, high performance, carbon nanomaterial based sensors for ammonia and DMMP gas detection," in *2015 European Microwave Conference (EuMC)*, 2015: IEEE, pp. 857-860.
- [126] J. Royo, P. Lambán, and J. Valencia, "Influence of the Position of a UHF-RFID Tag Relative to the Antenna in the Information Reading," *Procedia Engineering*, vol. 63, pp. 151-157, 2013.
- [127] T. Wangchareansak, A. Thitithanyanont, D. Chuakheaw, M. P. Gleeson, P. A. Lieberzeit, and C. Sangma, "Influenza A virus molecularly imprinted polymers and their application in virus sub-type classification," *Journal of Materials Chemistry B*, vol. 1, no. 16, pp. 2190-2197, 2013.
- [128] Y. Ma, X.-L. Shen, Q. Zeng, H.-S. Wang, and L.-S. Wang, "A multi-walled carbon nanotubes based molecularly imprinted polymers electrochemical sensor for the sensitive determination of HIV-p24," *Talanta*, vol. 164, pp. 121-127, 2017.
- [129] B. Babamiri, A. Salimi, and R. Hallaj, "A molecularly imprinted electrochemiluminescence sensor for ultrasensitive HIV-1 gene detection using EuS nanocrystals as luminophore," *Biosensors and Bioelectronics*, vol. 117, pp. 332-339, 2018.

- [130] T. N. Chatterjee and R. Bandyopadhyay, "A molecularly imprinted polymer-based technology for rapid testing of COVID-19," *Transactions of the Indian National Academy of Engineering*, vol. 5, no. 2, pp. 225-228, 2020.
- [131] A. Raziq, A. Kidakova, R. Boroznjak, J. Reut, A. Öpik, and V. Syritski, "Development of a portable MIP-based electrochemical sensor for detection of SARS-CoV-2 antigen," *Biosensors and Bioelectronics*, vol. 178, p. 113029, 2021.
- [132] C. Tancharoen *et al.*, "Electrochemical biosensor based on surface imprinting for zika virus detection in serum," *ACS sensors*, vol. 4, no. 1, pp. 69-75, 2018.
- [133] A. Cumbo, B. Lorber, P. F.-X. Corvini, W. Meier, and P. Shahgaldian, "A synthetic nanomaterial for virus recognition produced by surface imprinting," *Nature communications*, vol. 4, no. 1, pp. 1-7, 2013.
- [134] O. Hayden, P. A. Lieberzeit, D. Blaas, and F. L. Dickert, "Artificial antibodies for bioanalyte detection—Sensing viruses and proteins," *Advanced Functional Materials*, vol. 16, no. 10, pp. 1269-1278, 2006.
- [135] P. A. Lieberzeit, S. Gazda-Miarecka, K. Halikias, C. Schirk, J. Kauling, and F. L. Dickert, "Imprinting as a versatile platform for sensitive materials—nanopatterning of the polymer bulk and surfaces," *Sensors and Actuators B: Chemical*, vol. 111, pp. 259-263, 2005.
- [136] E. Yaniz-Galende and R. Hajjar, "Stem cell and gene therapy for cardiac regeneration," in *Cardiac Regeneration and Repair*: Elsevier, 2014, pp. 347-379.
- [137] R. Bongianino and S. G. Priori, "Gene therapy to treat cardiac arrhythmias," *Nature Reviews Cardiology*, vol. 12, no. 9, p. 531, 2015.
- [138] M. Millington, A. Arndt, M. Boyd, T. Applegate, and S. Shen, "Towards a clinically relevant lentiviral transduction protocol for primary human CD34+ hematopoietic stem/progenitor cells," *PloS one*, vol. 4, no. 7, p. e6461, 2009.
- [139] M. Geraerts, S. Willems, V. Baekelandt, Z. Debyser, and R. Gijssbers, "Comparison of lentiviral vector titration methods," *BMC biotechnology*, vol. 6, no. 1, pp. 1-10, 2006.

- [140] A. J. Prussin, 2nd, E. B. Garcia, and L. C. Marr, "Total Virus and Bacteria Concentrations in Indoor and Outdoor Air," *Environ Sci Technol Lett*, vol. 2, no. 4, pp. 84-88, 2015, doi: 10.1021/acs.estlett.5b00050.
- [141] C. F. Fronczek and J. Y. Yoon, "Biosensors for Monitoring Airborne Pathogens," *J Lab Autom*, vol. 20, no. 4, pp. 390-410, Aug 2015, doi: 10.1177/2211068215580935.
- [142] N. Nikitin, E. Petrova, E. Trifonova, and O. Karpova, "Influenza virus aerosols in the air and their infectiousness," *Advances in virology*, vol. 2014, 2014.

APPENDIX A

THE OPERATING PROCEDURE OF SDR-KITS DG8SAQ VECTOR NETWORK

ANALYZER (VNWA 3)

Operating Procedures:

Software Setting

1. Connect the USB power cable to the VNA and the laptop.
2. Open VNWA software.
3. Select Options – Setup – Rescan the USB Bus – Test the USB Interfaces.

The message “Tests passed without errors” should emerge at the bottom column after the successful connection.

4. Select Audio Settings – Press Auto-setup Audio Devices – Select 48000 Hz – Press OK to setup.
5. If the error regarding microphone settings emerged, select the USB from the Device Manager to change the properties of audio input – Select 48000 Hz.
6. Select Audio Level – Select Reflect Mode by switching the icon at the bottom-left – Connect TX port to RX port with the short coax cable accompanied in the package.
The sinusoidal wave of the Right should disappear, then stop the audio test.
7. The Instrument Setting and Misc. Settings should remain the default settings.

Calibration

1. Set the frequency range from 700 to 1,200 MHz.
2. Select Settings – Sweep – Set 1,000 data points and the scan rate of 100 msec per point.

3. Select Settings – Calibration Kits – Use Arbitrary Model with Amphenol Connex SMA Male Kit.

The reference figures of the calibration standard ports should reveal, and one can check if the picture matches with the calibration standards in hands.

4. Fix the VNA on the table. It should not be moved anymore during the entire experiment after the calibration.

5. Select Measure – Calibrate

Six buttons with red lights will present.

6. Click from the first button of Short to Open, Load, Thru Cal, and Thru Match Cal.

Neglect the option of Crosstalk Cal.

7. Follow the schematic instruction to install the corresponding calibration standard port.

The finished step should reveal as green lights.

8. Save the calibration file for future reference. The calibration should be done before each experiment.

Measurement

1. Select S_{11} mode
2. Make a single sweep and wait for the frequency scan to be completed.
3. Select File – Export Data – Select S2P – dB Phase.
4. Save the result in the destination folder.

Four different experimental settings were tested for validating the calibration and the signal sources: the VNA without any connection, the VNA connected with the antenna reader but no antenna in the test chamber, the antenna without deposition of MIP-PANI, and the antenna with an NH₃-MIP-PANI electrode. Since the calibration procedure is based on the VNA itself without attaching to the antenna reader, the flat maroon line of the VNA-only response in Figure 34 suggests that the calibration step was successful. Attaching the antenna reader generates the S₁₁ response, and the presence of the antenna tag did not affect the profile, indicating that the two separated parts of the antenna need to be electronically connected to work appropriately. The deposition of NH₃-MIP-PANI on the opening space of the antenna resulted in the signal variation in the S₁₁ parameter, indicating that only the presence of NH₃-MIP-PANI contributed to the signal variation. Therefore, the systematic errors from the antenna and the reader themselves can be excluded by subtracting the sample's S₁₁ value to the blank, and the signal variation is merely attributed to the response of NH₃-MIP-PANI upon exposure to the reference air or the target gas.

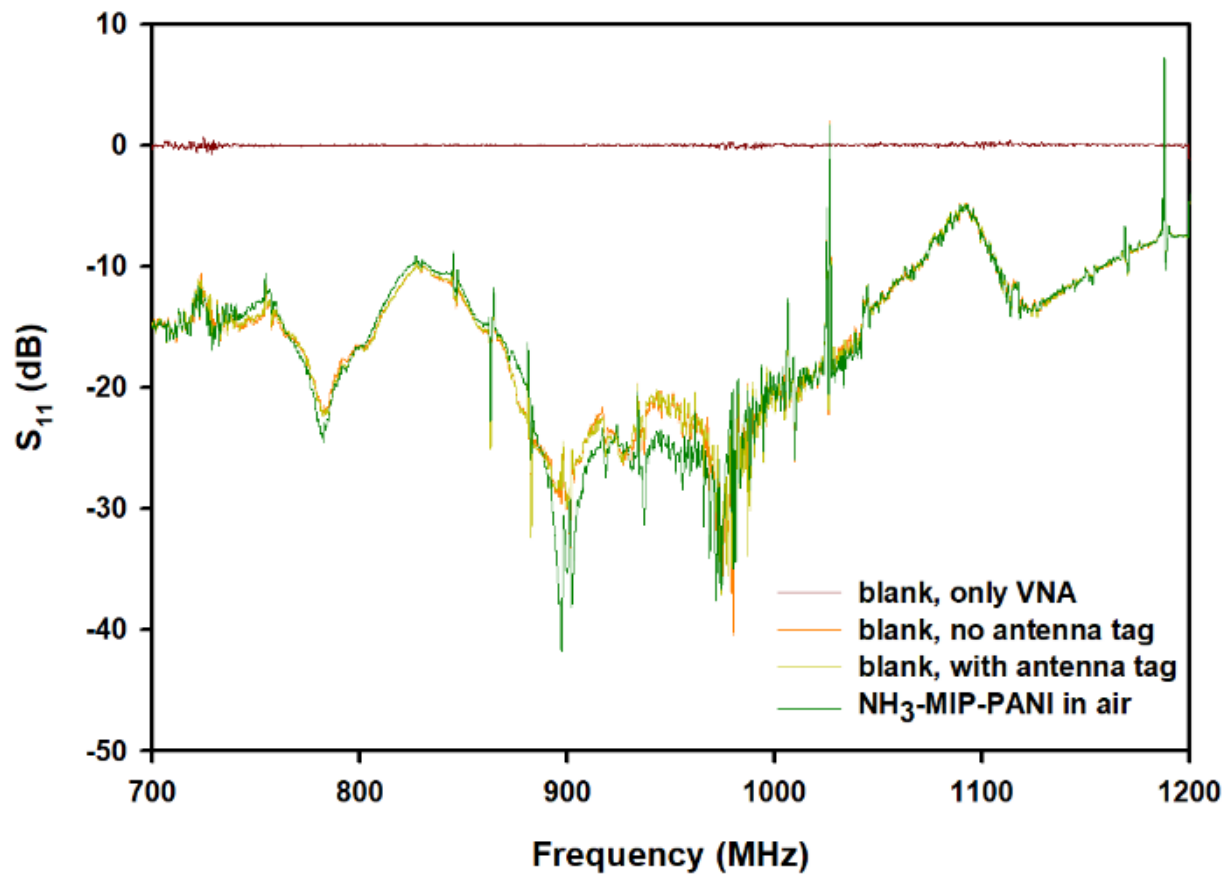


Figure 34 The S_{11} -frequency diagram of signals from four different experimental setups for quality control of the instrumental calibration as well as the signal sources.

APPENDIX B

THE FULL-SPECTRUM DATA OF WIRELESS SENSING

Each sweep generated by the VNA has a frequency range from 700 to 1,200 MHz. The figures with full-spectrum data associated with their corresponding figures in the main context are listed here. The associated figure is mentioned in the following figure captions.

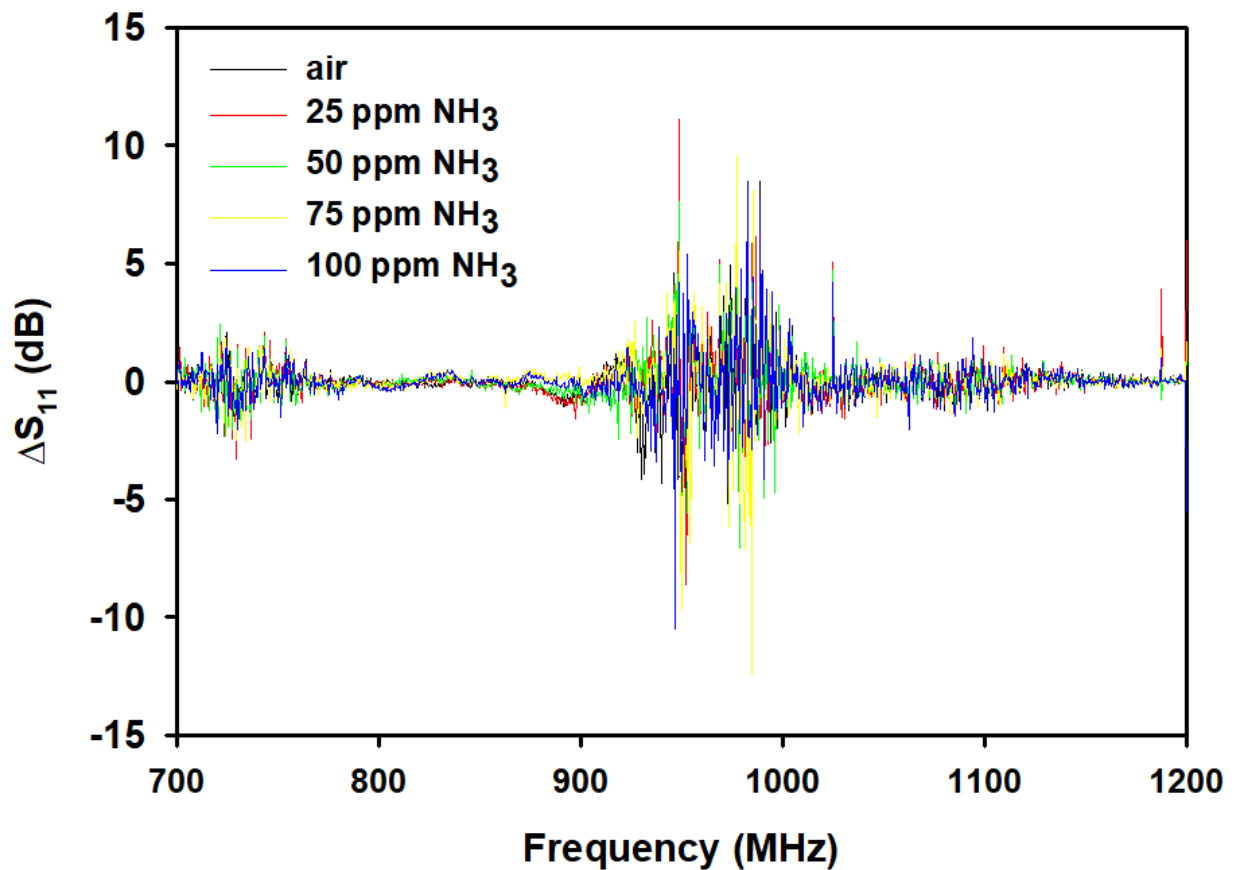


Figure 35 The full-spectrum ΔS_{11} -frequency diagram associated with Figure 26.

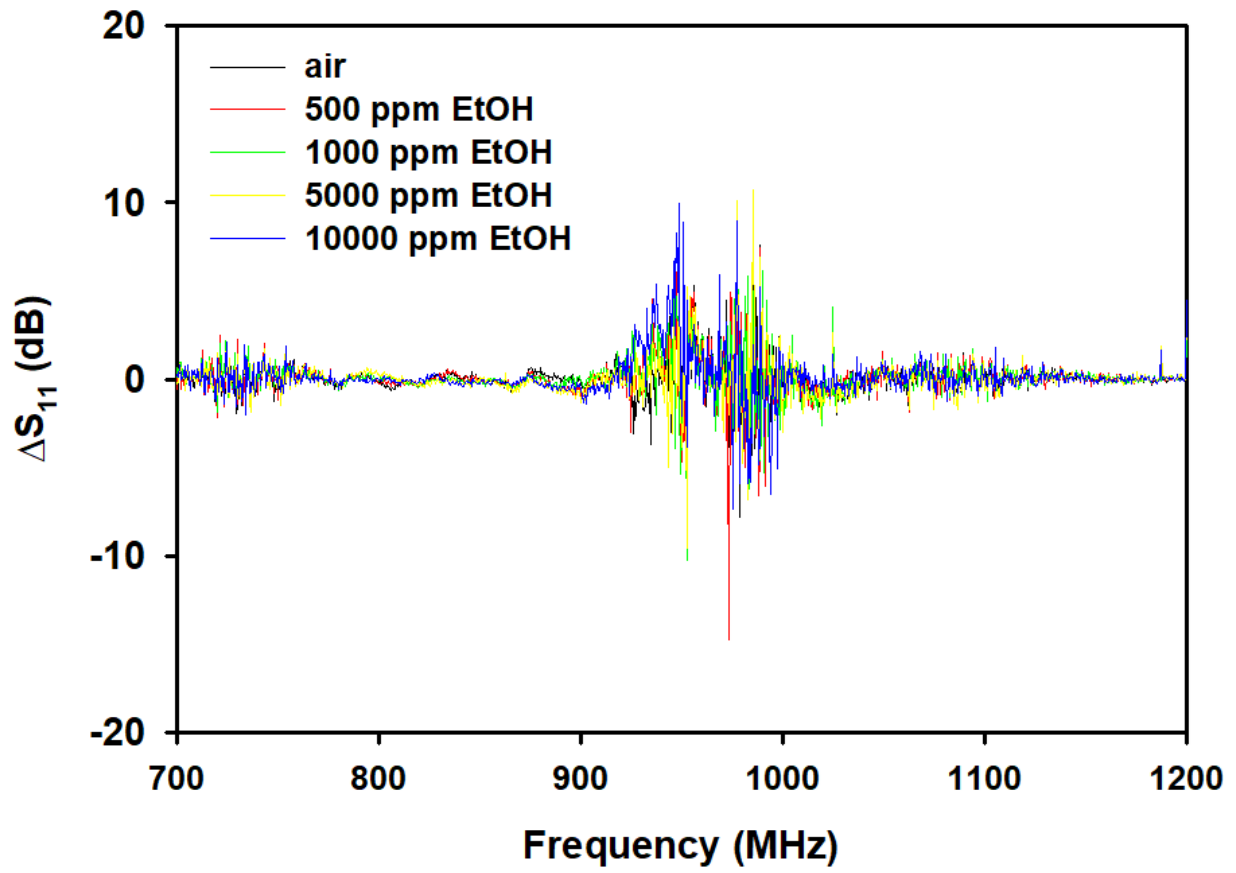


Figure 36 The full-spectrum ΔS_{11} -frequency diagram associated with Figure 27.

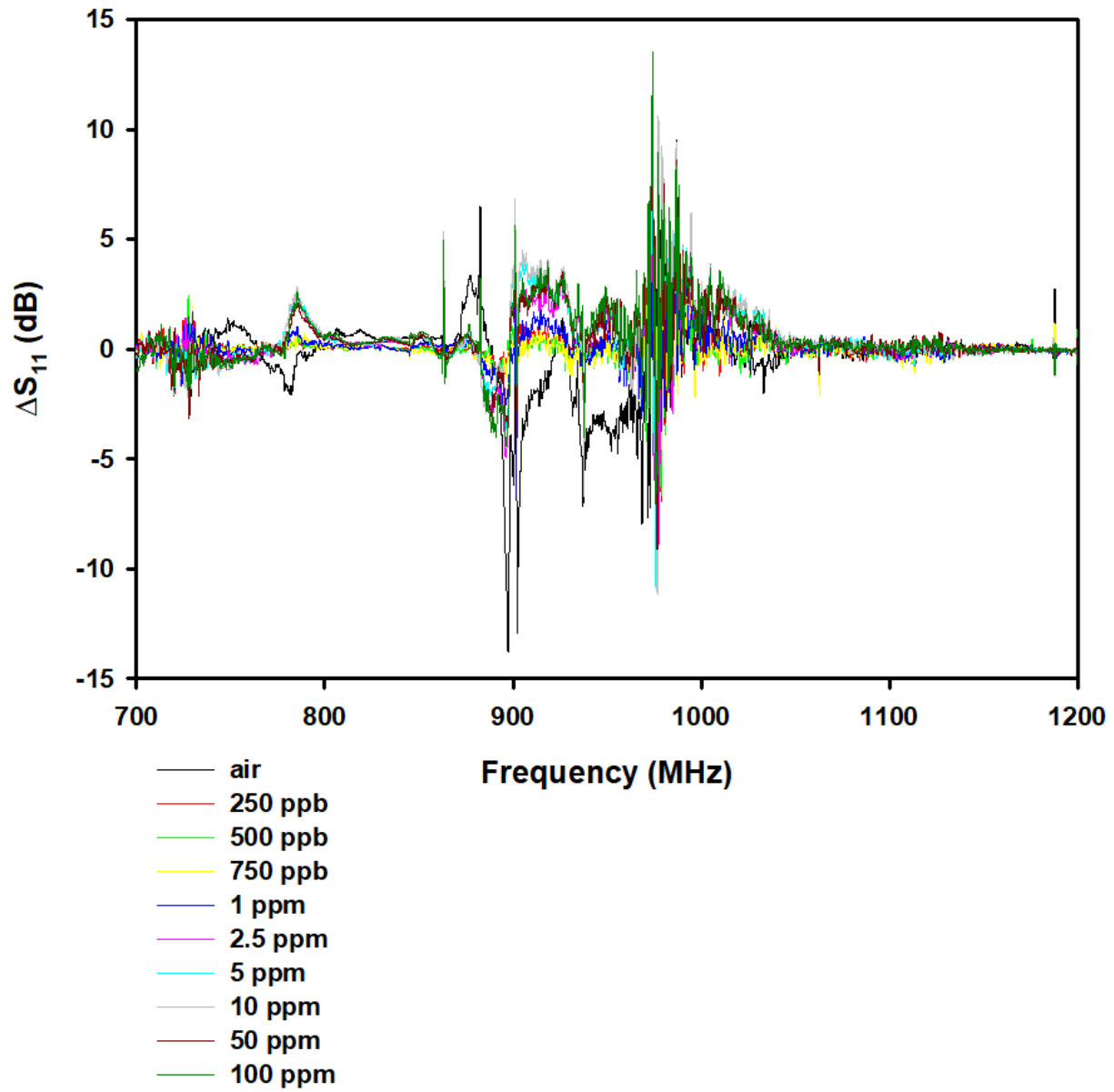


Figure 37 The full-spectrum ΔS_{11} -frequency diagram associated with Figure 28.

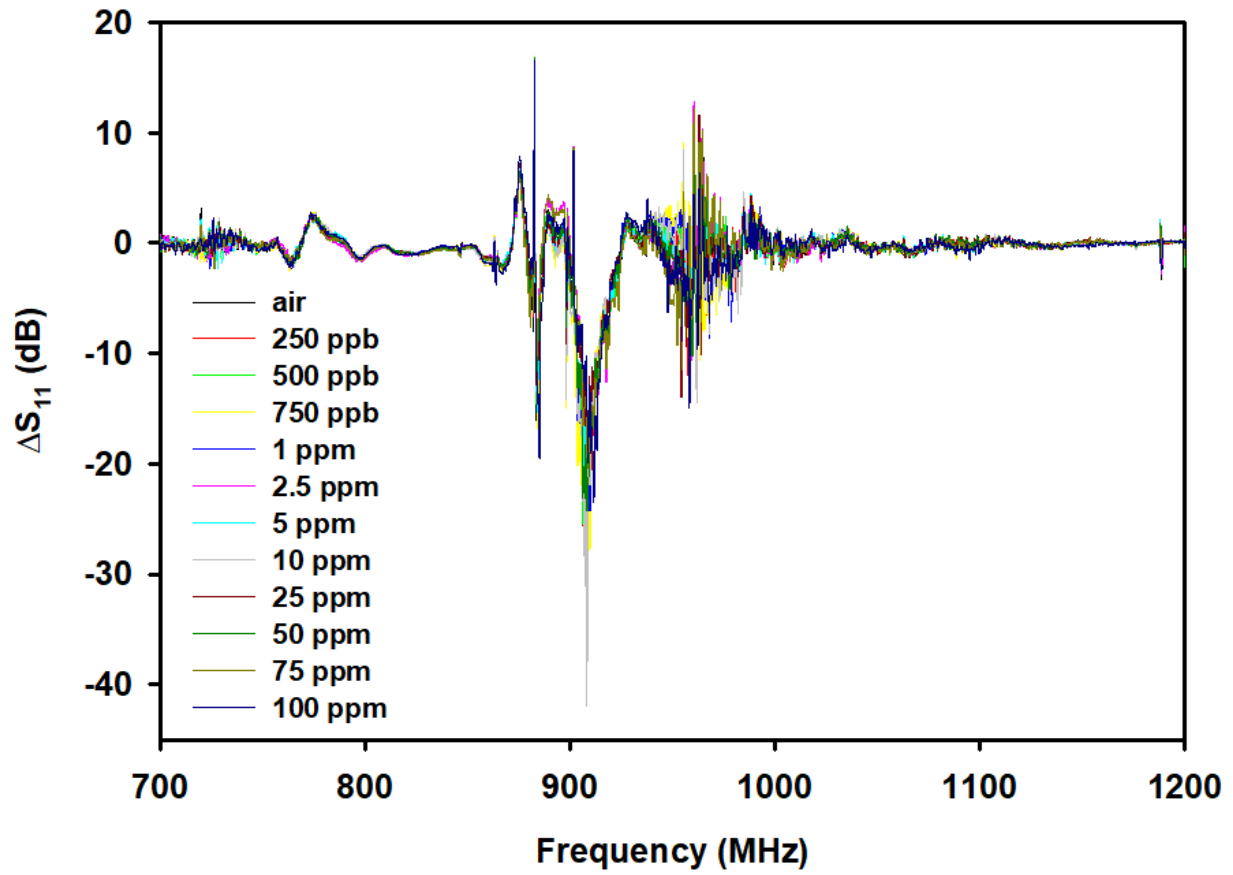


Figure 38 The full-spectrum ΔS_{11} -frequency diagram associated with Figure 30.